The Dissertation Committee for Joshua Kane Davis Certifies that this is the approved version of the following dissertation:

THE BREAKUP OF EAST GONDWANA: insights from plate modeling, basin analysis, and numerical experiments

Committee:

Luc Lavier, Supervisor

Larry Lawver, Co-Supervisor

Ian Dalziel

Sean Gulick

Ian Norton

THE BREAKUP OF EAST GONDWANA: insights from plate modeling, basin analysis, and numerical experiments

by

Joshua Kane Davis, B.S.

Dissertation

Presented to the Faculty of the Graduate School of

The University of Texas at Austin

in Partial Fulfillment

of the Requirements

for the Degree of

Doctor of Philosophy

The University of Texas at Austin

May 2017

Dedication

To Becca, Mom, Dad, and Mandy

Acknowledgements

This work would never have been possible without the support of my family, advisors, friends, and sponsors. My wife, Becca, deserves an enormous amount of credit for this. Despite my weird work schedule, odd stresses, and graduate-student pay grade, Becca has never offered anything by unceasing laughter, encouragement, love, support, and patience. I'm so grateful for her and will definitely 'owe-her' for the rest of our lives. I love you Becca.

My mom, dad, and sister all played a huge role in making me who I am today. Without them, I never would have become interested in geoscience much less considered pursuing PhD research. Thank you for teaching me how to approach the world with drive, curiosity, and creativity. I hope this work makes you proud.

Thank you to my advisors, Larry, Luc, Ian D., Ian N., and Sean. They helped guide all of my half-brained ideas and questions into workable science. They were so patient with me, and never once balked at answering any of my stupid questions. I couldn't think of a better group of researchers to be associated with, and am immensely grateful for all of their contributions to this project.

Thank you to my peers and friends. Especially my former office-mates, Liz and Sebastian. It was never a chore to come into work while you were there. When things got tough, I could always count on you for comradery, jokes, and delirious laughter. They deserve a lot of credit for helping me figure out how to be an adult and graduate student.

THE BREAKUP OF EAST GONDWANA: insights from plate modeling, basin analysis, and numerical experiments

Joshua Kane Davis, PhD

The University of Texas at Austin, 2017

Supervisors: Luc Lavier & Lawrence Lawver

During the Early Cretaceous, East Gondwana began to fragment. Due to temporal proximity to the Cretaceous Normal Superchron and a lack of well resolved seafloor fabric, our understanding of this breakup has historically been limited. A new interpretation of the marine magnetic anomalies preserved within the Somali Basin, provides insight into the motions of the East Gondwana from the Late Jurassic through the Early Mesozoic. When combined and compared with magnetic anomaly interpretations from coeval regional basins, the timing of East Gondwana breakup can be constrained to begin at M15n (135.76 Ma). Within the Enderby Basin, East Antarctica, oceanic and thinned continental crust preserve a record of this rifting. Previous works have suggested that a wide (500 km) domain of thinned continental crust exists between the present-day coastline and a regional, high-amplitude, magnetic anomaly. We offer an alternative interpretation of the Enderby Basin crustal structure, where much of this postulated continental crust is instead thin, proto-ocean crust. This interpretation is based on the lack of isostatically observable crustal thinning throughout the domain, as would be expected for rifted continental blocks. Throughout much of this domain, the crust instead appears to be rugged, thin (<6 km), and of relatively constant thickness, resembling oceanic crust formed at ultraslow/slow ridges. The preferred tectonic interpretation is that, immediately after continental breakup,

magmatic production/emplacement was low and formed this proto-ocean domain. A later reorganization of the magmatic system allowed for normal ocean crust to form and is manifest today as a change in crustal structure and thickness and corresponding magnetic anomaly. Numerical modeling experiments were undertaken to investigate potential influences on melt production during passive continental extension. Factors determined to favor delayed magmatic emplacement include: an initial cool lithosphere geotherm, thin crust, rapid extension rates, low mantle potential temperature, and strong crustal rheology. If magmatic emplacement is sufficiently delayed, these factors may influence formation of a magma-poor margin and/or proto-ocean domain. In the Enderby Basin, Permo-Triassic rifting in the Lambert Graben appears to have previously thinning the continental crust. This pre-breakup thinning may be ultimately responsible for the later formation of the observed proto-ocean domain during East Gondwana breakup.

Table of Contents

List of Tables xi

List of Figures xii

List of Animations xv

Chapter 1: Project Overview 1

Chapter 2: New Somali Basin magnetic anomalies and a plate model for the early Indian Ocean 5

Abstract 5

2.1 Introduction 6

2.2 Gondwana Breakup 7

2.3 East Gondwana Fragmentation 9

2.4 Geophysical Observations & Previous Work 10

2.4.1 The Mozambique Basin and Riiser Larsen Sea 10

2.4.2 The Somali Basin 13

2.4.3 The Western Australian Abyssal Plains 17

2.4.4 The Enderby Basin 19

2.5 Methodology 23

2.5.1 Somali Basin Magnetics 23

2.5.2 Building a Plate Model 27

2.6 Discussion 32

2.7 Conclusions 34

Acknowledgements 35

Chapter 3: The crustal structure of the Enderby Basin 42

Abstract 42

3.1 Introduction 43

3.2 Background 45

3.3 Methods 48

3.3.1 Seismic Data and Seismic Interpretation 48

3.3.2 Synthetic Velocity Model and Time to Depth Conversion 50

3.3.3 Isostatic Moho and Crustal Thickness 54
3.3.4 Regional Basement Interpretations 57
3.3.5 Potential Field Modeling 58
3.4 Results 59
3.4.1 Regional Overview 59
3.4.2 Eastern Domain 60
3.4.3 Central Domain 65
3.4.3.1 Potential causes of crustal variation observed at the EBA75
3.4.4 Western Domain 76
3.5 Conclusions 86

Chapter 4: Influences on the development of volcanic and magma poor morphologies during passive continental rifting 88
Abstract 88
4.1 Introduction 89
4.2 Passive Margin Morphologic Variations 90
4.3 Potential Influencing Factors 92
4.4 Methodology 93
4.4.1 Numerical Model Overview 93
4.4.2 Model Domain 94
4.4.3 Boundary Conditions 96
4.4.4 Initial Thermal Structure 97
4.4.5 Mantle Melting 98
4.4.6 Predicting Margin Morphology 99
4.4.7 Parameter Space & Model Runs 101
4.5 Results 101
4.5.1 Overview 101
4.5.2 Base Model 102
4.5.3 Mantle Potential Temperature 105
4.5.4 Extension Rate 110
4.5.5 Lithosphere Geotherm 116

4.5.6 Crustal Thickness....122
4.5.7 Crustal Rheology....125
4.6. Discussion....128
4.6.1 Overview....128
4.6.2 Significant Influences: Lithosphere Geotherm & Crustal Thickness....130
4.6.3 Important Influences: Extension Rate & Mantle Potential Temperature....132
4.6.4 Likely Influence: Crustal Rheology....133
4.7 Conclusions....134
Appendix....136
References....137

List of Tables

Table 2.1 Somali Basin ship tracks. 22

Table 2.2 Magnetic modeling input parameters. 23

Table 2.3 Plate model total rotation poles 31

Table 4.1 Potential controlling factors and parameter space. 93

Table 4.2 Physical and rheological properties of crust and mantle phases.....95

Table 4.3 Timing and summary of major rifting events in each experiment.....129

List of Figures

Figure 2.1 Indian Ocean study areas. 6
Figure 2.2 Mozambique Basin geophysical data 11
Figure 2.3 Riiser Larsen Sea geophysical data 12
Figure 2.4 Somali Basin seafloor fabric 14
Figure 2.5 West Australia geophysical data 17
Figure 2.6 Enderby Basin geophysical data 20
Figure 2.7 Magnetic profiles & magnetic model 24
Figure 2.8 Somali Basin magnetics and ship track wiggles 26
Figure 2.9 Comparison of Somali Basin flow lines and rotated magnetic anomalies 29
Figure 2.10a Gondwana fit (>182 Ma) 36
Figure 2.10b Mozambique Basin seafloor spreading (M25n—153.71 Ma) 37
Figure 2.10c Somali Basin seafloor spreading (M18r—141.22 Ma) 38
Figure 2.10d East Gondwana breakup begins (M15n — 135.76 Ma) 39
Figure 2.10e West Australia seafloor spreading (M10n — 128.93 Ma) 40
Figure 2.10f Start of the Cretaceous Normal Superchron (120.6 Ma) 41
Figure 3.1 Overview of the Enderby Basin, East Antarctica 44
Figure 3.2 Antarctic Digital Magnetic Anomaly Project compilation 47
Figure 3.3 Free-air satellite gravity data and reflection seismic profiles 49
Figure 3.4 Depth to water bottom 51
Figure 3.5 Depth to top of basement 52
Figure 3.6 Sediment thickness 53
Figure 3.7 Crustal thickness 55

Figure 3.8 Interpreted basement morphology.....56
Figure 3.9 Reflection seismic profile GA229-21.....61
Figure 3.10 Potential field model for GA229-21.....62
Figure 3.11 Reflection seismic profile RAE39-10 63
Figure 3.12 Potential field model for RAE39-10.....64
Figure 3.13 Reflection seismic profile RAE39-03 68
Figure 3.14 Potential field model for RAE39-03.....69
Figure 3.15 Reflection seismic profile GA229-30.....70
Figure 3.16 Potential field model for GA229-30.....71
Figure 3.17 Reflection seismic profile GA228-06.....72
Figure 3.18 Potential field model for GA228-06.....73
Figure 3.19 Sonobuoy velocities with crustal depth.....74
Figure 3.20 Reflection seismic profile GA228-04.....78
Figure 3.21 Potential field model for GA228-04.....79
Figure 3.22 Reflection seismic profile RAE46-07 80
Figure 3.23 Potential field model for RAE46-07.....81
Figure 3.24 Reflection seismic profile GA229-35.....82
Figure 3.25 Potential field model for GA229-35.....83
Figure 3.26 Reflection seismic profile RAE45-04 84
Figure 3.27 Potential field model for RAE45-04.....85
Figure 4.1 Numerical model initial setup. 94
Figure 4.2. Temperature and differential stress profiles 96
Figure 4.3 Base model results.....103
Figure 4.4 Low Tp model results.....107
Figure 4.5 High Tp model results 107

Figure 4.6 Fast model results. 112
Figure 4.7 Slow model results 113
Figure 4.8 Results from Elevated geotherm model 118
Figure 4.9 Results from Depressed geotherm model. 119
Figure 4.10 Results from the Thin crust model 123
Figure 4.11 Results from the Dry Quartz model.....126
Figure 4.12. Modeling results summary 131

List of Animations

Animation 4.1 Base model rifting simulation. 104
Animation 4.2 Low Tp model rifting simulation 108
Animation 4.3 High Tp model rifting simulation 109
Animation 4.4 Fast model rifting simulation 114
Animation 4.4 Slow model rifting simulation 115
Animation 4.6 Elevated geotherm rifting simulation 120
Animation 4.7 Depressed geotherm rifting simulation. 121
Animation 4.8 Thin Crust model rifting simulation 124
Animation 4.9 Dry Quartz rifting simulation 127

Chapter 1: Project Overview

This dissertation focuses on deciphering the breakup of East Gondwana (Australia, East Antarctica, India, Madagascar, Sri Lanka). Understanding this breakup is important for constraining the Mesozoic development of the Indian Ocean, and can provide insights into the processes which act to rift continental lithosphere and form new oceanic crust. While paleontological observations have suggested connections between the now dispersed blocks of East Gondwana for over 125 years (Suess, 1885), the exact manner in which these blocks were dispersed is still a subject of debate. Particularly enigmatic is the fragmentation of East Gondwana into two blocks, consisting of India/Madagascar/Sri Lanka and Australia/East Antarctica. The rifted margins and ocean basins formed from this breakup are preserved in the Enderby Basin, East Antarctica. Two-dimensional thermomechanical experiments can provide insight into the processes which influence continental rifting and can help guide interpretations of Enderby Basin crustal structure and evolution.

In Chapter One, I present a constrained plate models for the formation of the early Indian Ocean. This plate model offers both a constrained age for the breakup of East Gondwana and predictions for extension occurring between India and East Antarctica throughout the breakup. This is accomplished through combination and comparison of the magnetic anomalies and seafloor fabric formed in the Somali Basin and Mozambique Basin. These coeval basins were formed during the separation of East and West Gondwana. A divergence in spreading history preserved in the basins begins at anomaly M15n (135.76 Ma). Reconciling these differences can only be accomplished by fragmenting East Gondwana into two blocks capable of independent motion. Honoring the geophysical

observations from the Somali and Mozambique basins, therefore becomes a constrained prediction for the age and breakup history of East Gondwana, analogous to using two angles of a triangle to determine the third. The plate model produces plausible extension between the blocks of India/Madagascar/Sri Lanka and Australia/East Antarctica, and matches geophysical observations from offshore Western Australia.

In Chapter Two, I present interpretations of the crustal structure of the Enderby Basin, East Antarctica. Previous works have suggests that much of the Enderby Basin consists of thinned continental crust that stretches, up to 500 km from the coastline, to a basin-wide, high-amplitude, magnetic anomaly, the Enderby Basin Anomaly (EBA). In these previous efforts, the EBA is interpreted represent the continent-ocean boundary and demarcate the seaward limit of basement with continental crust seismic velocities. Using public domain, satellite gravity, magnetic anomaly, sonobuoy velocity, and reflection seismic data we have interpreted the basement structure preserved within the Enderby Basin in an effort to better understand the breakup of East Gondwana. The basement of the Enderby Basin is highly varied, with regional domains that demonstrate differences in both crustal thickness and morphology. The most notable difference, between my interpretations and those from previous efforts, concerns the extent of thinned continental crust. Isostatically, the seaward limit of regional crustal thinning is observed to occur up to 275 km inboard of the EBA. The crust within this inboard domain is 4.5-8 km in thickness, with a rugged basement surface. It is difficult to reconcile a wide domain, of this thickness, that fails to demonstrate regional thinning, with a plausible model of continental crust extension. Instead we propose that this inboard domain consists of proto-oceanic crust, with a morphology similar to that observed at slow spreading oceanic crust. Additionally, sonobuoy velocities from this domain do not appear to preclude an oceanic affinity, and may more closely follow velocity-depth trends similar to those observed for oceanic crust.

In Chapter Three, I present results from numerical experiments that investigate the influences on rifted margin morphology formed from passive continental extension. Passive margins demonstrate notable differences in the degree of magmatism accompanying continental breakup. In this regard, passive margins can be classified as either of two end-members: volcanic or magma-poor. In volcanic end-members, magmatic emplacement begins prior to the full thinning of the continental crust, and volcanic intrusion of the continental shelf occurs. While at magma-poor margins, continental breakup precedes magmatic emplacement, and a domain of exhumed lithospheric mantle accommodates extension prior to the onset of seafloor spreading. I conduct numerical experiments to investigate potential influences on the relative timing of magmatic emplacement and continental breakup, and offer constrained estimates for the magnitude of volcanism and the widths of marginal domains. My results suggest that a variety of factors can influence rift-related magmatism, and a spectrum of margin morphologies can be produced. The initial lithosphere geotherm and continental crust, thickness appear to be the most significant influences on margin morphology. Independent variation of either variable can alter the resulting end-member morphology. In aggregate, cool lithosphere geotherms, thin crust, faster extension rates, lower mantle potential temperatures, and strong crustal rheologies tend to favor magma-poor characteristics. In contrast, elevated geotherms, thick crust, slower extension, higher mantle potential temperatures, and weak crustal rheologies are more conducive to formation of volcanic margins.

Integration of these works can help provide insight into the breakup of East Gondwana and the factors which influenced this rifting. Plate modeling results suggest that at the eastern domain of the Enderby Basin underwent extension at more rapid rates (>33 mm/yr.) than the western domain (<15 mm/yr.). Additionally, when placed in an absolute framework, the Kerguelen Hotspot can be located within the eastern domain. Geophysical

observations suggest that, within the Enderby Basin, the eastern domain demonstrates features of a magmatic, volcanic margin, while the central and western domains demonstrates less magmatism, rugged, thin ocean crust, and overall variable morphology. From numerical experiments, I suggest possible controls that might help explain the observed variations. I conclude that the eastern domain was likely influenced by elevated mantle potential temperatures of the Kerguelen hotspot, the central domain by the thin crust of the Lambert Graben, and the western domain by the extents of cratonic lithosphere.

Chapter 2: New Somali Basin magnetic anomalies and a plate model for the early Indian Ocean[1]

ABSTRACT

The oldest portions of the Indian Ocean formed via the breakup of Gondwana and the subsequent fragmentation of East Gondwana. We present a constrained plate model for this early Indian Ocean development for the time period from Gondwana Breakup until the start of the Cretaceous Normal Superchron. The motions of the East Gondwana terranes are determined using new geophysical observations in the Somali Basin and existing geophysical interpretations from other coeval Indian Ocean basins. Within the Somali Basin, satellite gravity data clearly resolve traces of an east–west trending extinct spreading ridge and north–south oriented fracture zones. A compilation of Somali Basin ship track magnetic data allows us to interpret magnetic anomalies M24Bn through M0r about this extinct ridge. Our magnetic interpretations from the Somali Basin are similar in age, spreading rate, and spreading directions to magnetic anomalies interpreted in the neighboring Mozambique Basin and Riiser Larsen Sea. The similarity between the two datasets allows us to match both basin's older magnetic anomaly picks by defining a pole of rotation for a single and cohesive East Gondwana plate.Following magnetic anomaly M15n, we find it is no longer possible to match magnetic picks from both basins and maintain plausible plate motions. To match the post-M15n geophysical data we are forced to model the motions of Madagascar/India and East Antarctica/Australia as independent plates. The requirement to utilize two independent plates after M15n provides strong circumstantial evidence that suggests East Gondwana breakup began around 135 Ma.

[1] Davis, J.K., Lawver, L.A., Norton, I.O., Gahagan, L.M., 2016. New Somali Basin magnetic anomalies and a plate model for the early Indian Ocean. Gondwana Research 34, 16-28. Lawver & Norton assisted in plate modeling. Gahagan assisted in data compilation.

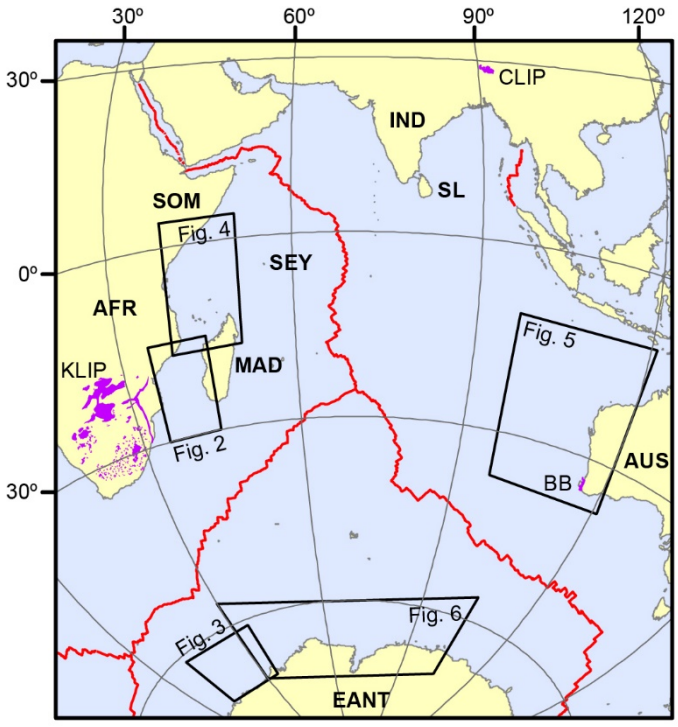

Figure 2.1 Indian Ocean study areas.

Overview of the present-day Indian Ocean and figure locations. Present day oceanic spreading ridges are shown as a solid red line. Subsequent figure locations and study areas are outlined by a solid black line. The extents of relevant volcanic features are shown in purple. BB — Bunbury Basalts; CLIP — Comei Large Igneous Province; KLIP — Karoo Large Igneous Province; AFR—Africa; AUS—Australia; EANT—East Antarctica; IND—India; MAD—Madagascar; SEY—Seychelles; SOM—Somali; SL—Sri Lanka.

2.1 INTRODUCTION

The Indian Ocean is almost entirely bordered by Late Jurassic to Early Cretaceous aged basins (Fig. 2.1; Le Pichon & Heirtzler, 1968; McElhinny, 1970). These oldest vestiges of the Indian Ocean were formed during the breakup of Gondwana and the subsequent fragmentation of East Gondwana (Australia—AUS, East Antarctica—EANT, India—IND, Madagascar—MAD, Seychelles—SEY, and Sri Lanka—SL). Understanding the movement and breakup of East Gondwana allows for a more constrained correlation of Indian Ocean margins and provides valuable insight into the rifting processes that affected

their development. Unfortunately, our knowledge concerning the formation of the Indian Ocean, from Gondwana breakup (182 Ma; Jourdan et al., 2007) to the start of the Cretaceous Normal Superchron (120.6 Ma; Gee & Kent, 2007), is limited by a lack of a plausible and comprehensive plate model. Existing plate models either do not provide constrained rotation parameters or are problematic due to unlikely plate geometries, improbable plate motions, and/or utilization of dubious marine magnetic interpretations. We utilize new magnetic anomaly interpretations in the Somali Basin and leverage existing magnetic anomaly interpretations from the Mozambique Basin and Riiser Larsen Sea (König & Jokat, 2010; Leinweber & Jokat, 2012), to develop a new plate model for the early Indian Ocean. This plate model provides new insights into the breakup of Gondwana, the later fragmentation of East Gondwana, and the development of basin systems offshore the margins of AFR, MAD, EANT, and West AUS.

2.2 GONDWANA BREAKUP

The development of the early Indian Ocean began with the breakup of East and West Gondwana (Le Pichon & Heirtzler, 1968; McElhinny, 1970; Smith & Hallam, 1970; McKenzie & Sclater, 1971). The start of the Gondwana breakup is often correlated with the emplacement of the main phase of the Karoo Large Igneous Province between 184 and 181 Ma (Duncan, 2002; Jourdan et al., 2008). By the Late Jurassic, rifting between East and West Gondwana had developed into seafloor spreading within the Mozambique and Somali Basin systems (Segoufin, 1978; Norton & Sclater, 1979; Segoufin & Patriat, 1980; Rabinowitz et al., 1983). The Mozambique Basin spreading system formed between EANT and AFR, while the Somali Basin system formed concurrently between MAD and AFR. These two spreading systems moved East Gondwana southward relative to present-

day AFR. Oceanic crust from this initial seafloor spreading can be found in the present-day Mozambique Basin (Fig. 2.2), Riiser Larsen Sea (Fig. 2.3), and Somali Basin (Fig. 2.4).

Marine geophysical observations from the Somali Basin, Mozambique Basin, and Riiser Larsen Sea have historically been difficult to integrate within a regional plate model (McKenzie & Sclater, 1971). An ideal plate model for the early development of the two basin systems, would honor the geophysical observations from the three regions, and reflect a cohesive East Gondwana rifting away from West Gondwana (Norton & Sclater, 1979; Segoufin & Patriat, 1980). As such, a single rotation pole for East Gondwana should match magnetic anomalies from the EANT and MAD margins with those on the conjugate AFR margin. Unfortunately, previously interpreted differences between Somali and Mozambique Basin spreading rates and spreading directions have hindered past efforts at building a cohesive East Gondwana plate model (Eagles & König, 2008). In order to overcome these seafloor spreading differences, previous works have suggested two possibilities: either East Gondwana did not separate from West Gondwana as an entirely cohesive unit (Marks & Tikku, 2001) or the geometry of East Gondwana requires significant revision (Eagles & König, 2008). In order to simultaneously satisfy magnetic anomalies and seafloor fabric in the Somali Basin and Mozambique Basin systems, Marks & Tikku (2001) were forced to adopt a plate model where the East Gondwana terranes broke away from West Gondwana as a series of independent microplates. Conversely, Eagles & König (2008) argued for a cohesive East Gondwana that moved as a single unit, but found it necessary to significantly alter the geometry of the East Gondwana terranes in order to match magnetic anomaly interpretations. The East Gondwana geometry proposed in Eagles and König (2008) is unacceptable because it requires an over-tight fit between MAD and EANT. Such a fit leaves no space for Sri Lanka and disrupts apparent pre-

breakup connections between MAD and AFR (see Figure 14 of Eagles & König, 2008). Using recently published magnetic interpretations from the Mozambique Basin and Riiser Larsen Sea (Leinweber & Jokat, 2012) and the most comprehensive magnetic anomaly compilation to date from the Somali Basin, we attempt to address these problems, and to develop a new plate model for the breakup of Gondwana.

2.3 EAST GONDWANA FRAGMENTATION

Following the formation of the Mozambique and Somali Basin systems, East Gondwana began to internally fragment (McElhinny, 1970; McKenzie & Sclater, 1971). This rifting split East Gondwana into two plates, with one plate consisting of IND–MAD–SL–SEY and the other EANT–AUS (Markl, 1974; Sclater & Fisher, 1974). During this separation, IND and its now subducted northern extent, here referred to as "Greater India," rifted away from EANT and western AUS respectively. Oceanic crust from this breakup is found offshore the present-day margins of western AUS in the Cuvier, Gascoyne, and Perth Abyssal Plains (Fig. 2.5) and offshore EANT in the Enderby Basin (Fig. 2.6). Observations from these basins suggest that a ridge jump occurred shortly after M0r (<120.6 Ma; Powell et al., 1988; Borissova et al., 2003; Gaina et al., 2003; Gibbons et al., 2012; Williams et al., 2013). This hypothesized ridge jump is discussed in further detail below, but would imply that the margin of East IND is devoid of significant amounts of oceanic crust formed during East Gondwana fragmentation.

The timing of East Gondwana breakup has historically been based on circumstantial, rather than direct evidence. Although the age of seafloor spreading between Greater India and wAUS is well constrained (Larson et al., 1979; Gibbons et al., 2012; Williams et al., 2013), the assumption that the entirety of Greater India was rigidly attached

to cratonic IND during this separation remains speculative (Lawver et al., 1998). The emplacement of both the Comei Large Igneous Province at 132 Ma (Zhu et al., 2009) and the first phase of the Bunbury Basalts at 132– 130 Ma (Frey et al., 1996; Coffin et al., 2002) provides additional, though indirect, evidence as to the possible start of East Gondwana fragmentation. Recent efforts to improve constraints on the age of East Gondwana breakup rely on interpretations of M-Series magnetic anomalies offshore EANT (Gaina et al., 2003; Gaina et al., 2007; Gibbons et al., 2013). However, Golynsky et al. (2013) concluded that these interpreted M-Series magnetic anomalies are likely incorrect as they are unsupported by the more comprehensive marine magnetic anomaly compilation of the Antarctic Digital Magnetic Anomaly Project. Additionally, improbable two-way plate motion (~500 km left-lateral followed by ~500 km right lateral; Gaina et al., 2007) between IND and MAD, or plate geometries that misfit MAD–IND piercing points (Ishwar-Kumar et al., 2013; Tucker et al., 2014) in combination with more minor two-way plate motion (Gibbons et al., 2013). Our work seeks to develop a more plausible plate model for East Gondwana fragmentation, offer additional constraints on the age of initial rifting, and aid future efforts interpreting airborne-magnetic data from the Princess Elizabeth Trough (Fig. 2.6; Gohl et al., 2007).

2.4 Geophysical Observations & Previous Work

2.4.1 The Mozambique Basin and Riiser Larsen Sea

During Late Jurassic time, rifting between East and West Gondwana transitioned into the Mozambique Basin and Somali Basin seafloor spreading systems (Le Pichon & Heirtzler, 1968; Smith & Hallam, 1970; Norton & Sclater, 1979; Veevers, 2012). Oceanic crust offshore AFR in the Mozambique Basin and offshore EANT in the Riiser Larsen Sea formed during this early phase of seafloor spreading in the Mozambique Basin

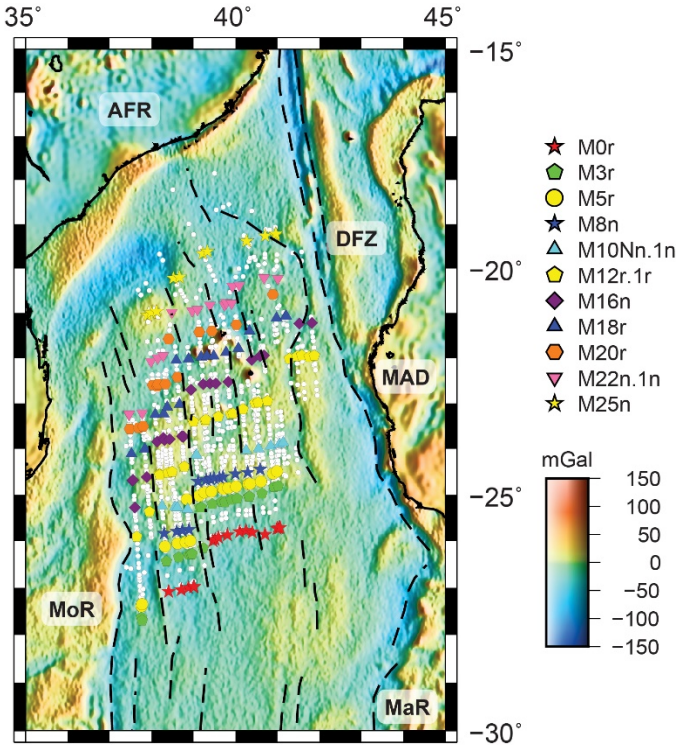

Figure 2.2 Mozambique Basin geophysical data

The Mozambique Basin is bounded by Africa (AFR) to the north, the Mozambique Ridge (MoR) to the west, and to the east by the Davie Fracture Zone (DFZ), Madagascar (MAD), and the Madagascar Ridge (MaR). The basin continues to the south into present day seafloor spreading along the Southwest Indian Ridge, allowing for clear identification of the Cretaceous Normal Superchron and anomaly M0r. Select magnetic picks from Leinweber & Jokat (2012) are plotted as colored symbols and can be identified using the legend on the right. For visual simplicity, the majority of the magnetic picks are plotted as smaller white circles. This dataset of magnetic identifications can be downloaded from the supplementary data provided in this paper. Overlain on the free-air-gravity of Sandwell et al. (2014) are our interpretations of possible fracture zones (dashed black lines).

system. Spreading between AFR and EANT has continued from this inception, and persists today as the slowly spreading Southwest Indian Ridge. This continuity allows for well constrained magnetic and seafloor fabric interpretations. Using satellite gravity data (Sandwell et al., 2014), fracture zones can be traced from a sharp bend near the Southwest Indian Ridge into areas near the margins of the Mozambique Basin and Riiser Larsen Sea. Recent marine magnetic studies have been able to confidently identify the Cretaceous Normal Superchron, magnetic anomaly M0r (120.6 Ma), and the older M-Series magnetic

anomalies offshore both margins (Fig. 2.2 and 2.3; König & Jokat, 2010; Leinweber & Jokat, 2012).

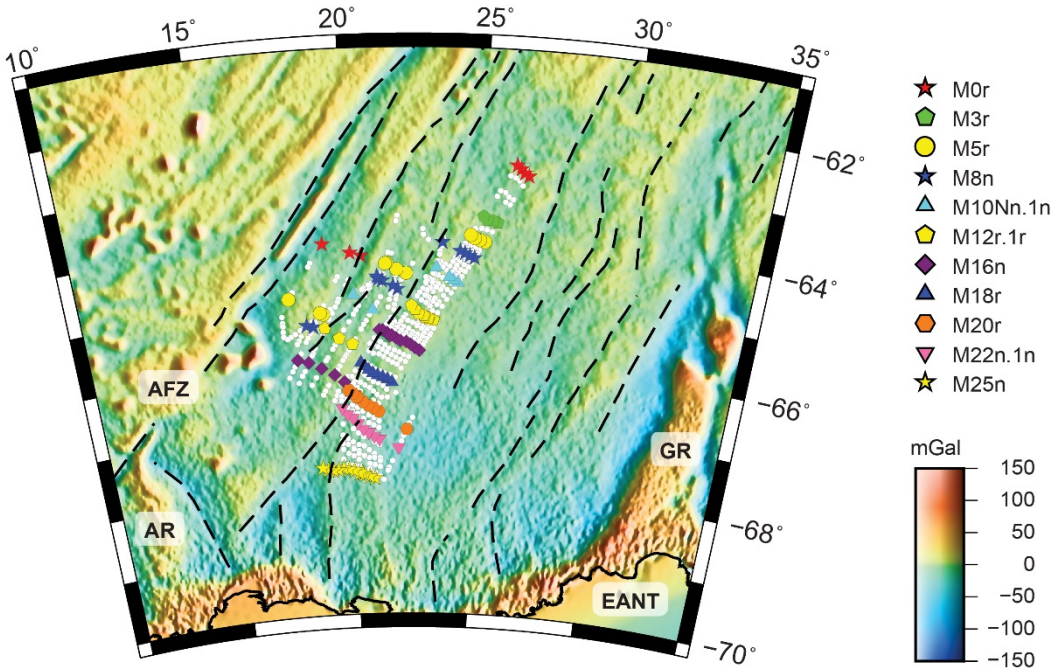

Figure 2.3 Riiser Larsen Sea geophysical data

The Riiser Larsen Sea is bounded by the Astrid Ridge (AR) and Astrid Fracture Zone (AFZ) to the west, East Antarctica (EANT) to the south, and Gunnerus Ridge (GR) to the east. Similar to the Mozambique Basin, the Riiser Larsen Sea continues into present day seafloor spreading along the Southwest Indian Ridge. Select magnetic picks from Leinweber & Jokat (2012) are plotted as colored symbols and can be identified using the legend on the right. For visual simplicity, the majority of the magnetic picks are plotted as smaller white circles. This dataset of magnetic identifications can be downloaded from the supplementary data provided in this paper. Overlain on the free-air gravity of Sandwell et al. (2014) are our interpretations of possible fracture zones (dashed black lines).

Utilizing the most recent versions of satellite gravity data (free air gravity and vertical gravity gradient; Sandwell et al., 2014), we have identified relevant fracture zone traces and seafloor fabric within the Mozambique Basin and Riiser Larsen Sea (dashed black lines; Figs. 2.2 and 2.3). These lineaments help to pair conjugate magnetic anomalies and resolve the paleo-seafloor spreading direction within the Mozambique Basin system. Our interpretations of the seafloor fabric, including all fracture zones and an extinct

spreading ridge, are available for download as .kmz files online in the supplementary data for this paper. For this work, we prefer the recent, high-quality magnetic interpretations from Leinweber & Jokat (2012). Their work used densely spaced aeromagnetic and ship track magnetic measurements to build on the work of König & Jokat (2010), and made over 1300 individual magnetic anomaly picks. Identifications were made in the middle of the magnetic chron and range in age from M0r (120.8 Ma) to M25n (153.71 Ma) in both basins (magnetic picks; Figs. 2.2 and 2.3). Leinweber & Jokat (2012) make a limited number of anomaly identifications older than M25n (153.71 Ma) within the Mozambique Basin, however we treat these older identifications as tentative as they do not have conjugate members in the Riiser Larsen Sea and are part of the more poorly constrained older M-Series anomalies (Cande et al., 1978; Tominaga et al., 2015). Given the detailed fracture zone and magnetic anomaly data, the Mozambique Basin system is the best understood of all the early Indian Ocean basins. As such, the motion of EANT relative to AFR can be resolved and provides a crucial foundation for deciphering the early tectonics and movement of East Gondwana with respect to West Gondwana.

2.4.2 The Somali Basin

The Somali Basin (Fig. 2.4) formed concurrent with the Mozambique Basin system during the breakup of East and West Gondwana (Le Pichon & Heirtzler, 1968; Smith & Hallam, 1970; Heirtzler & Burroughs, 1971). Historically, poorly resolved seafloor fabric and an apparent paucity of magnetic anomaly data have hindered our understanding of basin evolution. Four previous Somali Basin geophysical studies have proposed a variety of potential extinct spreading ridges and a range of possible magnetic anomaly interpretations. Segoufin & Patriat (1980) utilized 3 North–South ship tracks to identify

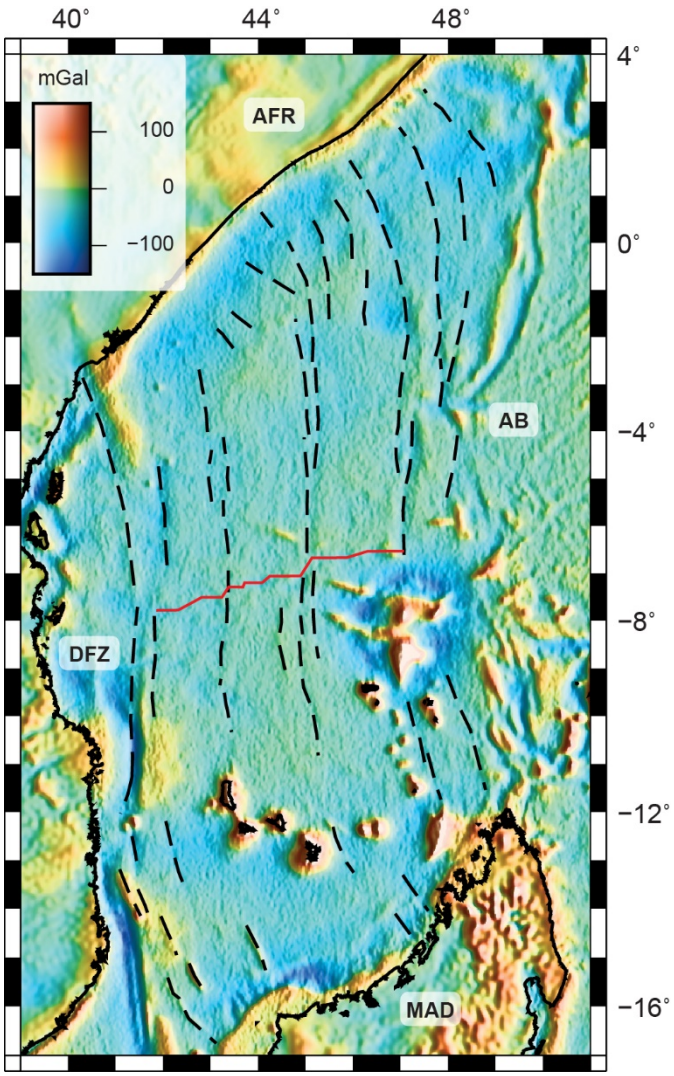

Figure 2.4 Somali Basin seafloor fabric

The Somali Basin is bounded by Africa (AFR), the Davie Fracture Zone (DFZ), Madagascar (MAD), and the Amirante Basin (AB). Recent free air gravity data from Sandwell et al. (2014) help to reveal an extinct spreading ridge in the middle of the basin (solid red line), and evidence of past paleospreading direction within the seafloor fabric (black dashed line).

anomalies M21n (145.52 Ma) to M0r (120.6 Ma) about an extinct ridge at approximately 7°S. They compared their magnetic interpretations with previous magnetic interpretations made in the Mozambique Basin (Segoufin, 1978) and concluded MAD & EANT separated from AFR as a cohesive unit. Segoufin & Patriat (1980) provide rotation poles for EANT–

AFR and MAD–AFR that suggest the plates of East Gondwana remained cohesive through at least anomaly M2n (123.55 Ma). Rabinowitz et al. (1983), overturned many of the interpretations of Segoufin & Patriat (1980) through the analysis of 1 existing ship track and 5 new ship tracks collected between 1980 and 1981. Using this new data, Rabinowitz et al. (1983) identified the young end of anomalies M25n (153.43 Ma) through M9n (128.34 Ma) about an extinct ridge ranging from 5°S to 10°S. Using the same dataset as Rabinowitz et al. (1983); Cochran (1988) proposed an alternative ridge geometry and magnetic interpretation. He interpreted anomalies M22n (147.18Ma) through M0r (120.6 Ma) about an extinct ridge running from 4°S to 7°S. Lastly, Eagles & König (2008) leveraged magnetic interpretations from the Mozambique Basin, and the same ship tracks from Rabinowitz et al. (1983) to interpret anomalies M25n (153.43Ma) to M10n (128.93 Ma) about an extinct ridge from 5°S to 10°S.

The dominance of the horizontal magnetic field component at low latitudes, in conjunction with seafloor spreading oriented North– South, creates a remnant magnetic anomaly profile across the Somali Basin that is anti-symmetric about the spreading axis. In an antisymmetric profile, magnetic anomalies from one side of the spreading ridge correlate with their horizontal mirror on the conjugate side of the ridge. In the Somali Basin, the young ends of normally magnetized ocean crust generate magnetic anomaly peaks on the south side of the ridge and magnetic anomaly troughs on the conjugate north side. Conversely, the young ends of reversed magnetized crust produce magnetic anomaly troughs on the south side of the ridge and magnetic anomaly peaks on the north side. This anti-symmetric relationship can be seen in our synthetic magnetic anomaly profile shown in Fig. 2.7, as well as in the models of Segoufin & Patriat (1980) and Cochran (1988). Based on the anti-symmetric nature of the Somali Basin, we suggest that the magnetic interpretations made by Rabinowitz et al. (1983) and Eagles & König (2008) are erroneous.

Rabinowitz et al. (1983) used appropriate input parameters to generate an anti-symmetric synthetic profile for their spreading model. However, the authors incorrectly identified the magnetic isochrons in their synthetic profile as though they were symmetric across the ridge. This misidentification carried into Rabinowitz et al. (1983)'s interpretation of the observed magnetic anomalies, thus leading to an erroneous interpretation of the data. Eagles & König (2008) incorrectly generated a symmetric synthetic model to represent a remnant magnetic profile across the Somali Basin. Eagles & König (2008) then erroneously interpreted magnetic isochrons in the observed magnetic anomalies utilizing their incorrect symmetric synthetic profile.

By utilizing recent satellite derived gravity data (free air gravity and vertical gravity gradient; Sandwell et al., 2014) to resolve an extinct spreading ridge within the basin (solid red Line, Fig. 2.4), an improvement can be made on previous efforts. The extinct ridge trends East to West across the basin, between 6°S and 8°S. Our interpreted extinct spreading ridge is similar in geometry and location to the ridges proposed by Segoufin & Patriat (1980) and Cochran (1988). The satellite gravity data also reveals several North–South fracture zone traces that help constrain paleospreading direction with improved accuracy (dashed black lines, Fig. 2.4). In addition to new gravity interpretations, a more comprehensive collection of magnetic data is used in this study. This compilation incorporates all of the previously published ship track magnetic data as well as 2 previously unpublished ship tracks. These ship tracks give unprecedented coverage within the basin and allows for the improved identification of magnetic anomalies.

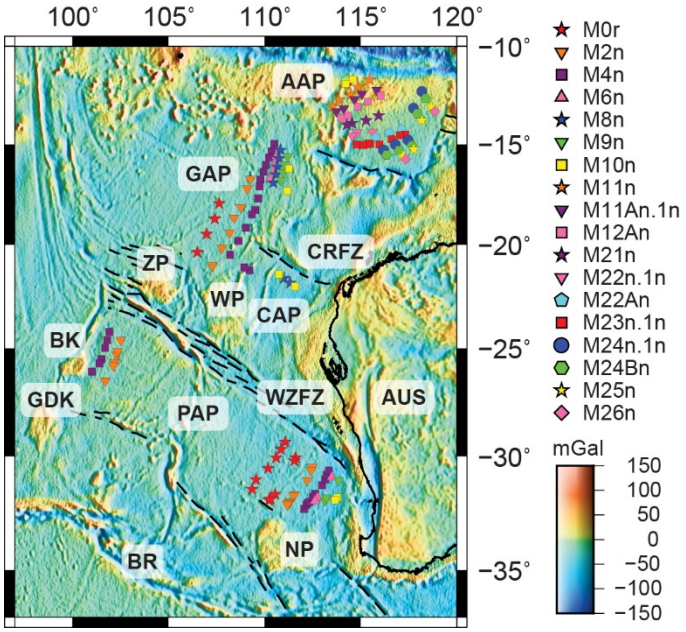

Figure 2.5 West Australia geophysical data

Seafloor formed via the breakup of East Gondwana along the margin ofWest Australia includes the Cuvier Abyssal Plain (CAP), Gascoyne Abyssal Plain (GAP), and Perth Abyssal Plain (PAP). Interpreted fracture zones (dashed black lines) are overlain on the free air gravity of Sandwell et al. (2014). Magnetic interpretations in the Cuvier Abyssal Plain and Gascoyne Abyssal Plain are from Gibbons et al. (2012). In the Perth Abyssal Plain we utilize the magnetic interpretations of Williams et al. (2013). AAP — Argo Abyssal Plain, BK — Batavia Knoll, BR — Broken Ridge, CRFZ — Cape Range Fracture Zone, GDK — Gulden Draak Knoll, NP — Naturaliste Plateau, WP Wallaby Plateau, WZFZ — Wallaby Zenith Fracture Zones, Zenith Plateau — ZP.

2.4.3 The Western Australian Abyssal Plains

During Early Cretaceous time, East Gondwana broke into two plates, one consisted of IND–MAD–SL–SEY, and the other AUS–EANT (Markl, 1974; Sclater & Fisher, 1974). The Cuvier Abyssal Plain, and Gascoyne Abyssal Plain, offshore Western Australia (Fig. 2.5), preserve a record of rifting between Greater India and AUS (Gibbons et al., 2012). Similarly, the Perth Abyssal Plain preserves separation between Greater India and AUS, but depending on the initial plate geometry, may also preserve seafloor formed between cratonic IND and AUS (Williams et al., 2013). It is unknown if Greater India was wholly

and rigidly attached to cratonic IND, therefore these basins provide only indirect evidence regarding East Gondwana fragmentation. However given the quality, these data provide important insights relative to early Indian Ocean tectonics and therefore are incorporated into our regional plate model.

Rifting along the western margin of AUS initiated via the southward propagation of existing spreading centers in the Argo Abyssal Plain (Gibbons et al., 2012). Geophysical interpretations within the Cuvier Abyssal Plain and Gascoyne Abyssal Plain (Gibbons et al., 2012) suggest seafloor spreading within both basins began around M10n (128.93Ma). The distinct Cape Range Fracture Zone, just north of the Cuvier Abyssal Plain, helps constrain a NW/SE seafloor spreading direction relative to present day AUS. Gibbons et al. (2012) suggest that a series of westward ridge jumps after M8n (127.79 Ma) acted to isolate the Wallaby and Zenith Plateaus outboard of the Cuvier Abyssal Plain.

The more southerly Perth Abyssal Plain developed when the southern portion of Greater IND and possibly the northern section of cratonic IND rifted from the wAUS margin. Williams et al. (2013) suggest that this basin preserves a record of cratonic IND rifting from wAUS. Based on our constrained fit of IND and plate motions, it appears plausible that at least some portion of the basin formed via the separation of cratonic IND and wAUS. The Diamantina and Wallaby Zenith Fracture Zones in the Perth Abyssal Plain have orientations similar to that of the Cape Range Fracture Zone and support a NW/SE spreading regime (dashed black lines, Fig. 2.5). Two bathymetric highs, the Batavia Knoll and the Gulden Draak Knoll, border the western side of the Perth Abyssal Plain. Based on dredged samples, these seamounts are thought to be thinned continental crust that separated from Greater India and were isolated on the AUS plate via a spreading ridge jump (Beslier et al., 2004). Using Perth Abyssal Plain magnetic anomaly data, Williams et al. (2013) interpreted magnetic anomalies M10n (128.93 Ma) through M0r (120.6 Ma), as well as

several possible abandoned spreading centers. Williams et al. (2013) contend that consecutive westward ridge jumps occurred shortly after anomaly M0r (120.6 Ma) and again between 101 and 103 MA. The authors postulate that the later ridge jump ended Perth Abyssal Plain seafloor spreading, and attached the Batavia & Gulden Draak Knolls to AUS plate. If cratonic IND did separate from AUS in the Perth Abyssal Plain, then the oldest anomaly (M10n — 128.93 Ma) in the basin provides a constraint on the youngest possible age for East Gondwana fragmentation. Additionally, the younger Perth Abyssal Plain magnetic anomalies (Williams et al., 2013) will be used to verify the plate motions predicted for the plates of MAD/IND and EANT/AUS following the breakup of East Gondwana.

2.4.4 The Enderby Basin

Similar to the wAUS abyssal plains, the Enderby Basin offshore East Antarctica, formed during the fragmentation of East Gondwana (Sclater & Fisher, 1974; Norton & Sclater, 1979; Royer & Coffin, 1988; Veevers, 2012). Seafloor in the Enderby Basin (Fig. 2.6) preserves the record of rifting between IND–SL and EANT. Unfortunately, despite an abundance of marine studies, geophysical observations have not found any definitive indicators of rifting age, spreading rate, or spreading direction. Seafloor fabric in the region is obscured by both thick sedimentary cover and the abundant volcanism of the Kerguelen Plateau. Marine magnetic anomalies are ambiguous and devoid of any clearly identifiable magnetic chrons (Golynsky et al., 2013). Given the paucity of quality data to constrain Enderby Basin rifting, we have leveraged our plate model in conjunction with the limited geophysical observations discussed below, in an effort to aid future works deciphering basin evolution.

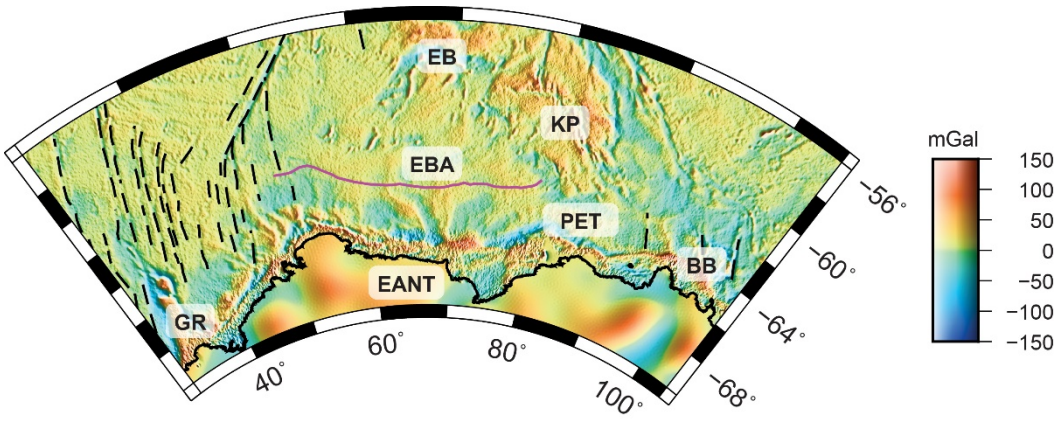

Figure 2.6 Enderby Basin geophysical data

The Enderby Basin is bounded by Gunnerus Ridge (GR), East Antarctica (EANT), and Bruce Bank (BB). Possible fracture zones (black dashed lines) appear sparse along much of the margin, but our best interpretations are plotted over the free-air-gravity of Sandwell et al. (2014). The Enderby Basin Anomaly (EBA; Golynsky et al., 2013) is shown as a solid purple line. This anomaly is thought to represent the inboard limit of true oceanic crust (Stagg et al., 2004). Due to the problematic nature of previous magnetic anomaly interpretations, no published magnetic picks are utilized for the Enderby Basin. Recent helicopter magnetic data have been collected within the Princess Elizabeth Trough (PET; Gohl et al., 2007) and may aid future efforts constraining the breakup of East Gondwana and the formation of the Enderby Basin. EB — Elan Bank, KP — Kerguelen Plateau.

One of the most distinct geophysical features of the Enderby Basin, is a long, linear, large amplitude, positive, magnetic anomaly, approximately 300 km outboard of the margin, known as the Enderby Basin Anomaly (Gaina et al., 2007; Golynsky, 2007; Golynsky et al., 2013). Gravity, magnetic, and seismic data collected and integrated by Stagg et al. (2004) and Leitchenkov et al. (2014) have demonstrated that the Enderby Basin Anomaly is coincident with a step up in basement at the inboard edge of unequivocal oceanic crust. The crustal structure inboard of the Enderby Basin Anomaly is generally considered to be thinned continental crust (Stagg et al., 2004).

Several works have attempted to interpret M-Series magnetic anomalies within the ocean crust outboard of the Enderby Basin Anomaly (Gaina et al., 2003, 2007; Gibbons et al., 2013). Their interpretations appear unsupported by the magnetic dataset compiled by the Antarctic Digital Magnetic Anomaly Project (Golynsky et al., 2013). Additionally,

these M-Series magnetic interpretations appear doubtful when integrated within a regional Indian Ocean plate model. The interpreted anomalies are far enough outboard of the EANT margin that they force either highly improbable 500 km two-way plate motion between IND and MAD (Gaina et al., 2003, 2007), or a more modest two-way plate motion coupled with unlikely original configurations of MAD–IND– EANT (Gibbons et al., 2013).

Aeromagnetic efforts to the west of the Enderby Basin Anomaly near Gunnerus Ridge, were unable to identify any M-Series magnetic anomalies that would help constrain East Gondwana breakup (Jokat et al., 2010). Jokat et al. (2010) contend that the lack of clear anomalies suggest that the western Enderby Basin most likely formed during the Cretaceous Normal Superchron. To the East of the Enderby Basin Anomaly and inboard of Kerguelen Plateau, recent deep seismic studies have identified seismic velocities consistent with ocean crust in Princess Elizabeth Trough (Gohl et al., 2007; Leitchenkov et al., 2014). Helicopter-magnetic data collected within the Princess Elizabeth Trough show clear magnetic lineations (Gohl et al., 2007). These new data will likely provide the best constraints to date on the age of East Gondwana breakup.

Within the Enderby Basin, the Kerguelen Plateau has been the subject of extensive geophysical surveys and multiple Ocean Drilling Program drill sites (ODP Legs 119, 120, 183, & 188). The maximum ages of basalts recovered from these ODP sites provide a minimum age for seafloor at select locations, with the oldest sample dated as 119 Ma from the southern Kerguelen Plateau (Duncan, 2002). Several lines of evidence point towards a possible continental affinity for parts of the Kerguelen Plateau and suggest that a ridge jump may have isolated continental fragments from the IND margin and attached them to the EANT plate (e.g., Frey et al., 2000; Gaina et al., 2003). Basalts drilled on ODP Leg 119, from the southern Kerguelen Plateau have geochemical signatures which suggest a subcontinental lithosphere origin (Alibert, 1991). ODP drilling during Leg 183 on Elan

Bank within the Kerguelen Plateau, recovered a conglomerate unit, with clasts of biotite-garnet gneiss, interbedded between lava flows dated at 108 Ma (Frey et al., 2000; Ingle et al., 2002). Lastly, seismic refraction data from the southern Kerguelen Plateau produce velocity profiles that support a possible continental affinity (Operto & Charvis, 1996; Gohl et al., 2007; Leitchenkov et al., 2014). In regards to our plate model, these observations suggest that the southern Kerguelen Plateau was initially attached to the Indian plate until a northward ridge jump, shortly after M0r (120.6 Ma) time, attached the Kerguelen Plateau to the EANT plate. This model also suggests that no significant amount of pre-Cretaceous Normal Superchron (>120.6 Ma) oceanic crust exists offshore the margin of eastern India, as it was transferred to the EANT and AUS plates via the ridge jump.

Line	**Year**	**Ship**	**Previous Publications**
lusi7d	1963	Argo	Rabinowitz et al. (1983) Cochran (1988) Eagles & Konig (2008)
gcdsdp25	1974	Glomar-Challenger	Segoufin & Patriat (1980) Rabinowitz et al. (1983) Cochran (1988)
jco1	1980	Jean Charcot	Segoufin & Patriat (1980)
ga04	1980	Gallieni	Segoufin & Patriat (1980)
ve3619b	1983	Vema	Rabinowitz et al. (1983) Cochran (1988) Eagles & Konig (2008)
ve3619c	1983	Vema	Rabinowitz et al. (1983) Cochran (1988) Eagles & Konig (2008)
ve3619d	1983	Vema	Rabinowitz et al. (1983) Cochran (1988) Eagles & Konig (2008)

Table 2.1 Somali Basin ship tracks.

2.5 METHODOLOGY

2.5.1 Somali Basin Magnetics

Ten ridge-perpendicular Somali Basin ship tracks were modeled for magnetic anomaly identification (Figs. 2.7 & 2.8). This compilation includes 6 ship tracks used by Rabinowitz et al. (1983), 2 additional ship tracks used by Segoufin & Patriat (1980), and 2 unpublished ship tracks (Royer; pers. comm.). These ten ship tracks (Table 2.1) give us confidence in our ability to resolve appropriate anomaly interpretations. Magnetic anomalies were identified by comparing ship track data with a synthetic magnetic anomaly profile calculated using ModMag magnetic modeling software (Mendel et al., 2005). For our interpretations we used the timescale of Gee and Kent (2007). Table 2.2 summarizes the input parameters used in ModMag to calculate the synthetic magnetic anomaly profiles. Shiptrack and parameter data files (.dxypa and .dat) used for ModMag modeling are available in the supplementary data. Along each ship track (Fig. 2.7), the "Distance from Ridge" refers to the ridge perpendicular distance from the extinct ridge previously identified via satellite gravity data (Fig. 2.4). The depths to magnetic source were calculated by adding the estimated sediment thickness (Whittaker et al., 2013) to the measured bathymetry at each data point along the ship track.

Spreading Direction:	179.2372°	Depth to Source:	4.0 km (or from ship track data)
Source Layer Thickness:	0.5 km	Magnetization of blocks (On-Axis):	8.0 A/m
Magnetization of blocks (Off-Axis):	4.0 A/m	Contamination Coefficient:	0.5
Present Day Declination:	-3.6328°	Present Day Inclination:	-37.2007°
Formation Latitude:	-33.2958°	Formation Strike:	-89.4329° (90.5671°)
Coefficient of thermal subsidence equation:	0.35	Time Scale:	Gee & Kent (2007)

Table 2.2 Magnetic modeling input parameters.

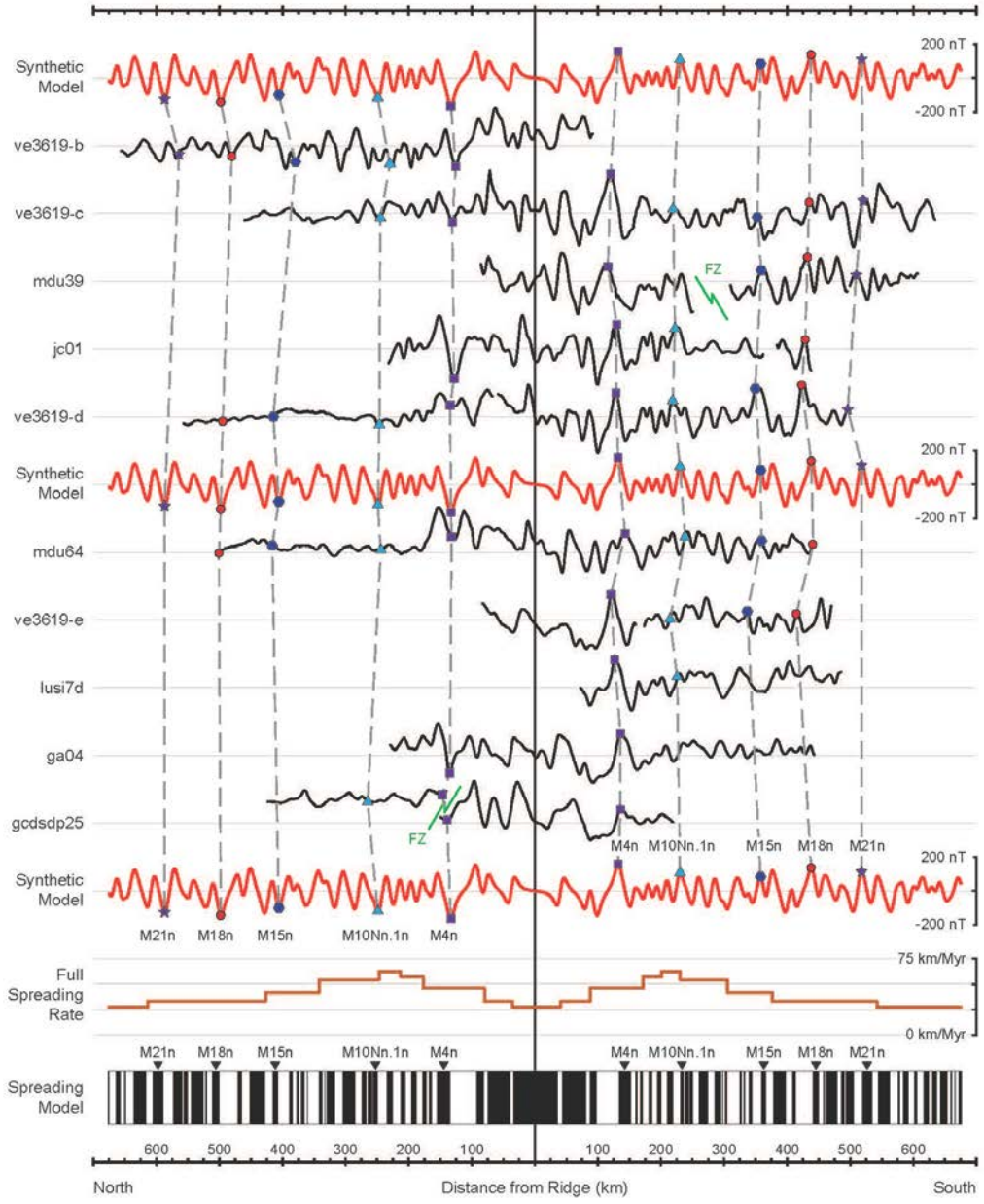

Figure 2.7 Magnetic profiles & magnetic model

Our proposed seafloor spreading model for the Somali Basin. Ridge perpendicular ship tracks (black) and synthetic (red) magnetic anomaly profiles are plotted above our spreading rate model. “Distance” refers to the ridge-perpendicular distance from the identified extinct ridge axis. Ship tracks are plotted with the easternmost ship track at the top, and westernmost ship track at the bottom. Select magnetic picks are shown in their location along the ship track. Parameters used to create the synthetic magnetic profile are summarized in Table 2.

As previously stated, an appropriate synthetic magnetic profile for the Somali Basin is anti-symmetric due to the dominance of the horizontal magnetic field component and the North–South spreading direction. Because of this anti-symmetry, we found it easier to pick the peaks and troughs at the young end of almost all of the magnetic anomalies. Only for magnetic anomaly M0r (120.8 Ma) did we pick the middle of the chron, as this coincided with a more easily identifiable inflection point in the profile. Magnetic anomaly M4n (125.67Ma) was ubiquitous and easily identifiable throughout the basin and provided a key foundation for our interpretations. Additionally, anomalies M10Nn.1n (129.63 Ma), and M15n (135.57 Ma), were distinct and identifiable throughout the basin. Magnetic identifications in the older, northern portions of the basin were often difficult because of the subdued nature of the magnetic anomalies (ve3619-d, mdu64, ve3619-e). These subdued profiles likely result from a deep basement magnetic source and a large thickness of sediments. However, we feel confident in our identification of the shallow peaks/troughs within these subdued profiles as these picks provide spreading rates consistent with those observed along more distinct profiles and are in agreement with our overall spreading model. Using our best spreading model (Fig. 2.7), we identify 300 magnetic anomalies, from M24Bn (152.43 Ma) to M0r (120.8 Ma; Fig. 2.8), with the oldest conjugate magnetic anomalies identified as M18r (141.22 Ma) within the Somali Basin.

These 300 magnetic anomaly picks greatly improve the coverage and resolution of magnetic anomaly identifications throughout the Somali Basin. Identification of the youngest magnetic anomalies, such as M0r and M4n, are similar to the interpretations of Segoufin & Patriat (1980) and Cochran (1988). Anomalies older than M4n show little similarity between the studies. The dissimilarity between interpreted anomalies results from this study's generally higher predicted spreading rates (Fig. 2.7; maximum of 62.67

km/Myr) compared to the slower rates (maximum of 34.0 km/Myr) suggested by Segoufin & Patriat (1980) and Cochran (1988).

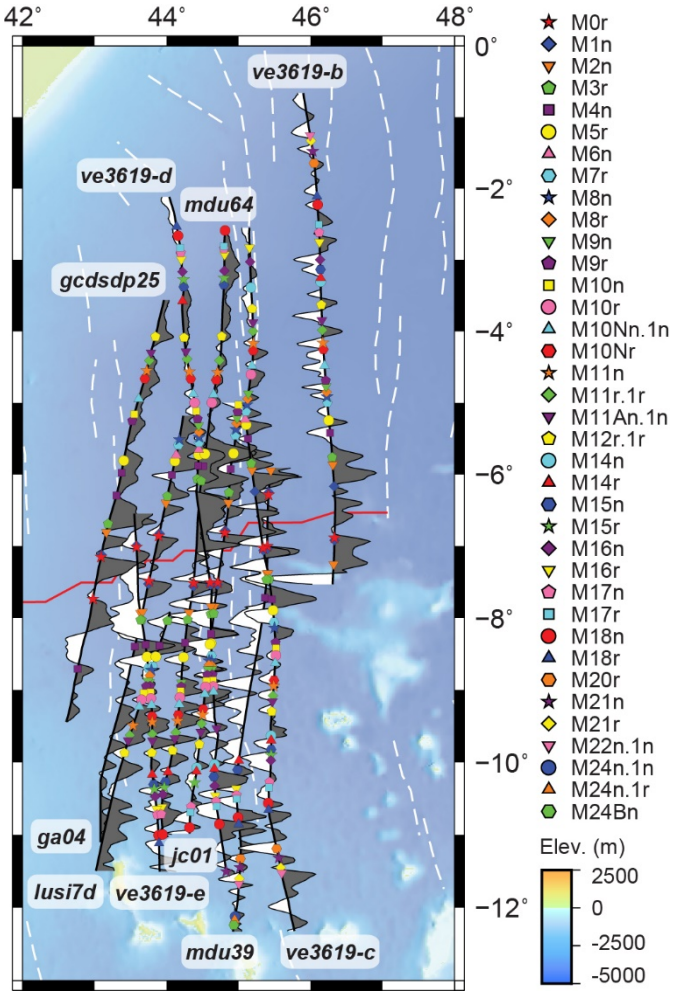

Figure 2.8 Somali Basin magnetics and ship track wiggles

North–South ship tracks and wiggles are plotted over Somali Basin bathymetry. Positive magnetic anomalies are shown as filled dark gray wiggles on the east side of the ship track, while negative anomalies are shown with white fill on the west side of the ship track. An extinct spreading ridge (thin red line) and seafloor fabric (dashed white line) were identified using satellite gravity data and shown in detail in Fig. 4. Magnetic picks from this study are overlain on the ship tracks and can be identified from the legend on the right. For the Somali Basin, most of the magnetic picks were made at the peaks and troughs coinciding with the young end of all magnetic isochrons. The only exception is our picking of M0r, which was picked at the inflection point coincident with the middle of the chron. Ship tracks and magnetic picks can be downloaded in the supplementary data.

2.5.2 Building a Plate Model

To build a regional plate model, we integrate our magnetic anomalies and seafloor fabric interpretations from the Somali Basin with previously published geophysical observations from the other early Indian Ocean basins. Any plausible early Indian Ocean plate model should begin from a constrained pre-breakup Gondwana geometry, match fracture zones and magnetic anomalies within the multiple spreading systems, and avoid improbable plate motions and plate configurations. We develop our plate model by first constructing a pre-breakup fit of the relevant Gondwana terrains (Fig. 2.10a) and then model post breakup terrain movement going forward in time (Fig. 2.10b–f). As we work forward in time, we visually match seafloor fabric and successive magnetic anomalies within the Mozambique Basin, Somali Basin, and Perth Abyssal Plain spreading systems using GPLATES plate modeling software (Boyden et al., 2011). For as long as it is possible, we attempt to maintain a cohesive East Gondwana configuration and visually match the geophysical observations in both the Somali and Mozambique basin systems, at a given time, using a single East Gondwana total reconstruction pole (TRP). When we can no longer match anomalies within both basins, we allow MAD/IND to move separately from EANT/AUS. The subsequent motion of MAD/IND is constrained using data in the Somali Basin systems, while EANT/AUS motion is constrained by data within the Mozambique Basin system. Therefore, any divergent motions that occur between MAD/IND and EANT/AUS are an output of this plate model, rather than an input. This output can be verified through comparison with geophysical observations from the Perth Abyssal Plain and EANT margin, and can aid future work deciphering their evolution.

A plausible pre-breakup fit of the plates comprising Gondwana is crucial to deciphering their subsequent breakup history. It is important to note that the pre-breakup fit of Gondwana is still an area of active research and discussion (Fritz et al., 2013; Collins

et al., 2014; Reeves, 2014). Our fit of Gondwana (Fig. 2.10a) attempts to honor generally accepted pre-breakup connections between the various plates (Smith & Hallam, 1970; Lawver et al., 1998; Reeves et al., 2002), utilize palinspastic restorations where available, and restrict overlap to regions of thinned continental crust along the present-day plate margins. To match EANT and IND, we follow Veevers (2009) palinspastic restoration and align the western boundary of the Napier Complex to the southern extent of the Dharwar Craton, the Robert Glacier to the Pranhita–Godavari Rift, Prydz Bay and the Lambert Graben to the Mahanadi Rift, and the Vestfold Hills/Rauer Block to the Singhbhum Craton. SL is matched to IND by arranging the northeast limit of the Highland Complex (Cooray, 1994) next to the southwest extent of the Trivandrum/ Nagercoil Block (Collins et al., 2014). Within this fit, SL is placed between Gunnerus Ridge, EANT, and IND. We connect MAD to IND through the proposed continuation of the Betsimisaraka Shear Zone with the Kumta Suture and the Coorg Shear Zone after Ishwar-Kumar et al. (2013). The existence of the Betsimisaraka Shear Zone has recently been called into question (Tucker et al., 2014). However, the fits of MAD–IND as proposed by Tucker et al. (2014) and Ishwar-Kumar et al. (2013) appear to have negligible differences, and thus our fit should be valid regardless of the existence of the Betsimisaraka Shear Zone. SOM and MAD are fitted through the alignment of the Marda Fault Zone (Boccaletti et al., 1991) with the Adreaparaty Thrust (Collins et al., 2014; Tucker et al., 2014) which together may represent the eastward extent of the proposed Azania block (Collins & Pisarevsky, 2005). SL and AFR are matched by aligning the Vijayan Block with the Nampula Block (Reeves & De Wit, 2000; Collins et al., 2014). Lastly EANT and AFR are fitted by aligning the southern extent of the Kalahari Craton with the westward extent of the Grunehogna Craton (Reeves et al., 2002; Hanson et al., 2004; Board et al., 2005).

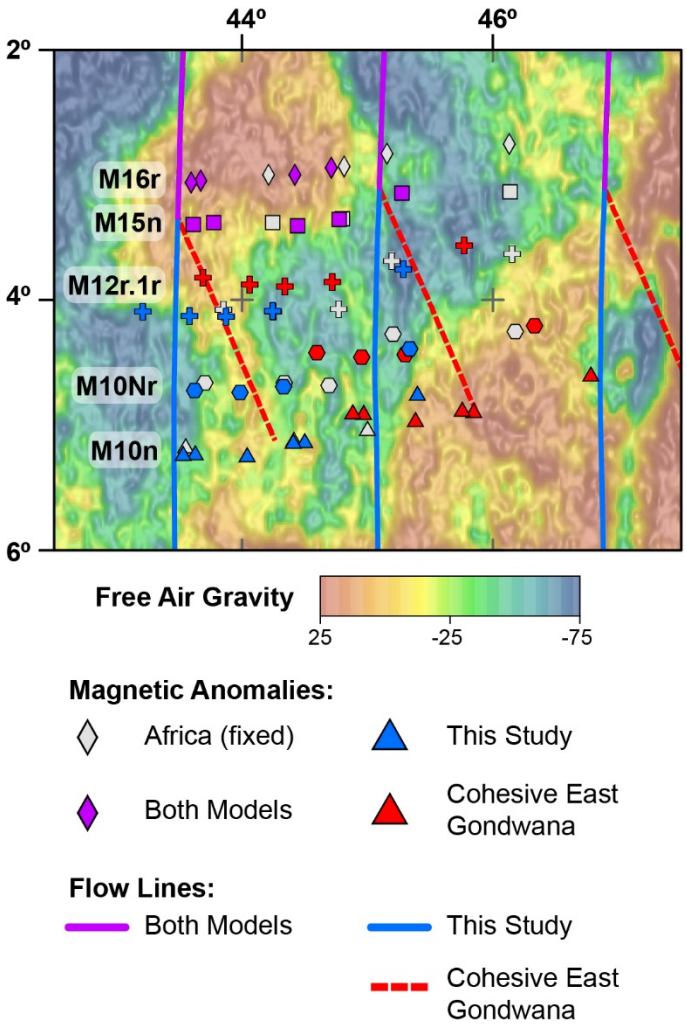

Figure 2.9 Comparison of Somali Basin flow lines and rotated magnetic anomalies

Somali Basin flow lines and rotated Madagascar magnetic anomalies are compared as predicted by This Study (blue) against a hypothetical Cohesive East Gondwana model (red). Africa is kept fixed and magnetic anomaly picks from the north side of the extinct Somali Basin spreading ridge are shown in gray. The Cohesive East Gondwana model is based upon keeping MAD/IND fixed to EANT/AUS and matching geophysical constraints in the Mozambique Basin. For anomalies M15n and older, both models produce identical and acceptable flow lines (purple solid lines) and magnetic anomalies matches (purple diamonds and squares). After M15n in the Cohesive East Gondwana model, constraints from the Mozambique Basin force MAD to deviate eastward (red dashed lines) and produce an unacceptable mismatch of the magnetic anomalies (red crosses, hexagons, and triangles). This study's model produces satisfactory flow lines (blue solid lines) and matches between the rotated Madagascar magnetic anomalies (blue crosses, hexagons, and triangles) and their African counterparts (gray crosses, hexagons, and triangles) by allowing MAD/IND to rotate independent of EANT/AUS after M15n.We end the comparison at anomaly M10n, which is the minimum possible age of East Gondwana cohesion based on the establishment of seafloor spreading the Perth Abyssal Plain (Williams et al., 2013).

Within our plate model, we begin to move East Gondwana southward away from a fixed AFR following emplacement of the Karoo Large Igneous Province at 182 Ma (Jourdan et al., 2007). Our best constraints on the early motion of East Gondwana come from the seafloor fabric and the detailed magnetic anomalies of Leinweber & Jokat (2012) in the Mozambique Basin system. We utilize these data to move EANT relative to AFR from the start of seafloor spreading at M25n (153.71 Ma) to the start of the Cretaceous Normal Superchron (120.6 Ma). Through the visual matching of rotated conjugate magnetic anomalies within the Mozambique Basin system, we produce total reconstruction poles (TRPs) describing EANT–AFR motion at M25n (153.71 Ma), M22n.1n (147.815 Ma), M15n (135.76 Ma), M11An.1n (132.13 Ma), M4n (126.12 Ma), M2n (123.8 Ma), and M0r (120.8 Ma). The development of the Mozambique Basin is shown in Fig. 2.10b–f.

In order to determine if East Gondwana rifted from West Gondwana as a cohesive unit, we test how well the Mozambique Basin TRPs are able to match conjugate magnetic anomalies from the Somali Basin, while maintaining a single East Gondwana plate. The oldest magnetic anomaly interpreted in the Somali Basin is M24Bn (152.43 Ma) with the oldest conjugate magnetic anomaly pair at M18r (141.22 Ma).We found that for M18r (141.22 Ma) through M15n (135.76 Ma), we can match conjugate magnetic anomalies and seafloor fabric in both the Mozambique and Somali Basin systems using a single East Gondwana plate (Fig. 2.9). Following M15n (135.76 Ma) we are unable to match both the magnetic anomalies and seafloor fabric in the two basins using a single East Gondwana plate (Fig. 2.9). Thus after M15n (135.76 Ma) we assume MAD/IND and EANT/AUS moved as independent plates as constrained by geophysical observations in the Somali and Mozambique Basin systems respectively. Based on our geophysical interpretations within

the Somali Basin system, we define new TRPs for MAD relative to Somalia (SOM) at M15n (135.76 Ma), M11An.1n (131.91 Ma), M7r (127.49 Ma), M4n (125.67 Ma), M2n

Fixed Plate	Moving Plate	Age	Latitude	Longitude	Angle
S. Africa	Somalia	>182-<120.6	-20.39	34.32	0.69
Somalia	Madagascar	182	4.22	98.05	-19.79
		153.71	-1.97	92.1	-16.4
		147.815	-3.19	89.69	-14.6
		135.76	-3.84	85.11	-10.55
		131.91	-3.84	85.11	-8.16
		127.49	-3.84	85.11	-4.61
		125.67	-3.84	85.11	-3.56
		123.55	-3.84	85.11	-2.23
		120.8	0.19	-67.71	0.75
		120.6	0.19	-67.71	0.70
Madagascar	India	>182-<120.6	-21.54	-155.79	57.89
India	Sri Lanka	182	10.83	82.49	-24.23
		135.76	10.83	82.49	-24.23
		120.6	10.91	79.79	-27.38
S. Africa	E. Antarctica	182	9.73	148.36	-58.03
		153.71	-9.42	-29.37	54.12
		147.815	-10.11	-28.48	52.62
		135.76	-12.45	-25.34	50.13
		132.13	-11.98	-25.56	48.65
		126.12	-10.64	-26.18	44.84
		123.8	-9.71	-26.8	43.37
		120.8	-8.33	-27.72	41.74
		120.6	-8.28	-27.78	41.61
E. Antarctica	Australia	182	-2	38.9	-31.5
		125	-2	38.9	-31.5
		120.6	-0.66	38.17	-30.89

Table 2.3 Plate model total rotation poles

(123.55 Ma) and M0r (120.8 Ma). Use of the separate Mozambique and Somali Basin TRPs, produces significant divergence between the MAD/IND and EANT/AUS plates by M10n (128.93; Fig. 2.10e) coincident with the establishment of the seafloor spreading systems offshore wAUS. In our plate model, magnetic anomalies in the western Perth Abyssal Plain (Williams et al., 2013) move with IND assuming later attachment to the AUS plate via ridge jumps at ~119 Ma and ~105 Ma. By the start of the Cretaceous Normal

Superchron (120.6; Fig. 2.10f), seafloor spreading in the Somali Basin has begun to slow, leading to further divergence between IND and EANT/AUS and the creation of much of the Enderby Basin. Rotation parameters for our plate model are shown in Table 2.3 and an animation of this model is available in the online supplementary data for this paper.

2.6 DISCUSSION

New geophysical observations from the Somali Basin have significant implications for the evolution of the early Indian Ocean. Our magnetic interpretations in the Somali Basin system are similar in age, geometry, spreading rate, and spreading direction to those observed in the coeval Mozambique Basin system (Leinweber and Jokat, 2012). Through integration in a plate model, we find that the conjugate geophysical interpretations within both basins can be matched, through anomaly M15n (135.76Ma), using rotation poles for a single East Gondwana plate (Fig. 2.9). This similarity in seafloor spreading character, and ability to match conjugate data in multiple basins with a single rotation pole, strongly suggests that East Gondwana rifted from West Gondwana as a cohesive unit. Maintaining an appropriate East Gondwana geometry that utilizes a single rotation pole to match geophysical data in both the Mozambique and Somali Basins helps resolve uncertainty concerning the exact orientation of East Gondwana relative to AFR. Post-M15n (135.76 Ma) geophysical interpretations require separate MAD/IND and EANT/AUS motion (Fig. 2.9) and provides constrained evidence for the likely start of East Gondwana breakup.

Divergence between MAD/IND and EANT/AUS arises naturally as an output of our plate model. The timing and direction of this divergence strongly agrees with observations from the margins of wAUS and from the Enderby Basin (EANT). The counter-clockwise motion of IND away from EANT/AUS predicted by our model, agrees

with fracture zones observations from wAUS. M10n (128.93Ma) and younger magnetic interpretations from the western Perth Abyssal Plain are attached to the IND plate and modeled using ridge jumps nearly identical in age to those suggested by Williams et al. (2013). After attachment to the IND plate, the conjugate IND and AUS anomalies from the Perth Abyssal Plain can be adequately matched using the previously defined TRPs for the MAD/IND and EANT/AUS plates. Since these TRPs are based on geophysical data in the Mozambique and Somali Basin systems, being able to match these Perth Abyssal Plain anomalies gives us confidence that our model is accurately resolving the appropriate relative motion and orientations of the two separate plates. Further our plate model predicts progressive rifting between IND and EANT, which may explain many geophysical observations from the Enderby Basin. Based on our plate model, IND rotates counter-clockwise away from EANT. Therefore in the eastern Enderby Basin, rifting is able to establish early seafloor spreading and form oceanic crust in the Princess Elizabeth Trough prior to the start of the Cretaceous Normal Superchron (120.6 Ma). In the central Enderby Basin, rifting is accommodated through the extension of continental crust out to the Enderby Basin Anomaly. This wide zone of continental extension, leaves little room for oceanic crust production prior to the start of the Cretaceous Normal Superchron (120.6 Ma), and can explain the lack of clear magnetic anomalies throughout much of the Enderby Basin (Golynsky et al., 2013). Our model predicts minimal extension in the western Enderby Basin between Sri Lanka (SL) and EANT, in agreement with detailed aeromagnetic surveys that were unable to identify any M-Series anomalies (Jokat et al., 2010) within the region. Given that the breakup of East Gondwana is an output of our plate model, we are satisfied with our ability to constrain seafloor spreading between MAD/IND and EANT/ AUS and explain geophysical observations from the wAUS and EANT margins.

Lastly, we hope our model can aid efforts to interpret the aeromagnetic data acquired within the Princess Elizabeth Trough (Gohl et al. 2007). Our plate model predicts that rifting between IND– EANT began after M15n (135.76 Ma) and that by M10n (128.93 Ma) the IND continent was outboard of the continental margin of EANT in the Princess Elizabeth Trough region. From these observations we expect that the oldest magnetic anomalies within the Princess Elizabeth Trough are likely to be between M11n (130.8 Ma) and M10n (128.93Ma). Additionally, our plate model may provide first order estimates of spreading rates during the early breakup of IND–EANT. We estimate full spreading rates of 7.5 km/Myr at 135 Ma, increasing to 15 km/Myr at 125 Ma, and finally accelerating to 37.5 km/Myr by 120.6 Ma between IND and EANT in the Princess Elizabeth Trough region.

2.7 CONCLUSIONS

1) Geophysical interpretations are made in the Somali Basin that utilize recent free-air-gravity data. We have identified seafloor fabric including fracture zone traces and an extinct spreading ridge. Using a basin-wide compilation of ship track magnetic data we make detailed magnetic anomaly identifications from M24Bn (152.43 Ma) to M0r (120.8 Ma). These new interpretations help constrain Somali Basin seafloor spreading and prove useful for understanding the tectonics of the early Indian Ocean.

2) Magnetic anomalies in the coeval Somali and Mozambique Basin systems have been integrated to understand the motion and fragmentation of East Gondwana. From breakup through anomaly M15n (135.76 Ma), conjugate geophysical data within both the Somali Basin and Mozambique Basin systems show similar spreading characteristics and can be matched using a single pole of rotation for East Gondwana. This spreading similarity

and ability to match geophysical observations within the older portions of the basin strongly support previous assertions that East Gondwana rifted from West Gondwana as a single cohesive unit.

3) To match data younger than M15n (135.76 Ma), in the Mozambique and Somali Basin systems, separate MAD/IND and EANT/AUS plates must be used. The inability to define a single rotation pole for East Gondwana, that would match data in both basins, provides constrained circumstantial evidence that East Gondwana began to rift from the east to the west shortly after M15n (135.76 Ma). We constrain the post-M15n (135.76 Ma) motions of MAD/IND and EANT/AUS as independent plates and predict a slow counter clockwise motion of IND away from the margins EANT/AUS. This separation, predicted by our plate model, agrees with geophysical observations from offshore wAUS and EANT without the need for previously postulated two-way plate motions or improbable plate geometries.

ACKNOWLEDGEMENTS

This work was supported by the PLATES Project at the Institute for Geophysics. The PLATES Project supports research in plate reconstruction and is funded by a consortium of industry sponsors. PLATES sponsors had no involvement in the collection or interpretation of the data presented in this study. This is UTIG Contribution #2957. We thank the anonymous reviewers for their help in refining this paper.

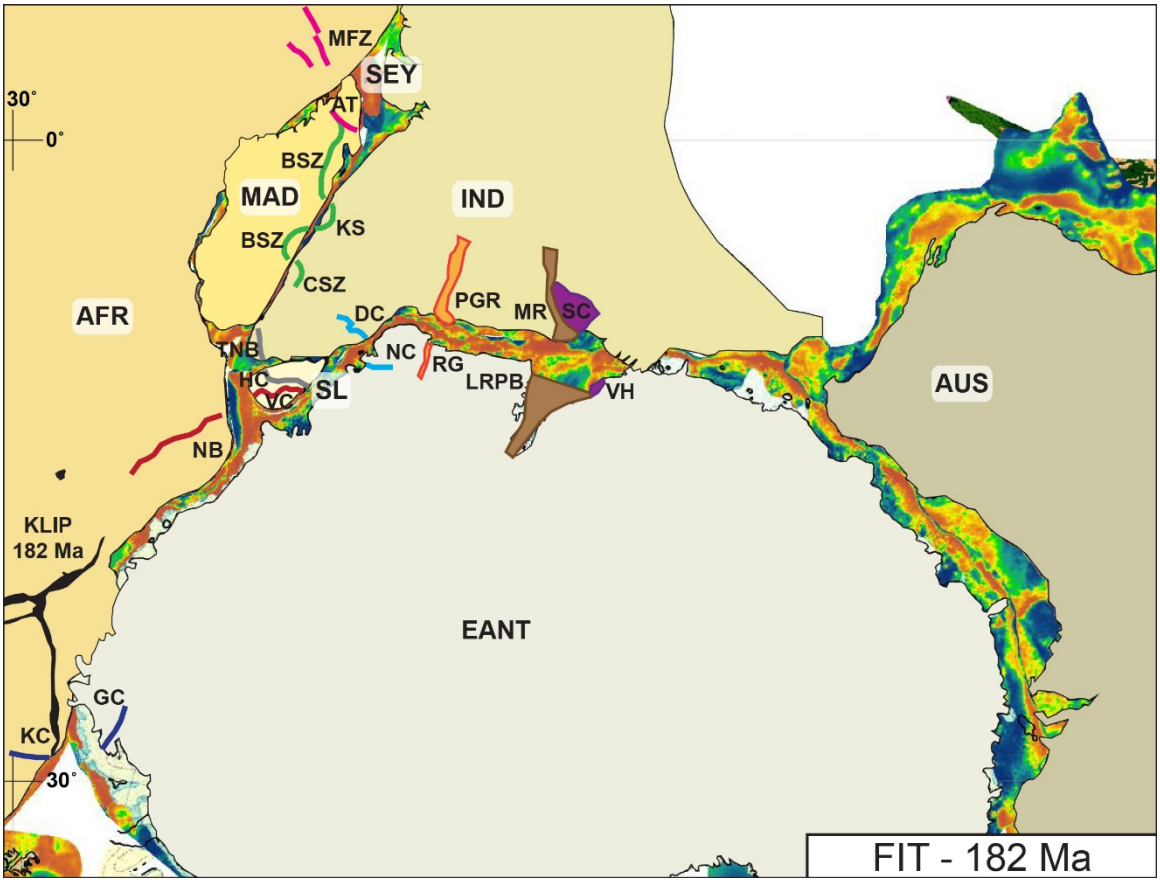

Figure 2.10a Gondwana fit (>182 Ma)

Pre-breakup fit of Gondwana in Mercator Projection with Africa fixed. Some of the lineaments and terrains used to construct our fit are shown as follows: Pink line: Madra Fault Zone (MFZ) & Adreaparaty Thrust (AT); Green line: Betsimisaraka Shear Zone (BSZ), Kumta Suture (KS), Coorg Shear Zone (CSZ); Gray line: Trivandrum/ Nagercoil Block (TNB), Highland Complex (HC); Red line: Nampula Block (NB), Vijayan Block (VC); Dark blue line: Kalahari Craton (KC), Grunehogna Craton (GC); Light blue line: Darwar Craton (DC), Napier Craton (NC); Orange polygon: Pranhita–Godavari Rift (PGR), Robert Glacier (RG); Brown polygon: Mahanadi Rift (MR), Lambert Rift/Prydz Bay (LRPB); Purple polygon: Singhbhum Craton (SC), Vestfold Hills (VH); Black Polygon: Karoo Large Igneous Province (KLIP).

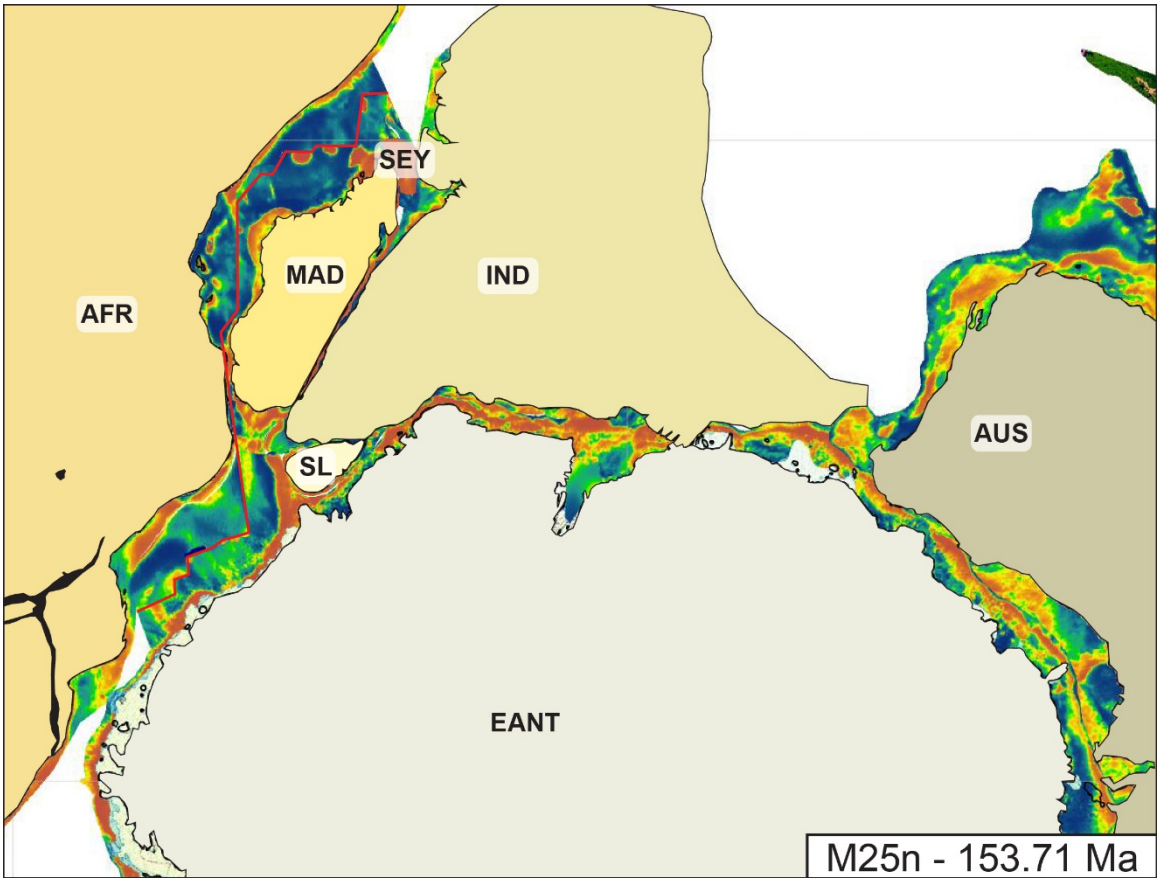

Figure 2.10b Mozambique Basin seafloor spreading (M25n—153.71 Ma)

East Gondwana rifts southward from AFR as a single cohesive unit. Seafloor spreading begins in the Mozambique Basin byM25n (153.71Ma; Leinweber and Jokat, 2012). A hypothetical spreading ridge (solid red line) distinguishes the satellite gravity data Sandwell et al. (2014) between the conjugate basins.

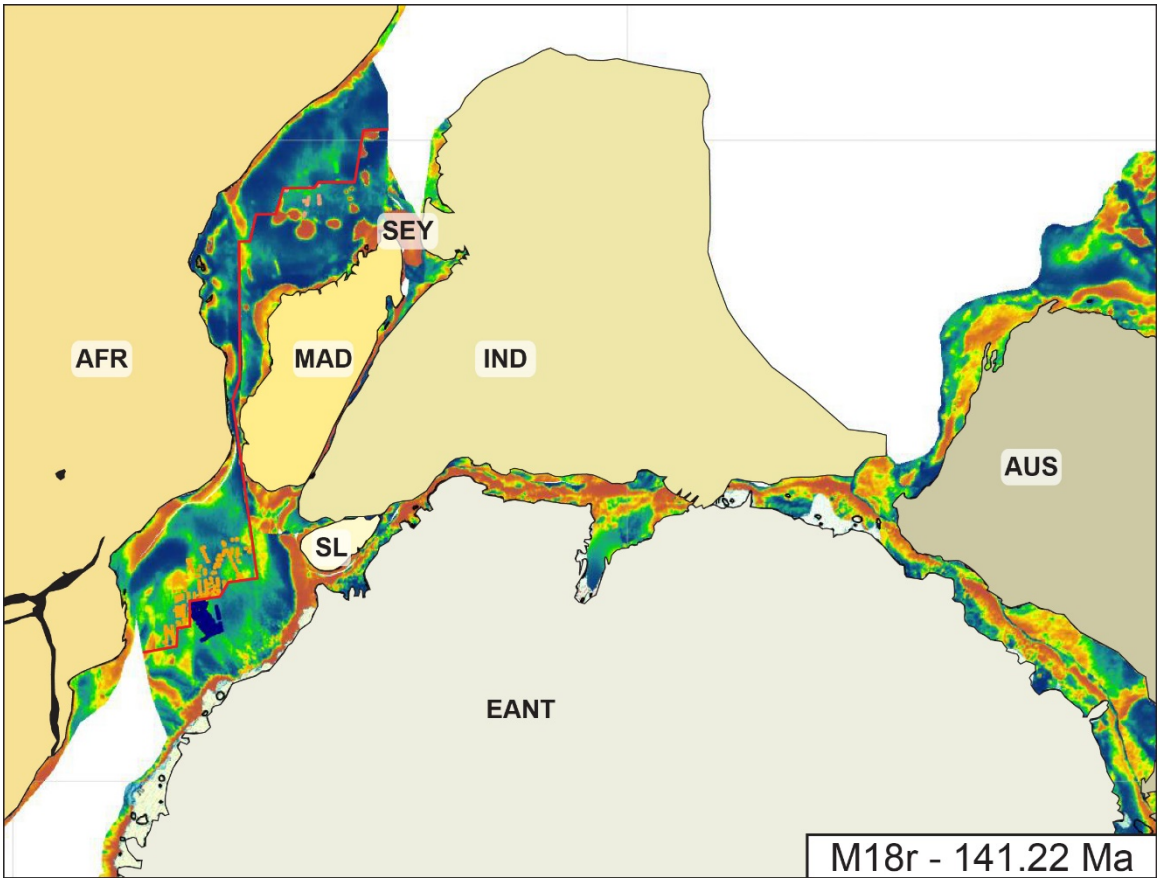

Figure 2.10c Somali Basin seafloor spreading (M18r—141.22 Ma)

Although, seafloor spreading begins in the Somali Basin at M24Bn (152.43 Ma; this study), the first conjugate magnetic anomalies don't appear until M18r (141.22 Ma; this study). Conjugate magnetic anomalies in both the Somali Basin and in the coeval Mozambique Basin are matched using a single pole of rotation for East Gondwana. Solid Red Line —Spreading Ridge Axis.

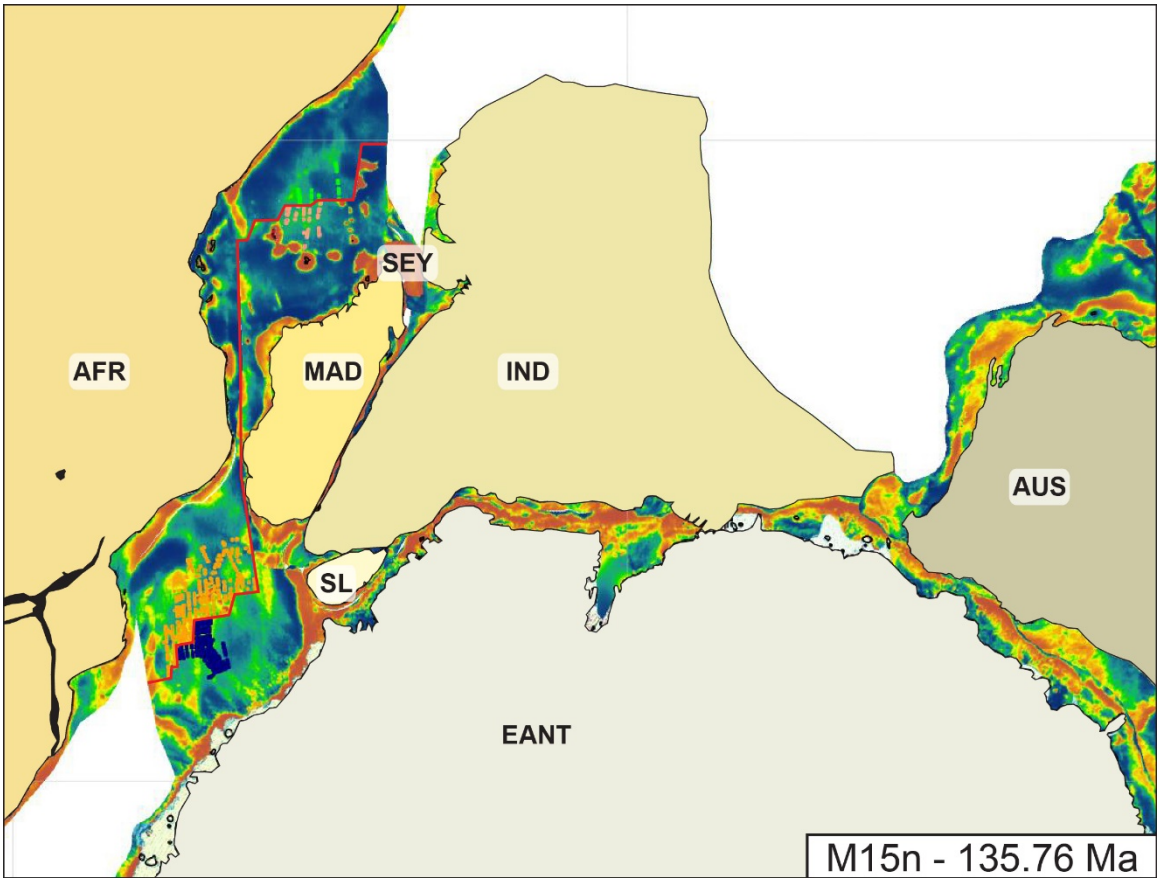

Figure 2.10d East Gondwana breakup begins (M15n — 135.76 Ma)

After anomaly M15n, it is no longer possible to match geophysical observations in the Mozambique and Somali Basins using a single pole of rotation for East Gondwana. Following M15n (135.76 Ma), Madagascar and India begin to move together as an independent plate constrained by our Somali Basin magnetic anomaly interpretations. Concurrently, East Antarctica and Australia move as an independent plate as constrained by Mozambique basin magnetic anomalies (Leinweber and Jokat, 2012). Divergent motion between the Madagascar/India and East Antarctica/Australia plates, (i.e. the breakup of East Gondwana) begins directly after M15n. Solid Red Line — Spreading Ridge Axis.

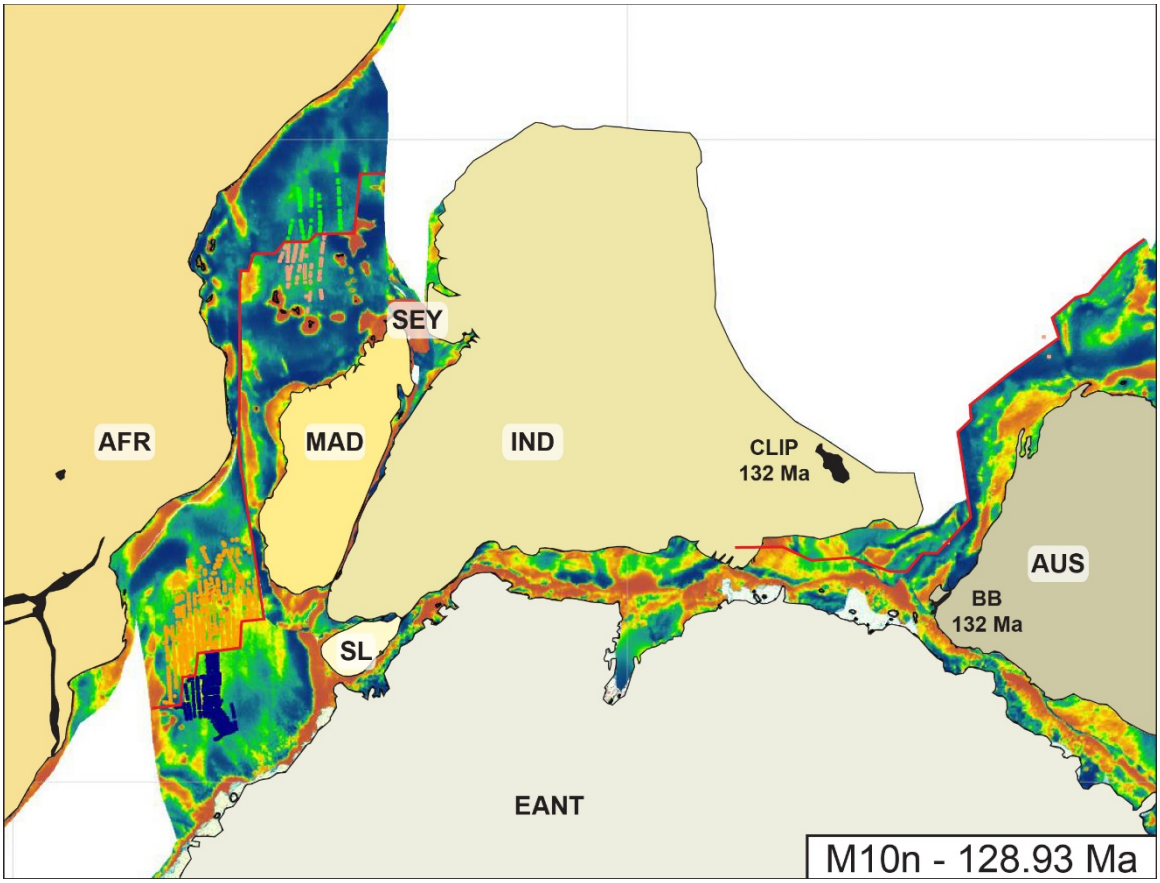

Figure 2.10e West Australia seafloor spreading (M10n — 128.93 Ma)

Divergent counter-clockwise motion of Madagascar and India relative to East Antarctica and Australia predicted using only constraints from the Somali and Mozambique Basins. The relative counter-clockwise motion of Madagascar/India from East Antarctic/Australia agrees well with observed fracture zones azimuths offshore West Australia. The magnitude of this predicted divergence agrees with magnetic anomaly interpretations offshore West Australia that suggest seafloor spreading became established around M10n (128.93 Ma; Gibbons et al., 2012; Williams et al., 2013). Divergence between India and East Antarctica in the Enderby Basin ranges from ~230 km of extension in the East to ~80 km in the West. Solid Red Line — Spreading Ridge Axis.

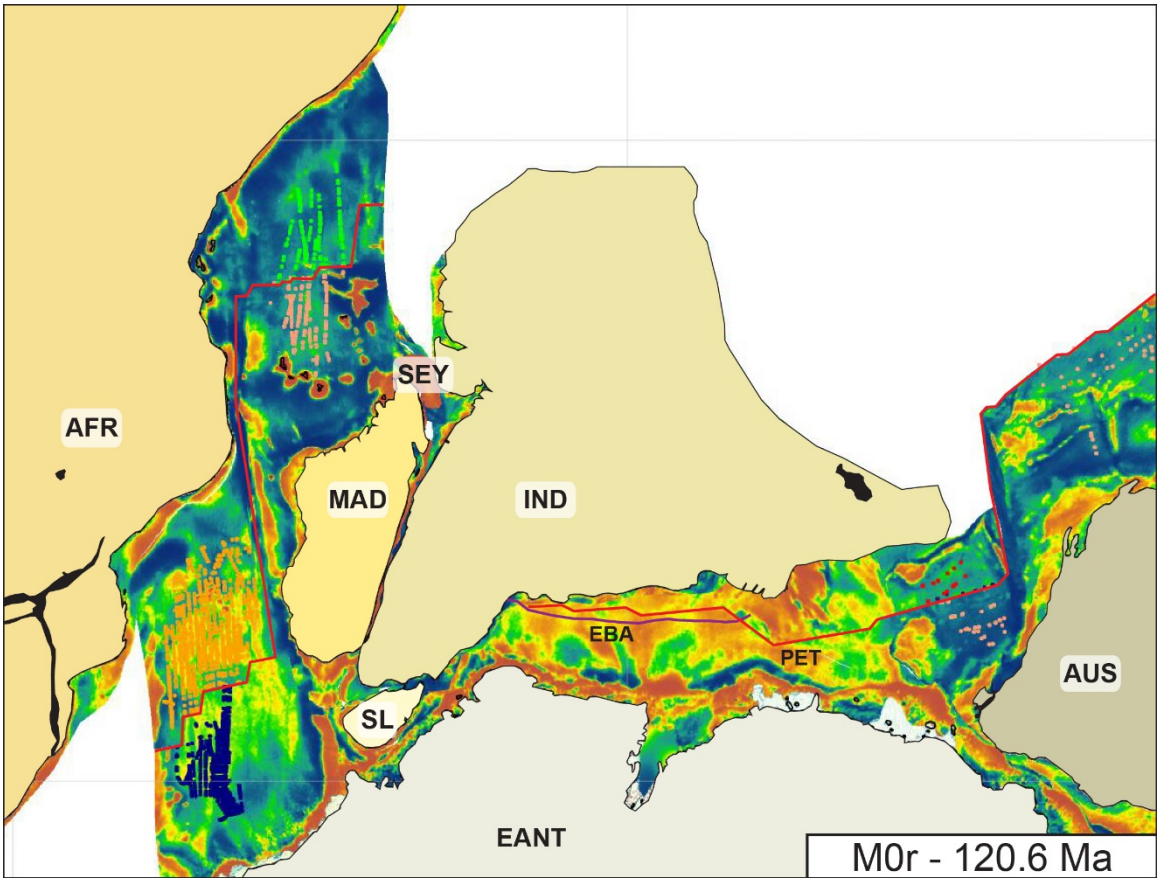

Figure 2.10f Start of the Cretaceous Normal Superchron (120.6 Ma)

We are able to match magnetic anomaly M0r (120.6 Ma) in the Mozambique, Somali, and West Australia basin systems, to obtain a constrained geometry of the Indian Ocean at the start of the Cretaceous Normal Superchron (120.6 Ma). In much of the Enderby Basin, extended continental crust out to the Enderby Basin Anomaly (EBA; thick purple line), leaves little room for oceanic crust prior to the start of the Cretaceous Normal Superchron. In the Princess Elizabeth Trough (PET), there is roomfor significant amounts of oceanic crust prior to the CretaceousNormal Superchron. These observations of oceanic crustal distribution may help explain the magnetic anomaly fabric observed within the Enderby Basin (Golynsky et al., 2013). Solid Red Line — Spreading Ridge Axis.

Chapter 3: The crustal structure of the Enderby Basin

ABSTRACT

The passive margins and ocean crust of the Enderby Basin, East Antarctica preserve a record of the breakup of East Gondwana. Using a suite of public domain geophysical data we have examined and described the crustal morphology of the basin. Based on our geophysical observations, we find that the Enderby Basin can be divided into three morphologic domains. The Eastern Domain demonstrates the most volcanic morphology of the basin, with abundant seaward dipping reflector packages and anomalously thick oceanic crust. These features suggest an early influence by the Kerguelen Hotspot on continental breakup within the domain. The Central Domain is characterized by two regions of oceanic crust of varying morphology segregated by a high amplitude magnetic anomaly. Geophysical observations suggest that the basement inboard of this magnetic anomaly is composed of thin, rugged, and poorly structured, proto-oceanic crust, similar in morphology to oceanic crust formed at ultraslow/slow mid-ocean ridged. Outboard of this anomaly, oceanic crust appears to be well-structured and of normal thickness. We offer three, non-exclusive, explanations for the observed change in ocean crustal structure: (1) melt production was low at continental breakup and the progressive decompression of the mantle induced an increase in production, (2) melt production was initially low to due lower extension rates and that melt production increased following a change in spreading rate, (3) a change in spreading ridge geometry led to more effective seafloor spreading and concurrent increase in melt production. The Western Domain of the Enderby Basin is characterized by abundant fracture zones and anomalously thin oceanic crust. We believe these features arose as a geometric consequence of the originally oblique orientation of

continental rifting relative to the extension direction within the domain. Together these observations suggest that during East Gondwana breakup, rifting processes were highly variable and produced spreading systems which reflect this variability.

3.1 INTRODUCTION

During the Early Cretaceous, East Gondwana began to internally fragment (McElhinny, 1970; McKenzie & Sclater, 1971). This rifting separated the combined blocks of Madagascar/India/Sri Lanka away from East Antarctica/Australia and ultimately formed the continental margins and ocean basins preserved today offshore eastern India, western Australia, and East Antarctica (Markl, 1974; Sclater & Fisher, 1974). The East Antarctic basins formed during this rifting occupy a domain stretching between Gunnerus Ridge in the west, and the Davis Sea in the east (Fig. 3.1; Stagg, 1985), For simplicity in the remainder of this paper, these Antarctic basins and seas, will be collectively referred to as the Enderby Basin. Despite being the subject of multiple geophysical investigations, the details of the tectonic development of the Enderby Basin still remains poorly constrained. Understanding this development can offer the critical insight into the fragmentation of East Gondwana, the early formation of the Indian Ocean, and supercontinent breakup processes.

Using public domain geophysical data including: satellite gravity, a compilation of marine and aeromagnetic anomaly data, sonobuoy velocity information, and a collection of long offset, post-stack, reflection seismic data, we have examined and described the crustal structure of the Enderby Basin. Previous works interpreting the crustal morphology of the Enderby Basin (Leitchenkov et al., 2014; Stagg et al., 2004) have postulated a wide, up to 500 km, domain of thinned continental crust outboard of the present-day coastline. Here we offer an alternative interpretation that proposes a narrower (150-275 km) domain

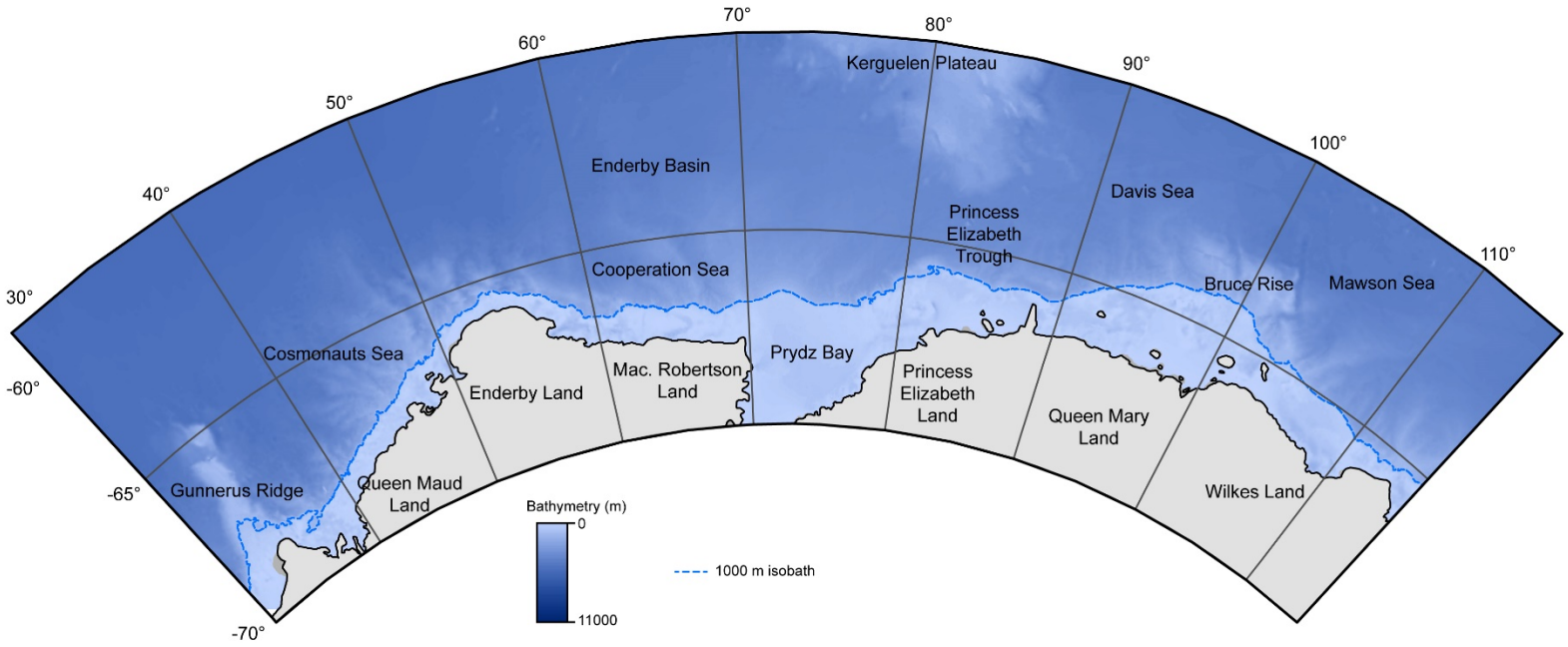

Figure 3.1 Overview of the Enderby Basin, East Antarctica

of thin continental crust, with a larger portion of the basin being of predominantly oceanic affinity. Much of the thin and rugged basement observed within the deeper portions of the Enderby Basin, appears devoid of any isostatically observable crustal thinning, and is proposed to be composed of primarily proto-oceanic crust. Our preferred interpretation suggests that this proto-oceanic domain was formed shortly after continental breakup, when melt production rates were low. Only after the later reorganization of the magmatic system, was normal seafloor spreading between India and East Antarctica established and well-structured ocean crust formed.

3.2 BACKGROUND

Marine magnetic anomalies in the Somali and Mozambique Basins indicate East Gondwana fragmentation likely began by M15n times (135.76 Ma; Davis et al., 2016). Magnetic anomalies, M10n through M0 (Gibbons et al., 2012; Williams et al., 2013) and geochronologic dating of the Bunburry Basalts (132-130 Ma; Coffin et al., 2002) help to constrain the timing of rifting between Greater India and western Australia. However, it is not known if Greater India remained wholly attached to India during this East Gondwana fragmentation (Lawver et al., 1998). As such, direct evidence for the rifting of India and East Antarctica must come from the Enderby Basin. Remnant marine magnetic anomalies interpreted within the Enderby Basin (e.g., Gaina et al., 2007; Gibbons et al., 2013) show little agreement with holistic magnetic datasets and are considered suspect (Golynsky et al., 2013). Ocean Drilling Program drill sites within the Kerguelen Plateau provide the only direct age control within the Enderby Basin, with a maximum recovered basalt age of 119 Ma from the southern portion of the Kerguelen Plateau (Duncan, 2002). The abundant geophysical data collected within the Enderby Basin therefore provides the best path for

understanding the breakup of India and East Antarctica and early formation of the Indian Ocean.

Geophysical investigation of the Enderby Basin began in the 1970s and have been carried out by a variety of nations, including Australia, France, Germany, Italy, Japan, Norway, South Africa, the Soviet Union/Russia, and the United States. During the austral summers of 2000-2002, the Australian Antarctic and Southern Ocean Profiling Project collected a suite of geophysical data in an effort to define the outer limits of the continental shelf within the Australian Antarctic Territory. These data include deeply penetrating seismic reflection, shipboard potential field, and sonobuoy velocity information. Seismic reflection and shipboard magnetic anomaly data reveal that for much of the basin, a positive, high amplitude, magnetic anomaly is coincident with a step up in basement and with the landward limit of smooth, well-structured, oceanic crust (Stagg et al., 2004; Stagg et al., 2005; Stagg et al., 2006; O'brien & Stagg, 2007). Additionally, this Enderby Basin Anomaly (EBA; Golynsky et al., 2013) has been suggested to demarcate the boundary between outboard, higher velocity oceanic basement and inboard lower velocity continental crust (e.g., Stagg et al., 2004). As such, the Australian investigators proposed that for much of the Enderby Basin, the EBA represents the Continent Ocean Boundary (COB; Stagg et al., 2004). This interpretation suggests that between the present day coastline and EBA, there is a wide (up to 450 km) domain, of predominately thinned continental crust.

Other significant regional geophysical datasets collected in and around the Enderby Basin include cooperative Russian PMGE and Norwegian NPD seismic and potential field expeditions (Leitchenkov et al., 2008; Solli et al., 2008), Japanese shipborne magnetic investigations (Nogi et al., 2004), and German/International Geophysical Year '07-'08 helicopter magnetic surveys in the Gunnerus Ridge and Kerguelen Plateau regions (Gohl

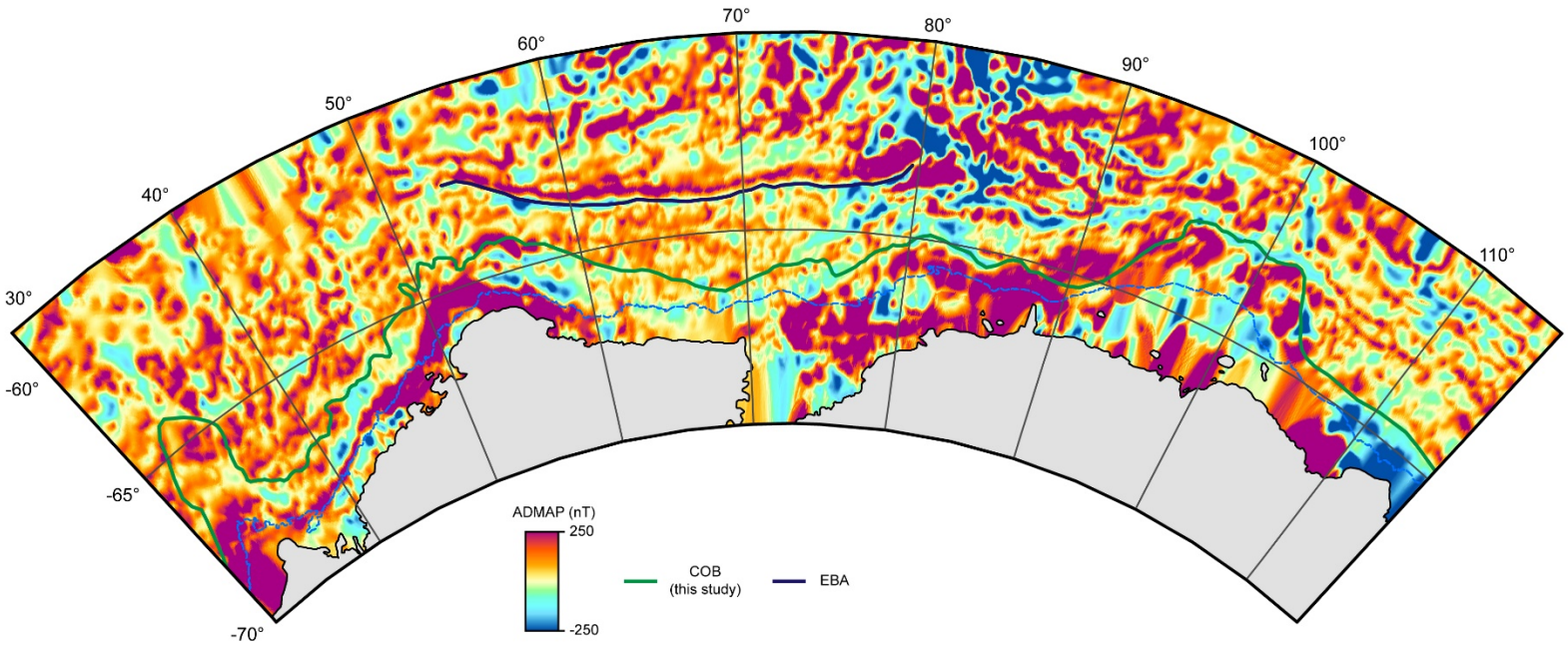

Figure 3.2 Antarctic Digital Magnetic Anomaly Project compilation

The Enderby Basin Anomaly (EBA) appears as a continuous high amplitude anomaly for much of the central part of the Enderby Basin. The preferred Continent Ocean Boundary (COB) of this study is shown in green.

et al., 2007; Jokat et al., 2010). Magnetic anomaly data from these and other surveys have been incorporated into the Antarctic Digital Magnetic Anomaly Project (Chiappini & von Frese, 1999; Golynsky et al., 2002; Golynsky et al., 2013). In the Enderby Basin, results from this magnetic compilation (Fig. 3.2) highlight the basin-wide geometry of the EBA, reveal high amplitude magnetic anomalies over portions of the continental shelf, and demonstrate an apparent lack identifiable remnant magnetic lineations (Golynsky et al., 2013). Crustal structure interpretations provided from Russian investigations (Leitchenkov et al., 2014) are similar to that proposed by Australian works, except with a slightly wider (up to 500 km) extent of thinned continental crust in the central portion of the Enderby Basin.

3.3 METHODS

3.3.1 Seismic Data and Seismic Interpretation

Using public-domain seismic data available through the Antarctic Seismic Data Library Service we have compiled a collection of post-stack, reflection, time data. The collection used for this work consists of 140 seismic lines (Fig. 3.3) that were found to consistently image the full sedimentary section down to the top of basement within our study area. The majority of this data comes from recent Australian, Russian, and Norwegian seismic surveys. The seismic data used in this compilation are listed in Supplementary Table 1 and with line naming conventions following from that on the Seismic Data Library. All horizon interpretations were conducted within the time domain. On most lines the top of basement was well imaged. On some seismic lines collected over thick sedimentary packages, the water-bottom multiple obscured a clear interpretation of the top of basement, as such a best estimate of basement depth was made by linearly

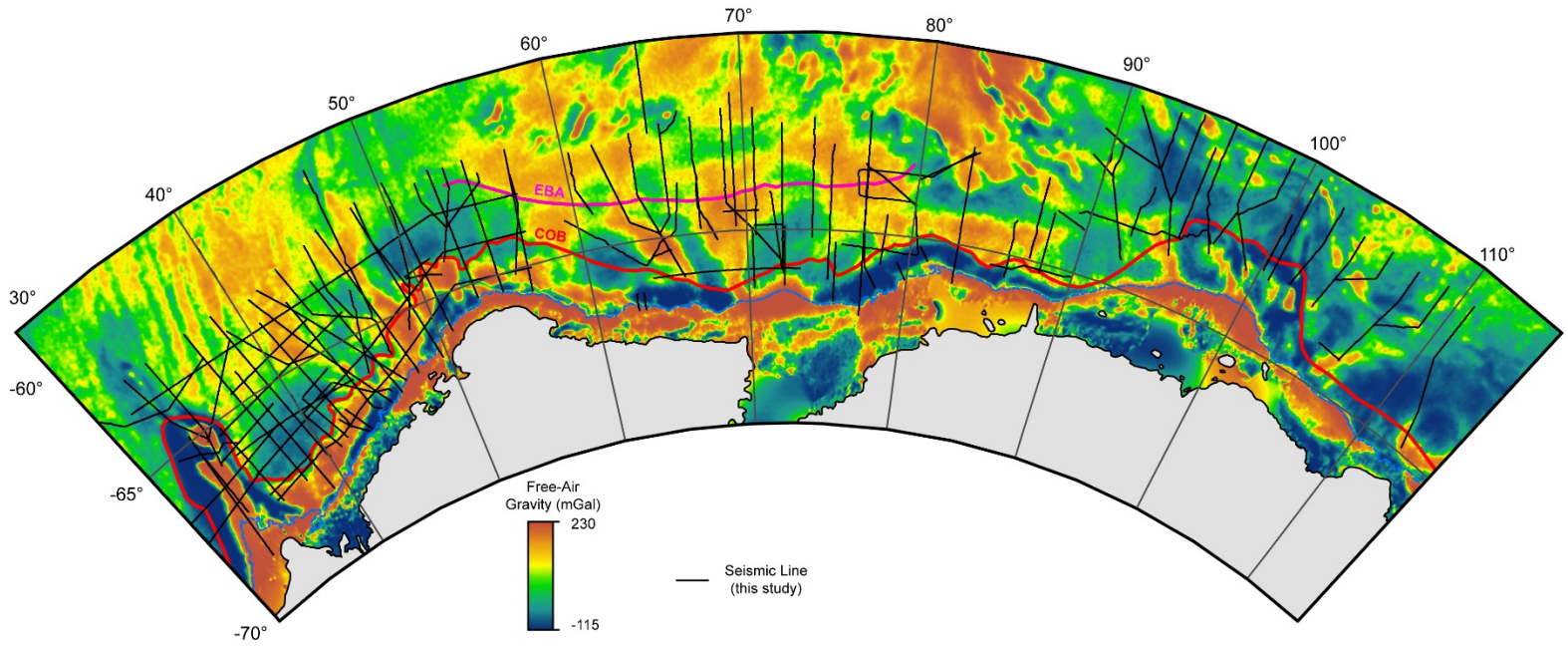

Figure 3.3 Free-air satellite gravity data and reflection seismic profiles

interpolating between clear basement reflections. If the basement was not well imaged over an extended length, no interpretation was made and the seismic line was excluded from this work. On a limited number of lines, reflections from the Mohorovičić discontinuity (moho), were visible and interpreted as a top of mantle horizon. These moho interpretations were limited in number and generally confined to the seaward portions of seismic lines in domains of smooth, well-structured, ocean crust.

3.3.2 Synthetic Velocity Model and Time to Depth Conversion

To place our seismic interpretations in an intuitive context for basin wide interpretations, a time to depth conversion was performed on all lines. Since no shot data was available to constrain a velocity model, a simple 1D formula, based on estimates of p-wave velocity, was used to construct a synthetic velocity model. For our velocity formulation, we utilize an assumed constant velocity for water (1500 m/s) and basement (6500 m/s). We also utilize a linearly increasing velocity for sediment packages (1825 + 500*s m/s). In this formulation, sediment seismic velocity starts at 1825 m/s and linearly increases at a rate of 500 m/s for every 1 second of two-way-travel time thickness. Using this velocity formulation and out interpreted water bottom and top of basement horizons, we construct a velocity model and perform a time to depth conversion. A spline fitting algorithm is used to interpolate our depth converted horizons between seismic lines and generate basin-wide surface grids for depth to water bottom (Fig. 3.4), top of basement (Fig. 3.5), and sediment thickness (Fig. 3.6). Since the velocity formulation used for the time to depth conversion, is a rough estimate and potential source of error, results from this conversion are be compared to depth grids from geophysical studies where seismic velocities were more constrained. In one of the most complex regions of our study, a

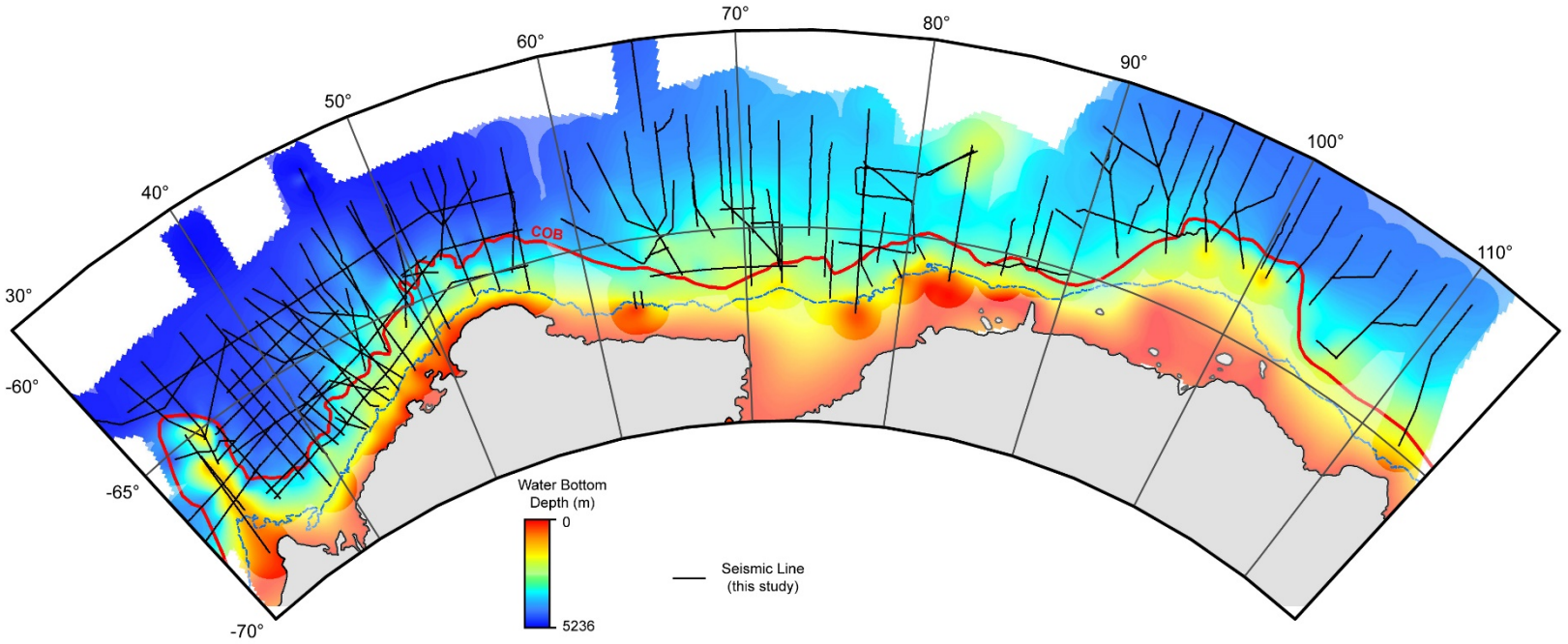

Figure 3.4 Depth to water bottom

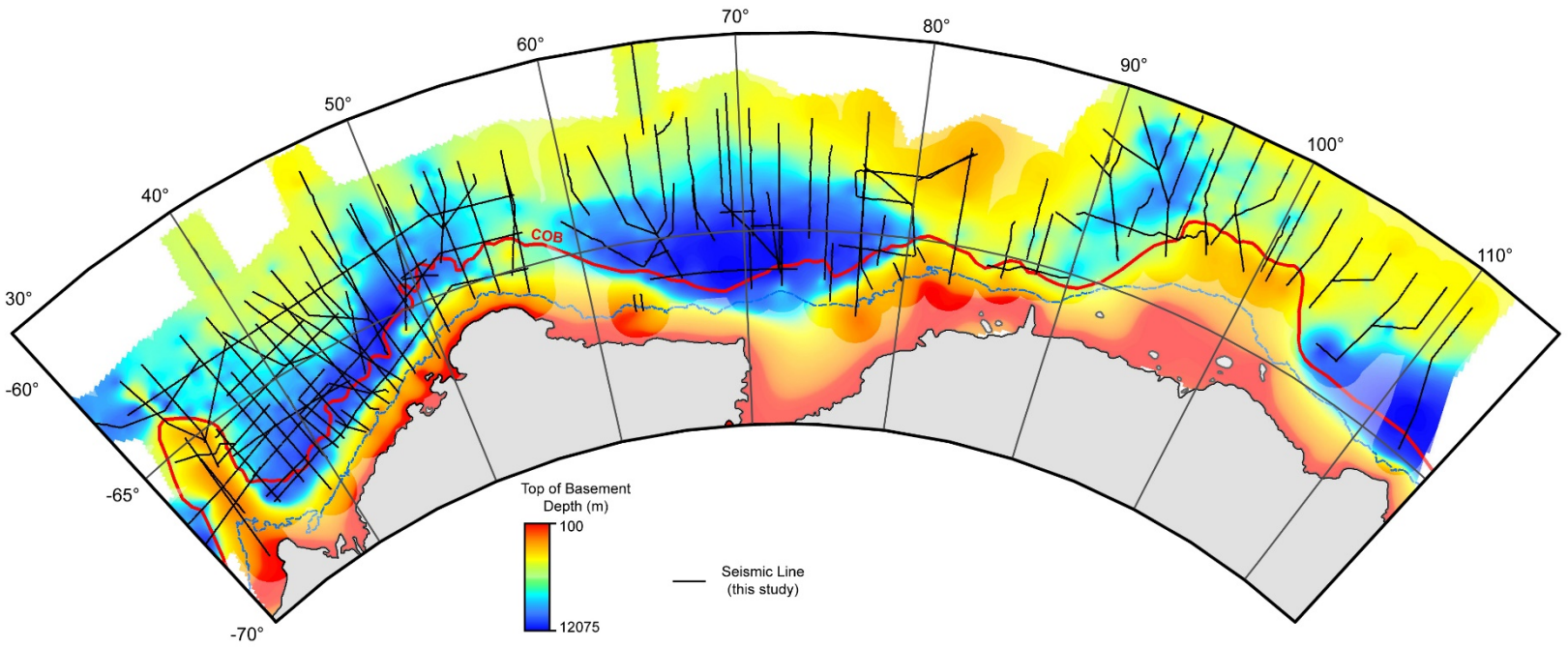

Figure 3.5 Depth to top of basement

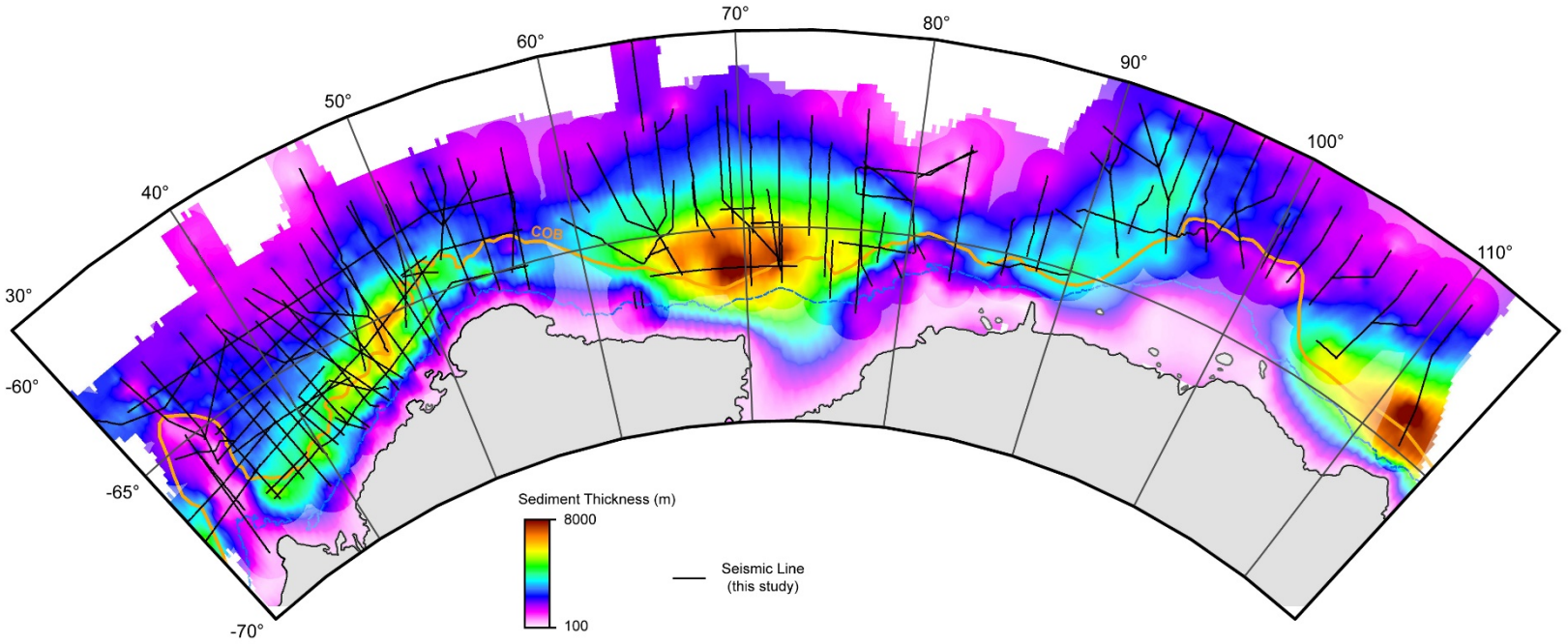

Figure 3.6 Sediment thickness

comparison of the predicted depths to top of basement from our conversion against those provided in Leitchenkov et al. (2014) show general agreement. While it is likely that an erroneous assignment of velocity has led us to over/underestimate package thicknesses for portions of the basin, we believe the depths and thicknesses estimated for the majority of the basin are approximate enough to be useful for isostatic analysis and potential field modeling.

3.3.3 Isostatic Moho and Crustal Thickness

Following the time to depth conversion, we assume local isostatic equilibrium and estimate crustal thickness/depth to moho. This isostatic calculation is done by assigning a depth of isostatic equilibrium at 31.2 km and density values for water, sediment, crust, and mantle of 1.03 g/cm3, 2.4 g/cm3, 2.8 g/cm3, and 3.3 g/cm3, respectively (G. Karner, personal communication, 2016). Along each seismic line we use our depth-converted water bottom and top of basement horizons, in conjunction with the above input variables, to estimate the crustal thickness necessary to be in isostatic equilibrium (Tc; Equation 1).

$$T_{crust} = 31.2 - T_{water}\left(\frac{(3.3 - 1.03)}{(3.3 - 2.8)}\right) - T_{sediment}\left(\frac{(3.3 - 2.4)}{(3.3 - 2.8)}\right)$$

Calculated values of crustal thickness (Fig. 3.7) are approximate and are sensitive to our assigned input variables for equilibrium depth and density. However, across the basin, the relative crustal thickness is insensitive to these inputs. This makes this process particularly useful for highlighting the relative thinning or thickening profiles of the basement within the basin. Comparison of calculated isostatic moho depths against seismically imaged and sonobuoy returned moho reflections, demonstrate an acceptable

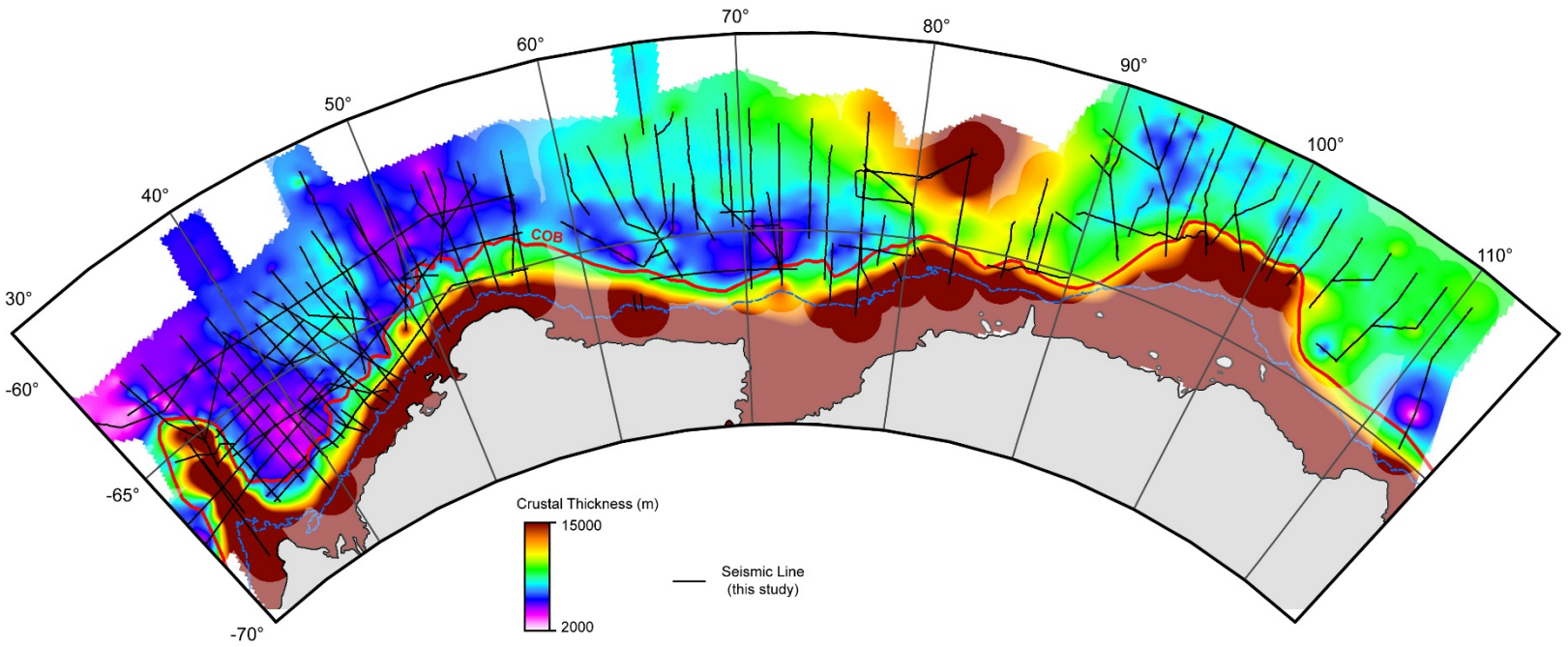

Figure 3.7 Crustal thickness

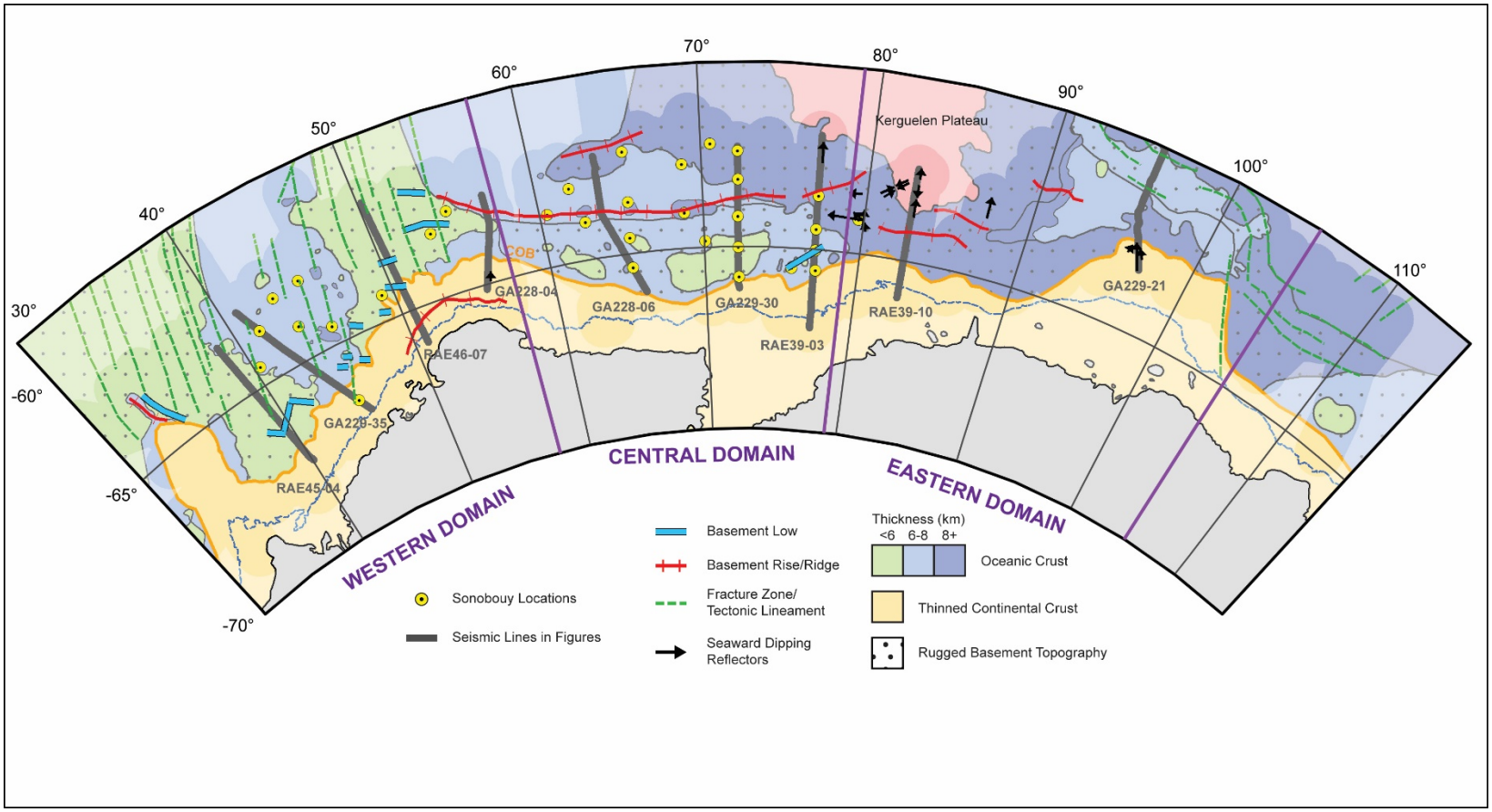

Figure 3.8 Interpreted basement morphology

The Enderby Basin can be generally divided into three domains of varying morphology

level of agreement (Fig. 3.9-3.16). So while certainly a rough estimate, values of crustal thickness are judged to be generally accurate, and can be used to help interpret the varying basin domains.

3.3.4 Regional Basement Interpretations

We utilize our regional collection of 2D seismic data, the Antarctic Digital Magnetic Anomaly Project marine magnetic compilation (Fig. 3.2; Golynsky et al., 2013), and satellite gravity data (Fig. 3.3; Sandwell et al., 2014), to identify important regional basement domains and structures preserved within the Enderby Basin (Fig. 3.8). Basin domains are divided into: predominantly continental crust, thin ocean crust (< 6 km), thick ocean crust (> 8 km), normal ocean crust (6-8 km), and the Kerguelen Plateau. Basin domains are qualitatively assessed for roughness based on the flatness of the top of basement reflector. A number of localized basement structures are identified that may be useful for understanding basin evolution, including: the COB, linear basement rises/ridges, linear basement lows, fracture zones, and volcanic seaward-dipping packages (SDRs; Fig. 3.8).

In this study, the COB demarcates the boundary between the inboard domain of predominantly continental crust, and the outboard domain of predominantly oceanic crust. The location of the COB is interpreted on each seismic profiles at the boundary between (1) an inboard basement demonstrating a seaward thinning profile, as would be expected for rifted continental crust and (2) an outboard basement domain, less than 10 km in thickness, that demonstrates either constant thickness over a domain wider than 50 km, and/or seaward thickening. Between seismic lines, the COB is interpolated using satellite gravity or magnetic fabric. Basement lows and basement rises are interpreted from

observations from seismic profiles, and when clearly linked to satellite gravity or magnetic features, are further interpolated spatially. SDR packages are interpreted based on the observation of thick, sub-basement, concave downward, dipping reflector series. Fracture zones are primarily interpreted from satellite gravity data (Fig. 3.3; Sandwell et al., 2014) but are often identifiable on seismic profiles as local zones of sediment and basement deformation.

3.3.5 Potential Field Modeling

To help assess the nature of gravity and magnetic anomalies, potential field modeling was performed on nine seismic lines using Geosoft's Oasis Montaj package. Seismic lines were chosen based on clear imaging of basement structure and spatial distribution to give coverage of the various basement domains (Fig. 3.8-3.27). Since shipborne gravity and magnetic data was unavailable, anomaly data from the publically available free-air satellite gravity (Sandwell et al., 2014) and Antarctic Digital Magnetic Anomaly Project compilation (Golynsky et al., 2013) were used for this modeling. These data were extracted along the seismic profiles. On all lines packages of water, sediment, crust, and mantle were initially assigned densities corresponding to those used in the isostatic analysis. Gravity anomalies were then matched through the variation of crustal density. While this density change might affect local isostasy, we do not alter our estimated crustal thickness or depth to isostatic moho values. To assign remnant magnetic anomaly orientations, seismic lines were placed in a plate tectonic framework based on the rotation poles provided in Davis et al. (2016), and an absolute framework based on Torsvik et al. (2012). Within this reconstruction framework, we assume remnant magnetization is locked in when the coastline of East India moves over the midpoint of the seismic line. At this

age, the seismic line midpoint paleolatitude is used to determine remnant inclination potentially preserved within the crust. Calculated remnant inclination values are between -67° and -73°. For magnetic field modeling, we vary susceptibility values for the lower crust between (0 and 0.9 SI) and for the basaltic upper oceanic crust between (0 and 0.18 SI). Remnant magnetization is modeled in the upper oceanic crust and is allowed to vary between 0 and 5 A/m. We find that no reversed remnant magnetization is needed to match the observed magnetic anomaly data.

3.4 RESULTS

3.4.1 Regional Overview

Surface grids for the depth to water bottom (Fig. 3.4), depth to top of basement (Fig. 3.5), sediment thickness (Fig. 3.6), and crustal thickness (Fig. 3.7), help summarize quantitative results from seismic interpretation, time to depth conversion, and isostatic analysis. Interpretation of basin domains and basement structures (Fig. 3.8) highlight rift style variations and may help guide interpretations of basin evolution. Select seismic lines and sonobuoy velocity data are plotted (Fig. 3.9-3.27) to illustrate details of basement interpretations and highlight differences with previous works. Based on regional observations we divide the Enderby Basin into three generalized domains: an Eastern Domain with significant volcanism and thick ocean crust; a Central Domain characterized by two regions of varying ocean crust morphology delineated by the EBA; and a Western Domain of primarily varying thickness with basement lows and fracture zones. To the east of our Eastern Domain is younger basement formed from the rifting of Australia and East Antarctica, which is beyond the scope of this work. The COB, interpreted as part of this project, occurs between 50-200 km from the 1000 m isobaths, and between 150-300 km

outboard of the present-day coastline. At the Bruce Rise and Gunnerus Ridge, these distance are higher due to anomalously thick continental crust distributed further outboard into the basin (Stagg et al., 2006; Leitchenkov et al., 2008).

3.4.2 Eastern Domain

The Eastern Domain preserves the oldest existing oceanic crust formed from the breakup of India and East Antarctica (Davis et al., 2016). Based on our geophysical observations, the Eastern Domain appears to be characterized by features related to abundant volcanism. These features include SDRs packages, both inboard and outboard of the COB, wide domains of thick oceanic crust, basement ridges possibly related to plume induced ridge jumps, and the volcanically thickened crust of the Kerguelen Plateau. Volcanic intrusion (Fig. 3.9) of the Bruce Rise (Leitchenkov et al., 2008; Stagg et al., 2006) suggest that, within this sector, volcanism arose early during continental breakup. Within the Bruce Rise, high amplitude magnetic anomalies are coincident with observed SDR packages (Fig. 3.10). These magnetic anomalies continue along a large portion of the continental shelf, potentially indicating an extensive domain of volcanic intrusion (Fig. 3.2; Golynsky et al., 2013). To the south of the Kerguelen Plateau, the thickness of oceanic crust (11 km) at the COB is the highest of the entire Enderby Basin (Fig. 3.11). The spatial distribution of this anomalously thick oceanic crust, suggests an influence by the Kerguelen Hotspot. Estimates of full spreading rates for the early (135-125 Ma) rifting in the Eastern Domain range between 33-50 mm/yr. (Davis et al., 2016), which although slow in classification, are the highest of all of the Enderby Basin domains. Within the Eastern Domain, we observe the thinnest sedimentary packages of the entire Enderby Basin, with maximum thicknesses of ~4 km. In the Eastern Domain, our preferred COB closely mimics

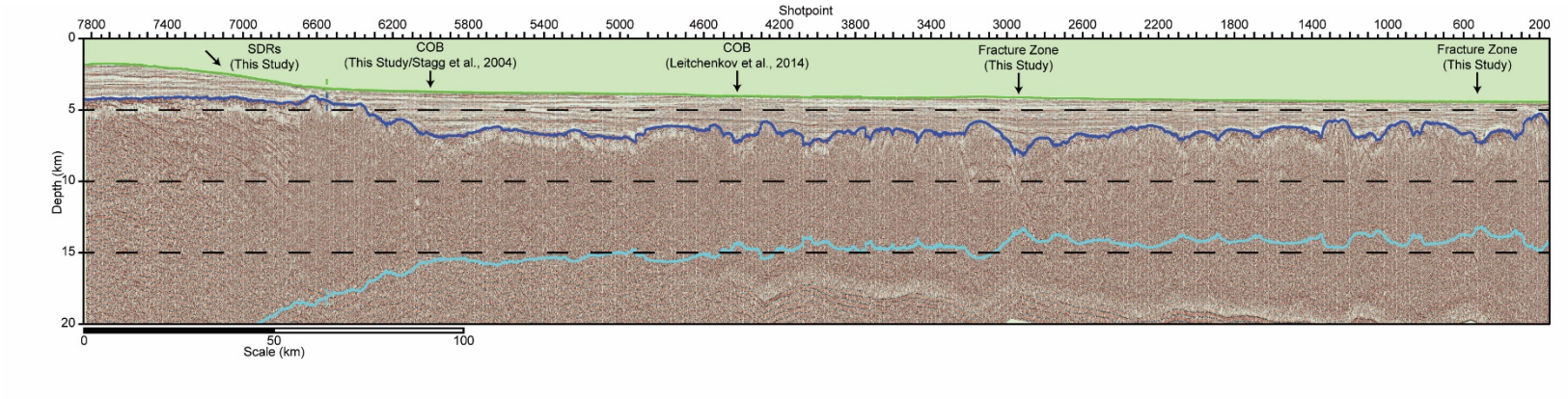

Figure 3.9 Reflection seismic profile GA229-21

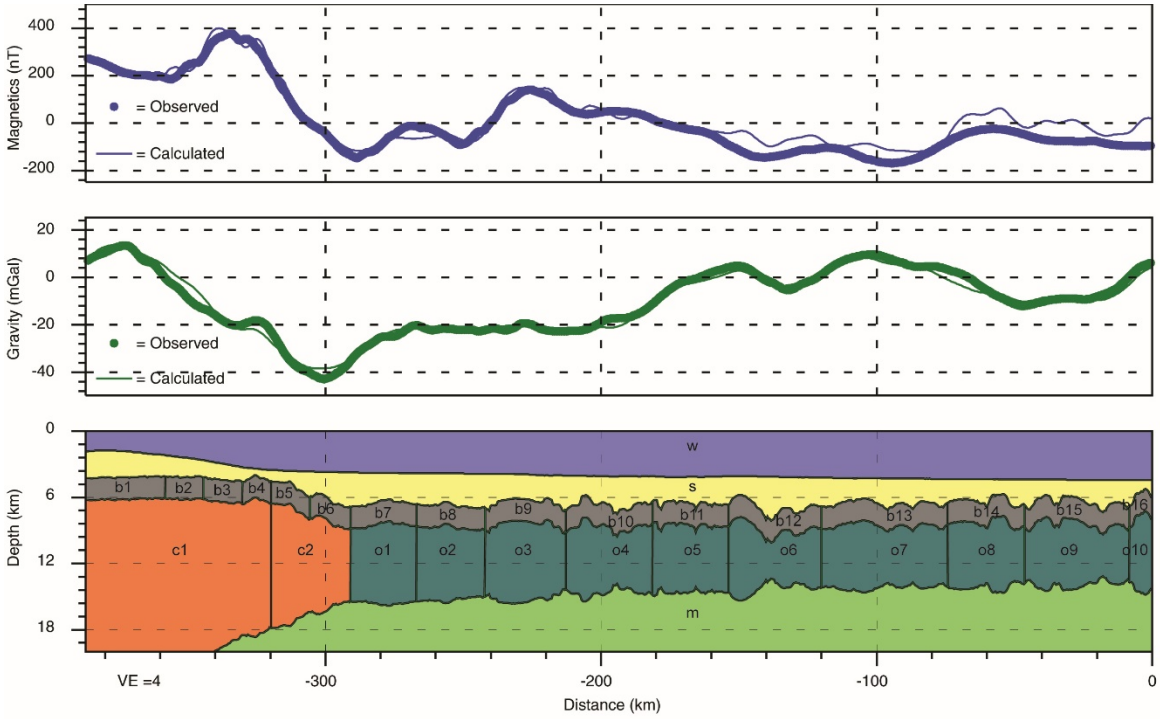

Block	Density	Suceptibility (SI)	Remnance (A/m)	Inclination (°)
w	1.03	0	0	
s	2.4	0	0	
m	3.3	0	0	
b1	2.8	0.08	2	-68.5
b2	2.75	0.11	2	-68.5
b3	2.7	0.17	2	-68.5
b4	2.85	0.13	2	-68.5
b5	2.75	0.07	2	-68.5
b6	2.7	0.05	2	-68.5
b7	2.8	0.05	2	-68.5
b8	2.775	0.06	2	-68.5
b9	2.75	0.11	2	-68.5
b10	2.75	0.05	2	-68.5
b11	2.85	0.07	2	-68.5
b12	2.8	0.04	2	-68.5
b13	2.875	0.01	2	-68.5
b14	2.8	0.03	2	-68.5
b15	2.8	0.04	2	-68.5
b16	2.85	0.04	2	-68.5
c1	2.8	0.05	0	
c2	2.75	0.05	0	
o1	2.8	0.04	0	
o2	2.8	0.04	0	
o3	2.775	0.04	0	
o4	2.775	0.05	0	
o5	2.85	0.01	0	
o6	2.85	0.01	0	
o7	2.875	0.01	0	
o8	2.8	0.03	0	
o9	2.8	0.02	0	
o10	2.85	0.02	0	

Figure 3.10 Potential field model for GA229-21

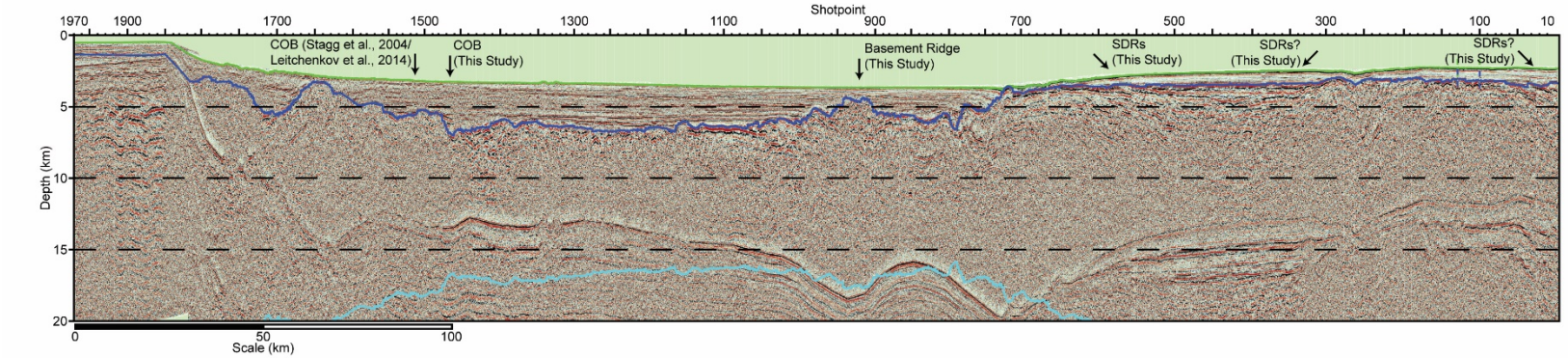

Figure 3.11 Reflection seismic profile RAE39-10

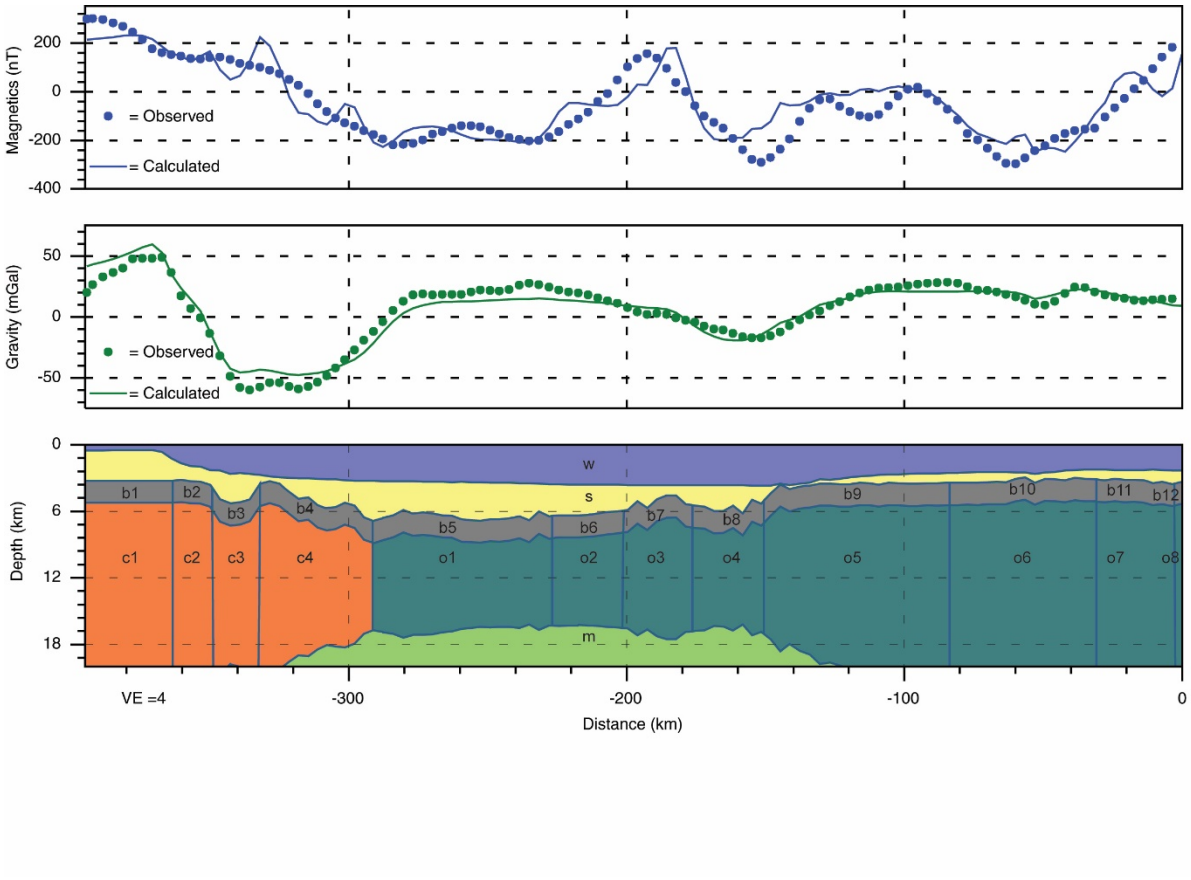

Block	Density	Suceptibility (SI)	Remnance (A/m)	Inclination (°)
w	1.03	0	0	
s	2.4	0	0	
m	3.3	0	0	
b1	2.675	0.12	2	-69.43
b2	2.875	0.14	2	-69.43
b3	2.675	0.18	2	-69.43
b4	2.525	0.1	2	-69.43
b5	2.875	0.07	2	-69.43
b6	2.875	0.15	2	-69.43
b7	2.85	0.16	2	-69.43
b8	2.775	0.09	2	-69.43
b9	2.75	0.06	2	-69.43
b10	2.75	0.08	2	-69.43
b11	2.8	0.04	2	-69.43
b12	2.8	0.1	2	-69.43
c1	2.8	0.07	0	
c2	2.775	0.05	0	
c3	2.85	0.07	0	
c4	2.75	0.05	0	
o1	2.875	0.05	0	
o2	2.875	0.05	0	
o3	2.825	0.05	0	
o4	2.775	0.05	0	
o5	2.825	0.05	0	
o6	2.825	0.03	0	
o7	2.8	0.07	0	
o8	2.8	0.07	0	

Figure 3.12 Potential field model for RAE39-10

that proposed by Australian researchers (Stagg et al., 2004; Stagg et al., 2005; Stagg et al., 2006; O'brien & Stagg, 2007), with minor differences (~50 km) proximal to the Bruce Rise in the Davis Sea. Additionally, our Eastern Domain COB generally agrees with that proposed by Russian researchers (Leitchenkov et al., 2008; Leitchenkov et al., 2014) in the Princess Elizabeth Trough region. However, in the Davis Sea and near the Bruce Rise we prefer a COB located up to 200 km landward of that proposed from their works. A series of tectonic lineaments mark the eastward limit of India-East Antarctic rifting, while a series of basement rises and SDR packages (Fig. 3.8 & Fig. 3.11) mark the transition to the thinner crust of the Central Domain.

3.4.3 Central Domain

The Central Domain is the most enigmatic and contentious of all the Enderby Basin domains. In our preferred interpretation, the Central Domain is characterized by an inboard region of rough, locally thin (< 6 km), proto-ocean crust and an outboard region of smooth, well-structured, normal ocean crust. Within this interpretation, the EBA delimits the boundary between these two differing oceanic regions. It is important emphasize that while the EBA has often been interpreted to demarcate the COB (e.g., Stagg et al., 2004; Leitchenkov et al., 2014), we are proposing an alternative interpretation and instead suggest that the EBA marks a change in ocean crust character. We propose that the COB is located up to 275 km inboard of the EBA (Fig. 3.8). This interpretation is based on the observed the isostatic limit of seaward crustal thinning, and the outboard domain, 150-275 km in width, of crust that is between 4.5 and 8 km in thickness (Fig. 3.7). It is difficult to reconcile a basement domain of this width and crustal thickness, that is devoid any regional crustal

thinning, with a plausible model of continental extension. However, these observations of crustal morphology are consistent with formation by seafloor spreading processes.

A thick sediment package, up to 9 km in thickness, sits above the basement within the region inboard of the EBA, making the imaging of internal crustal structure difficult (Fig. 3.6). On seismic reflection lines, this basement appears to be rugged, with local offsets up to 0.5 km (Fig. 3.13-3.18), and is often imaged as a series of high amplitude diffractions. Crustal thickness is locally variable within this internal region, with minimums thicknesses of ~4.5 km and maximums of up to 8 km. Rugged and faulted crust, of these variable thicknesses, is similar in morphology to oceanic crust formed at ultraslow/slow mid-ocean ridges (Dick et al., 2003; Niu et al., 2015). Spreading rates within the Central Domain are variable, with minimum values of ~15 mm/yr. and maximum values of 33 mm/yr. (Davis et al., 2016), consistent with an ultraslow/slow seafloor spreading system.

Both Australian and Russian works have contended that the basement domain inboard of the EBA exhibits seismic velocities indicative of a continental crust (e.g., Stagg et al., 2004; Leitchenkov et al., 2014). To help provide context for this contention, we have plotted observed sonobuoy velocity and depth information provided in Stagg et al. (2004) into the proximal 2D seismic profiles at the closest shot point to the sonobuoy position (Fig. 3.13-3.18). In the Central Domain, we observe that, basement inboard of the EBA is deeper than the basement outboard of the EBA. This makes the absolute depth vs. seismic velocity information conveyed in the sonobuoy table and figures of Stagg et al. (2004) ineffective for describing trends in crustal velocity. As such, we have plotted the sonobuoy velocity data, for the Central Domain from Stagg et al. (2004), at depths relative the top of basement observed on seismic reflection data (Fig. 3.19).

To compare the seismic velocity properties of the inboard and outboard regions, we color-code the velocity data based on the inboard/outboard position of the sonobuoy

relative to the EBA (Fig. 3.19). To help distinguish a potential ocean or continental affinity, for these regions, we have plotted observations of seismic velocity from similarly aged Atlantic Ocean lithosphere (White et al., 1992) and average seismic velocities from continental crust (Christensen & Mooney, 1995). Sonobuoy velocities, from the inboard and outboard regions, demonstrate similar values and trends in crustal seismic velocity. The only observable difference between inboard and outboard crustal velocities, occurs at 1-3 km depth from top of basement. At these depths, inboard crustal velocities are slightly lower (5.5-6.5 km/s) than that outboard crustal velocities (6-7 km/s). However, the inboard velocities from this depth do not unequivocally demonstrate velocities typical of average continental crust, nor do these velocities disprove a potential oceanic affinity. Overall the observed trends in crustal seismic velocity, from both the inboard and outboard regions, increase in a manner that resembles similarly aged oceanic crust (White et al., 1992). Coupled with our isostatically observed limit of crustal thinning, we believe that our preferred interpretation of a more inboard COB is plausible. This COB results in a domain of thinned continental crust that is 150-275 km from the coastline, while acceptance of an outboard COB at the EBA (e.g., Stagg et al., 2004; Leitchenkov et al., 2014), would require the thinned continental crust domain to be 450-500 km in width.

Given seismic and isostatic observations, we propose that the rugged, unthinned, 4.5-8 km crust, preserved between the COB and EBA, represents a region of proto-oceanic crust formed by seafloor spreading processes similar to that at ultraslow/slow mid-ocean ridges. Given our interpretation of inboard crustal structure, we suggest that rather than the COB, the EBA represent a change in magmatic production and ocean crust morphology. A change in magmatic production is suggested by a local step-up in basement with locally thick (> 8 km) crust at the EBA, and the outboard observation of 6-8 km, well-structured,

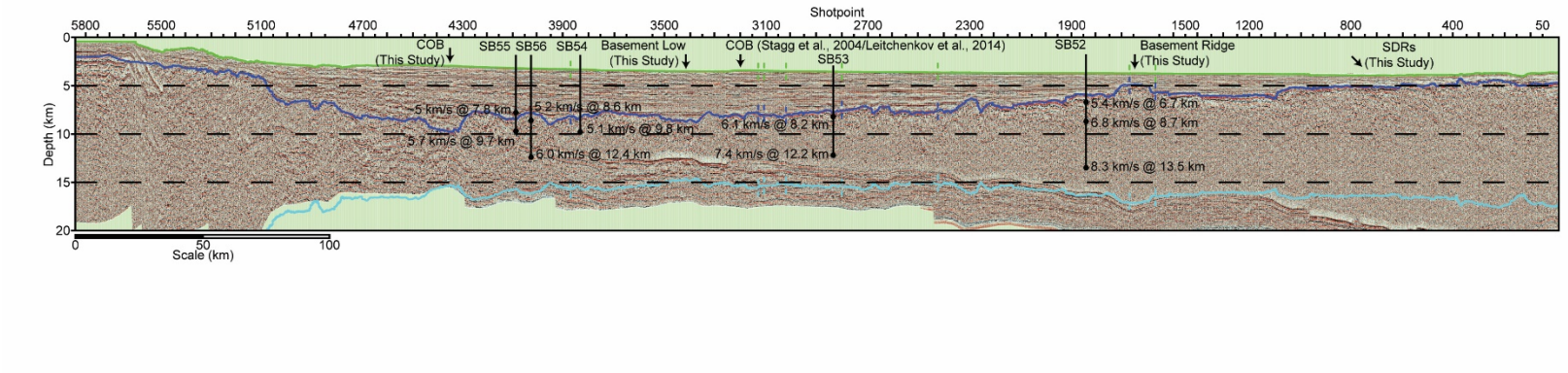

Figure 3.13 Reflection seismic profile RAE39-03

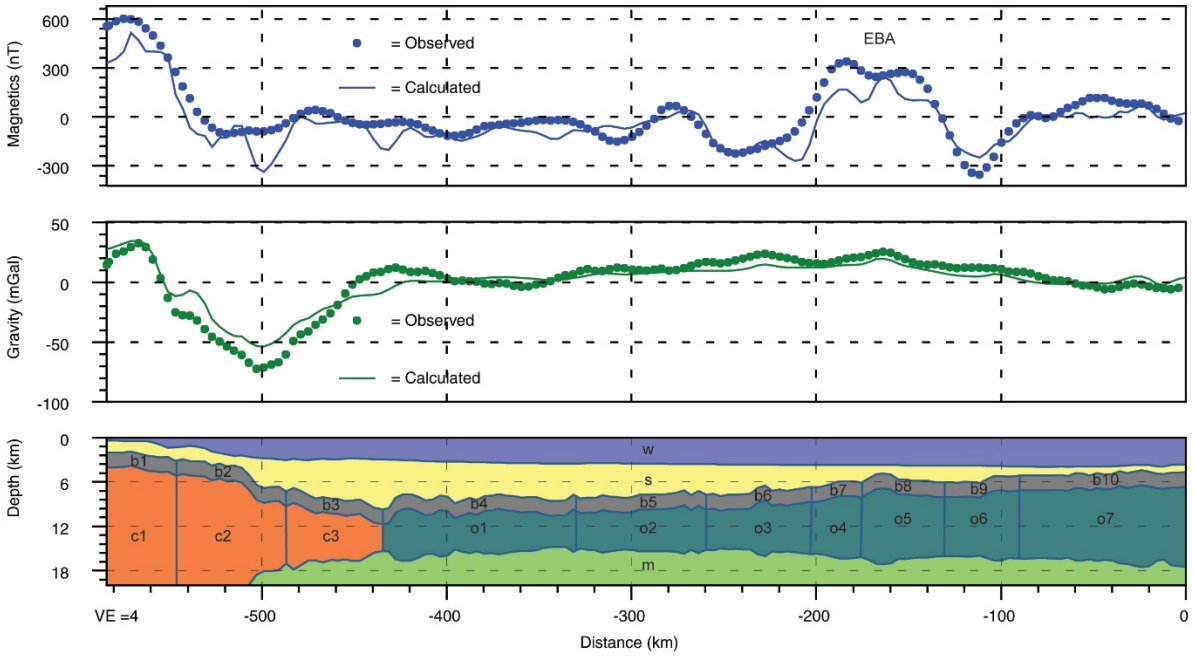

Block	Density	Suceptibility (SI)	Remnance (A/m)	Inclination (°)
w	1.03	0	0	
s	2.4	0	0	
m	3.3	0	0	
b1	2.75	0.15	2	-69.96
b2	2.675	0.18	2	-69.96
b3	2.875	0.18	2	-69.96
b4	2.825	0.18	2	-69.96
b5	2.875	0.11	2	-69.96
b6	2.875	0.01	2	-69.96
b7	2.875	0.18	2	-69.96
b8	2.875	0.15	2	-69.96
b9	2.875	0.13	2	-69.96
b10	2.8	0.1	2	-69.96
c1	2.8	0.09	0	
c2	2.75	0.04	0	
c3	2.775	0.09	0	
o1	2.85	0.05	0	
o2	2.825	0.09	0	
o3	2.85	0.09	0	
o4	2.825	0.09	0	
o5	2.825	0.09	0	
o6	2.8	0.05	0	
o7	2.8	0.09	0	

Figure 3.14 Potential field model for RAE39-03

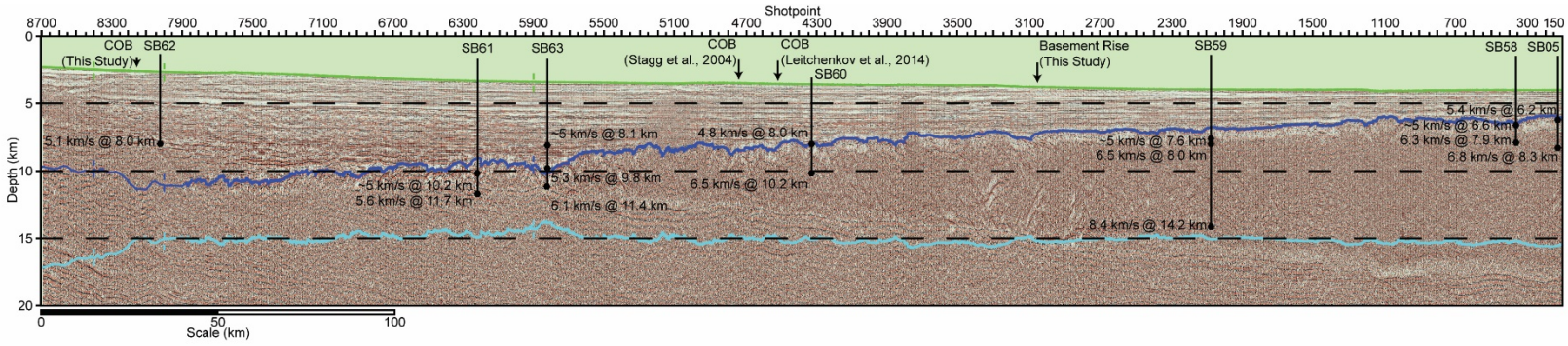

Figure 3.15 Reflection seismic profile GA229-30

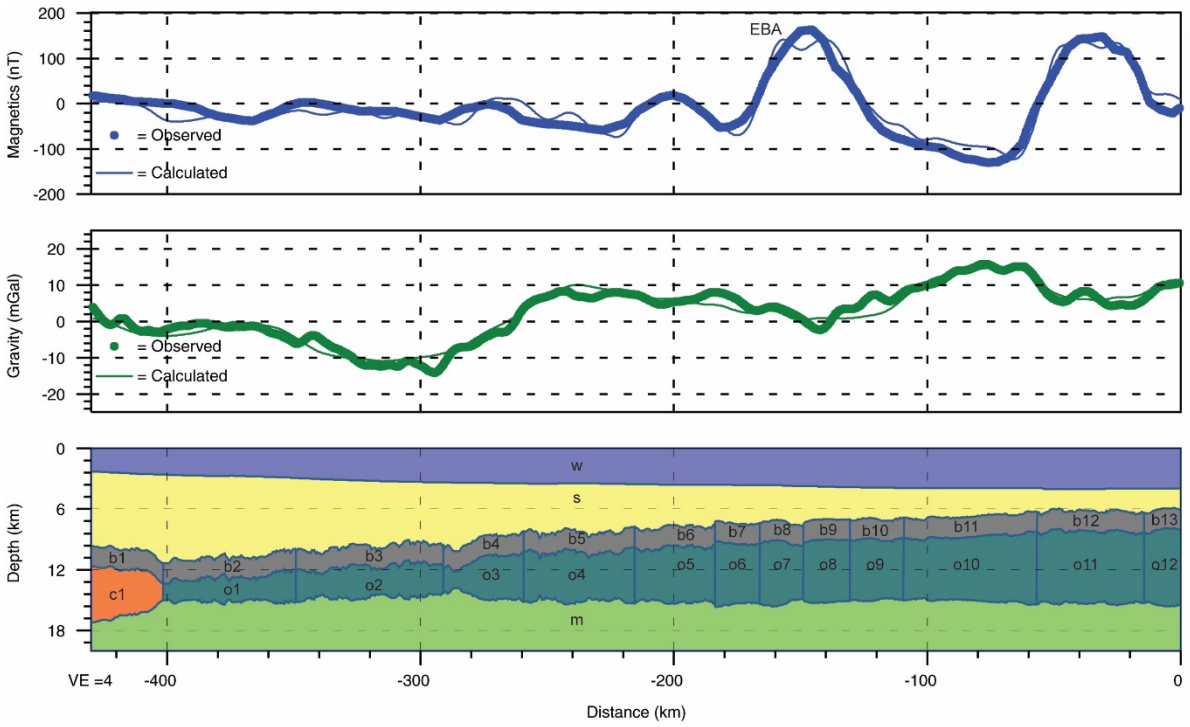

Block	Density	Suceptibility(SI)	Remnance(A/m)	Inclination(°)
w	1.03	0	0	
s	2.4	0	0	
m	3.3	0	0	
b1	2.75	0.1	2	-70.06
b2	2.8	0.11	2	-70.06
b3	2.725	0.13	2	-70.06
b4	2.75	0.15	2	-70.06
b5	2.825	0.08	2	-70.06
b6	2.8	0.18	2	-70.06
b7	2.775	0.09	2	-70.06
b8	2.775	0.08	2	-70.06
b9	2.8	0.09	2	-70.06
b10	2.775	0.09	2	-70.06
b11	2.85	0.07	2	-70.06
b12	2.75	0.09	2	-70.06
b13	2.825	0.1	2	-70.06
c1	2.775	0.02	0	
o1	2.8	0.02	0	
o2	2.75	0.01	0	
o3	2.8	0.01	0	
o4	2.85	0.04	0	
o5	2.825	0.01	0	
o6	2.8	0.04	0	
o7	2.8	0.09	0	
o8	2.8	0.08	0	
o9	2.8	0.04	0	
o10	2.85	0.04	0	
o11	2.85	0.08	0	
o12	2.825	0.05	0	

Figure 3.16 Potential field model for GA229-30

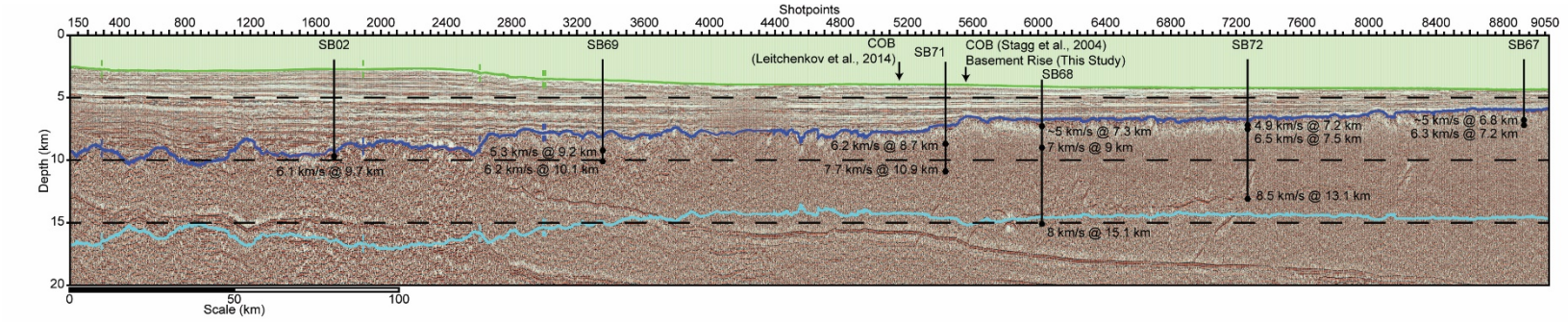

Figure 3.17 Reflection seismic profile GA228-06

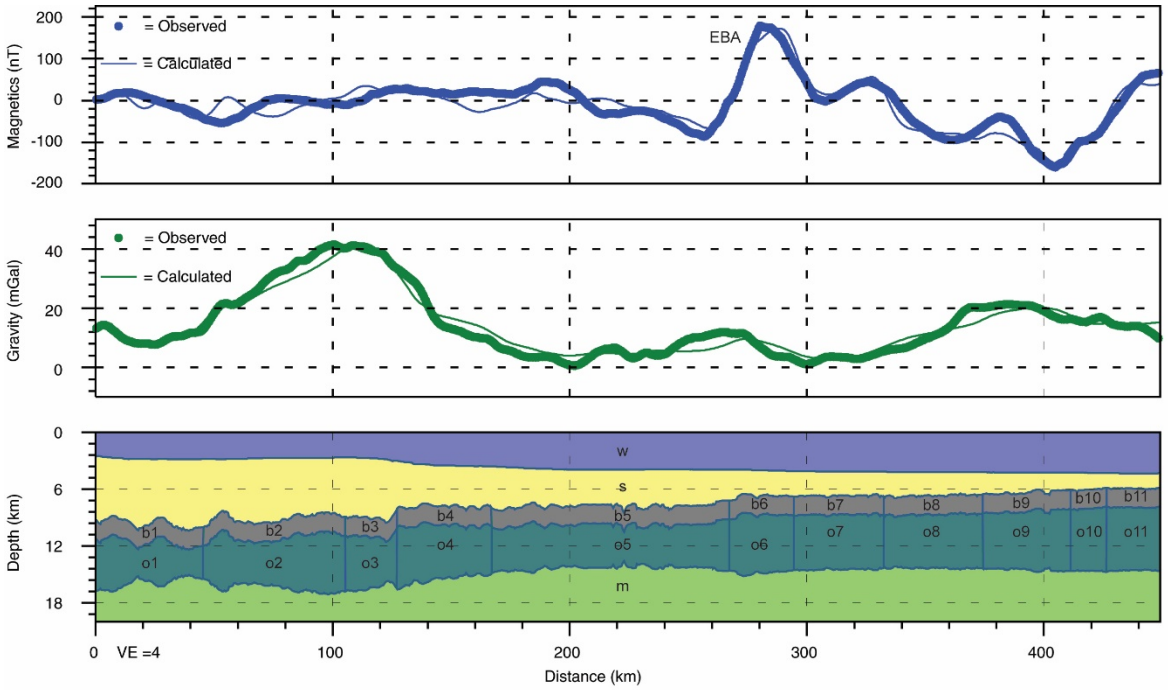

Block	Density	Suceptibility (SI)	Remnance (A/m)	Inclination (°)
w	1.03	0	0	
s	2.4	0	0	
m	3.3	0	0	
b1	2.75	0.1	2	-70.09
b2	2.85	0.06	2	-70.09
b3	2.875	0.1	2	-70.09
b4	2.775	0.06	2	-70.09
b5	2.7	0.09	2	-70.09
b6	2.775	0.11	2	-70.09
b7	2.7	0.06	2	-70.09
b8	2.775	0.03	2	-70.09
b9	2.825	0.06	2	-70.09
b10	2.75	0.1	2	-70.09
b11	2.8	0.1	2	-70.09
o1	2.775	0.02	0	
o2	2.85	0.04	0	
o3	2.875	0.04	0	
o4	2.825	0.04	0	
o5	2.8	0.04	0	
o6	2.775	0.06	0	
o7	2.775	0.04	0	
o8	2.8	0.02	0	
o9	2.825	0.01	0	
o10	2.8	0.02	0	
o11	2.8	0.05	0	

Figure 3.18 Potential field model for GA228-06

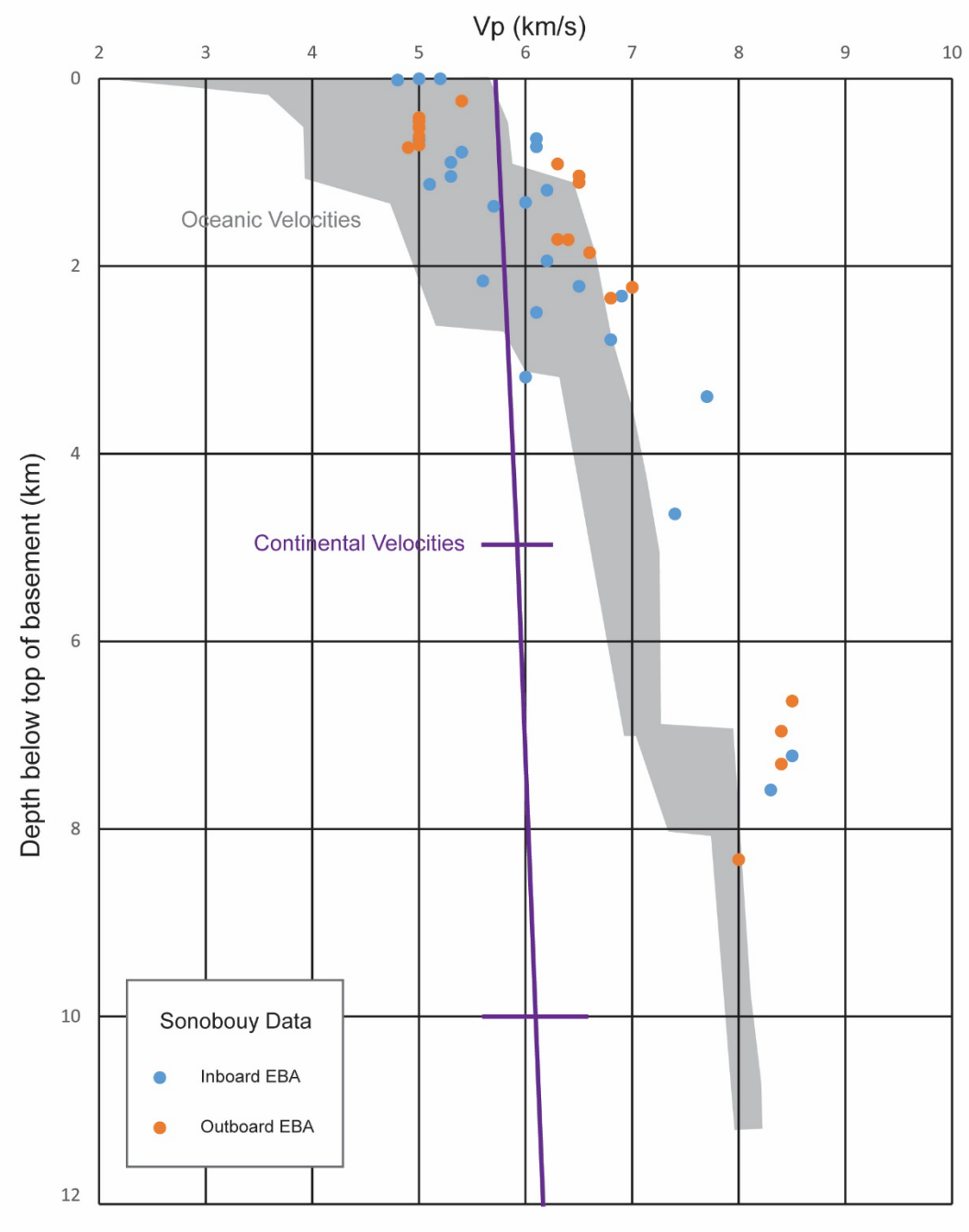

Figure 3.19 Sonobuoy velocities with crustal depth

Sonobuoy data is color-coded based on position relative to the EBA. Average seismic velocities from oceanic lithosphere (grey) and continental crust (purple) are plotted for comparison

ocean crust (Fig. 3.8 & Fig. 3.13-3.18). The magnetic anomaly produced at this boundary is a function of a change in basement elevation and a concurrent increase in crustal magnetic susceptibility (Fig. 3.14, 3.16, & 3.18).

3.4.3.1 Potential causes of crustal variation observed at the EBA

We offer three potential, non-exclusive, explanations for the change in ocean crust morphology observed in the Central Domain at the EBA. Both explanations are related to observed variations in ocean crust morphology (Dick et al., 2003; Carbotte & Scheirer, 2004). Mid-ocean ridges with axial depressions, rugged basement relief, and thin oceanic crust (< 6 km), are generally observed within ultraslow/slow spreading systems (Dick et al., 2003), and correspond in morphology to predictions from analytical models of passive mantle flow and low degrees of melting (Phipps Morgan et al., 1987). Ridges with axial rises and normal thickness ocean crust, are observed at spreading systems of intermediate/fast extensions rates (Carbotte and Scheirer, 2004), and correspond to analytical models of buoyant mantle flow and melting (Sotin & Parmentier, 1989).

Our first proposed explanation is that, initially after continental breakup, melt production/retention was low, and unable to induce the buoyant upwelling and melting rates necessary to form normal, full-thickness, oceanic crust (Bown & White, 1994, 1995). In this explanation, the progressive upwelling of the asthenosphere eventually led to an increase in melt production. This increase in melt production drove stable, buoyant mantle flow, and the formation of normal oceanic crust. This explanation is supported by the observed gradual thickening of the oceanic crust out to the EBA (Fig. 3.7). An alternative explanation, is that within the Enderby Basin, the progressive increase in spreading rate led to an increase in melt production and corresponding change in ocean crust morphology.

This is similar to the globally observed spreading rate dependence of ocean crust morphology (e.g., Carbotte and Scheirer, 2004). An increase in spreading rate is suggested by the plate model of Davis et al. (2016), however the later spreading rates in the basin are difficult to constrain due to temporal proximity to the Cretaceous Normal Superchron (120.6 - 83.0 Ma; Gee and Kent, 2007). Our last potential explanation, is that a ridge jump altered the spreading ridge orientation relative to the extension direction, which led to an increase in effective spreading rate and melt production. If the spreading ridge changed from oblique to orthogonal relative to the extension direction, it would increase the effective spreading rate, which can assist in buoyant upwelling and manifest as distinct change in ocean crust morphology (Dick et al., 2003). A ridge jump is suggested by both the distinct, and linear nature of the EBA, as well as a basement ridge feature that appears to emanate from the Kerguelen Plateau (Fig. 3.8 & Fig. 3.13). However, with the geophysical data available for this work, we cannot resolve a clear extinct spreading ridge inboard of the EBA and confirm the ridge jump provenance of the observed EBA structure. We note that none of the proposed explanations are mutually exclusive. It is entirely possible that the observed crustal variations corresponds to a post-breakup increase in melt production, increase in spreading rate, and/or a coeval change in spreading ridge geometry.

3.4.4 Western Domain

Basement crust within the Western Domain is variable in thickness and is the only domain with distinct and abundant fracture zones (Fig. 3.8). The oceanic crust within the Western Domain is the youngest of the Enderby Basin and was formed at the lowest spreading rates (<15 mm/yr; Davis et al., 2016). The orientation of the coastline and COB indicate that, in this domain, continental breakup was oblique to the direction of plate

motion. Based on observed differences in crustal morphology, we subdivide the Western Domain into three regions. The Western Domain consists of an eastern region of thin crust abutting the EBA, a central region of normal thickness ocean crust, and a western region of thin crust.

At the transition between the Central and Western Domains we observe a fracture zone (Fig. 3.8) that appears to truncate the EBA. On one seismic profile, eastward of this fracture zone, we observed a western continuation of the EBA and basement rise (Fig. 3.20 & 3.21). A potential SDR package inboard of the COB on this profile may suggest a volcanic continental breakup within this portion of the Western Domain (Fig. 3.20). In the eastern portion of the Western Domain, we observe thin ocean crust (5-6 km) and a basement ridge within the continental crust corresponding to a high amplitude magnetic anomaly, which may indicate shelf volcanism (Fig. 3.22 & 3.23). Crust within this eastern region is highly rugged, with multiple basement lows inboard and around the COB (Fig. 3.8). In the central region of the Western Domain, we observe 6-8 km thick, ocean crust that is intermittently well-structured (Fig. 3.24). Fracture zones cross much of this crust and may have zones of deformation that continue into the continental crust inboard of the COB (Fig. 3.8 & 3.24). In the westernmost region of the Enderby Basin we observe a number of fracture zones and a series of basement lows that appear orthogonal when linked between seismic lines (Fig. 3.8). Outboard of these basement lows and proximal to an apparent fracture zone (Fig. 3.26), there appears to be a change in crustal morphology, where crust inboard of the fracture zone is less than 5 km in thickness, and outboard between 5-6 km in thickness (Fig. 3.7). Crustal thickness increases with proximity to Gunnerus Ridge, potential suggesting a volcanic influence near the ridge. Multiple basement lows observed in the Western Domain are oblique to the coastline. Since these lows are not orthogonal to the outboard fractures zones, the Western Domain appears to

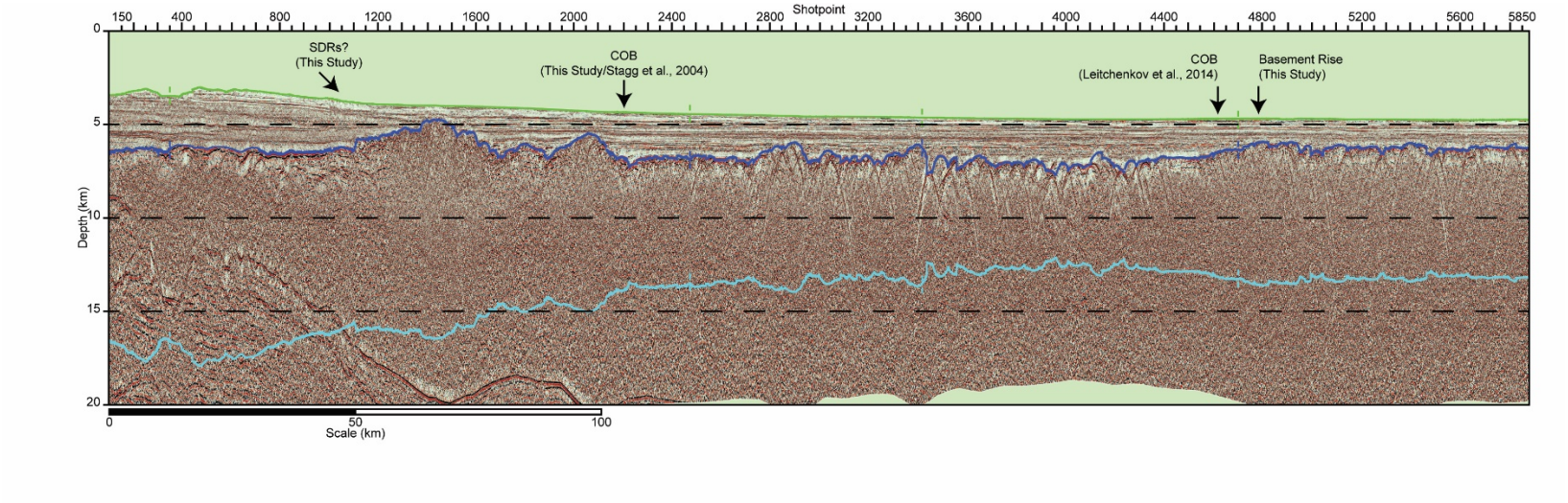

Figure 3.20 Reflection seismic profile GA228-04

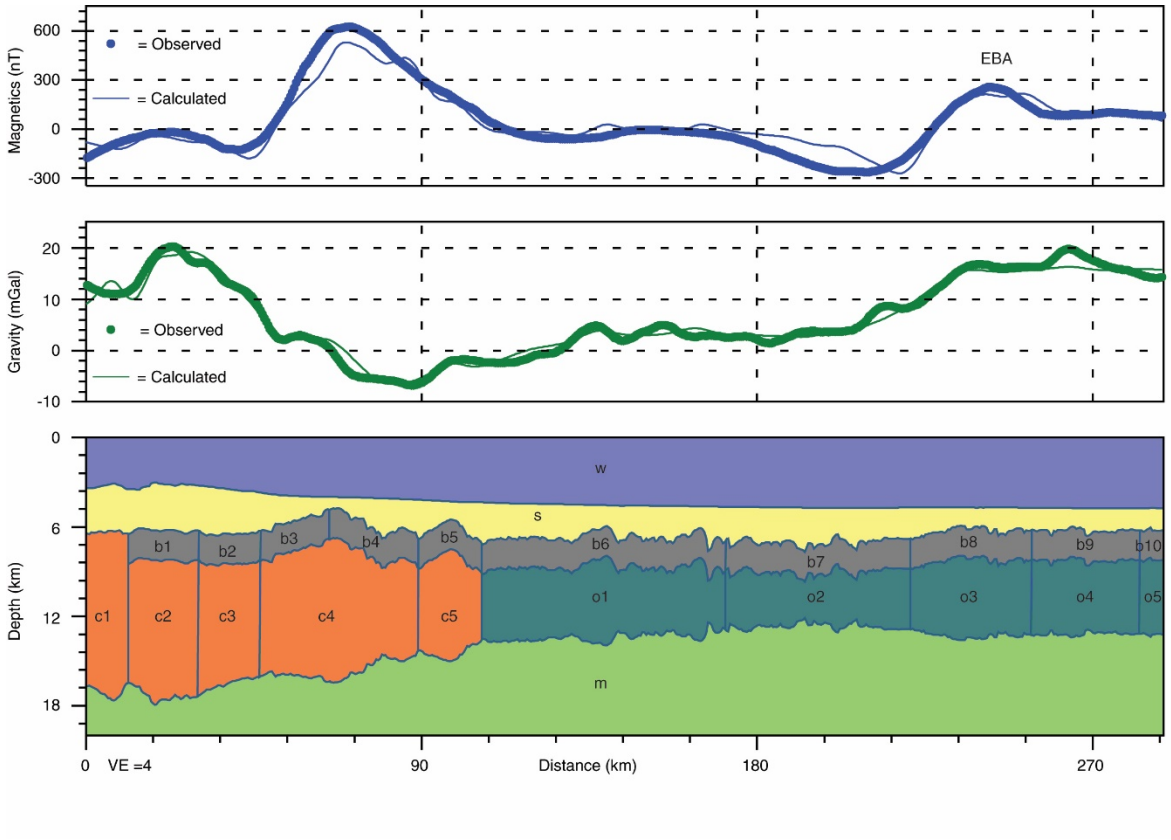

Block	Density	Suceptibility	Remnance	Inclination
w	1.03	0	0	
s	2.4	0	0	
m	3.3	0	0	
b1	2.8	0.08	1	-69.73
b2	2.825	0.09	1	-69.73
b3	2.775	0.18	2	-69.73
b4	2.7	0.17	2	-69.73
b5	2.75	0.11	2	-69.73
b6	2.8	0.08	2	-69.73
b7	2.8	0.04	2	-69.73
b8	2.8	0.15	2	-69.73
b9	2.825	0.13	2	-69.73
b10	2.8	0.1	2	-69.73
c1	2.8	0.05	0	
c2	2.8	0.05	0	
c3	2.825	0.07	0	
c4	2.775	0.09	0	
c5	2.775	0.02	0	
o1	2.8	0.03	0	
o2	2.8	0.04	0	
o3	2.85	0.09	0	
o4	2.85	0.06	0	
o5	2.85	0.05	0	

Figure 3.21 Potential field model for GA228-04

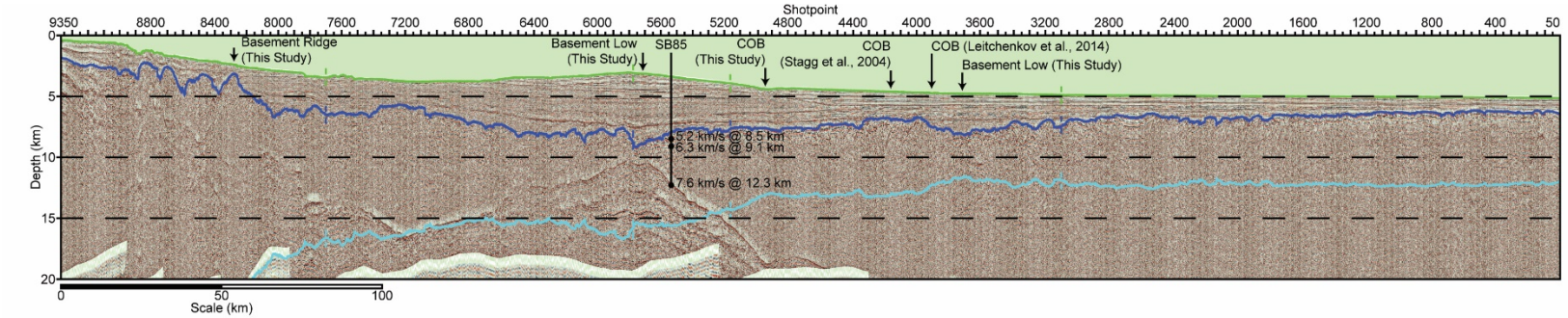

Figure 3.22 Reflection seismic profile RAE46-07

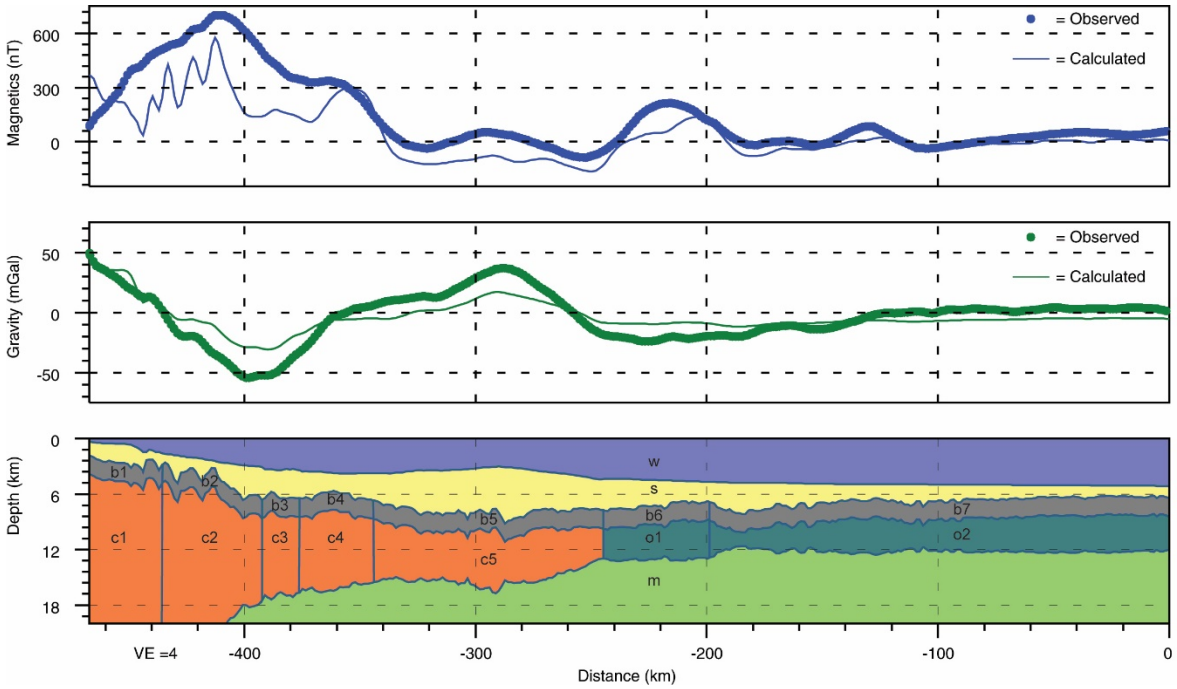

Block	Density	Suceptibility (SI)	Remnance (A/m)	Inclination (°)
w	1.03	0	0	
s	2.4	0	0	
m	3.3	0	0	
b1	2.725	0.12	2	-71.04
b2	2.725	0.16	2	-71.04
b3	2.725	0.18	2	-71.04
b4	2.825	0.14	2	-71.04
b5	2.825	0.06	2	-71.04
b6	2.75	0.11	2	-71.04
b7	2.75	0.08	2	-71.04
c1	2.8	0.07	0	
c2	2.8	0.09	0	
c3	2.8	0.09	0	
c4	2.85	0.09	0	
c5	2.85	0.02	0	
o1	2.8	0.09	0	
o2	2.8	0.07	0	

Figure 3.23 Potential field model for RAE46-07

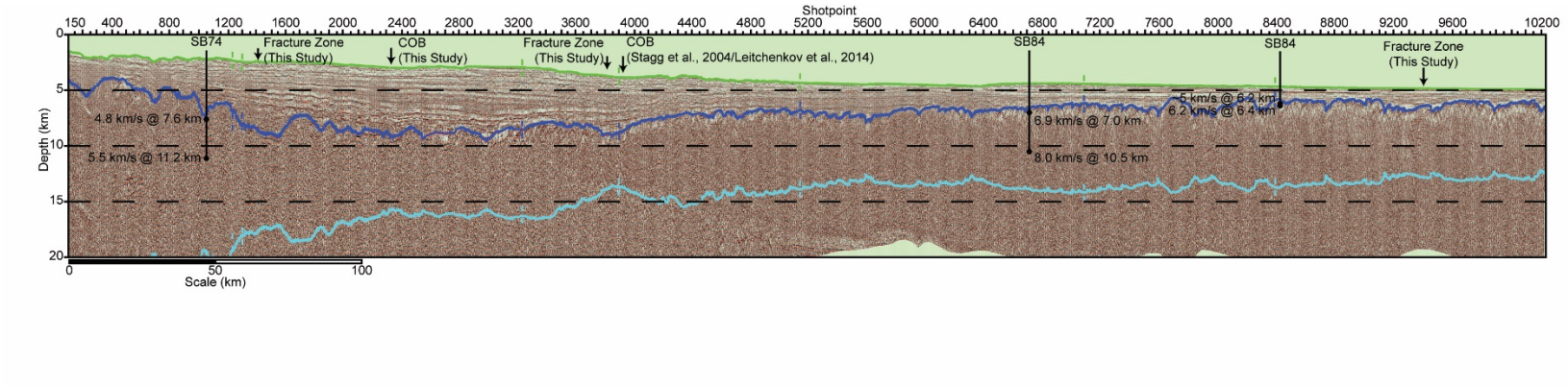

Figure 3.24 Reflection seismic profile GA229-35

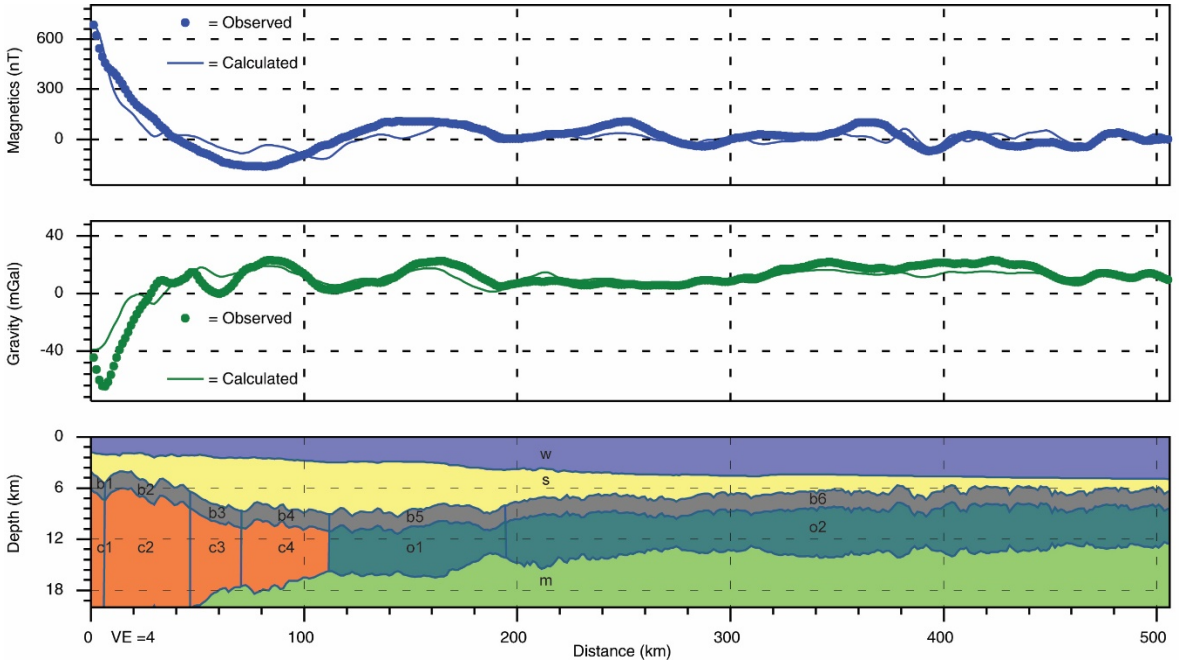

Block	Density	Suceptibility (SI)	Remnance (A/m)	Inclination (°)
w	1.03	0	0	
s	2.4	0	0	
m	3.3	0	0	
b1	2.675	0.18	2	-72.96
b2	2.775	0.05	2	-72.96
b3	2.85	0.08	2	-72.96
b4	2.825	0.09	2	-72.96
b5	2.775	0.09	2	-72.96
b6	2.725	0.1	2	-72.96
c1	2.675	0.07	0	
c2	2.775	0.02	0	
c3	2.875	0.01	0	
c4	2.85	0.02	0	
o1	2.825	0.08	0	
o2	2.85	0.05	0	

Figure 3.25 Potential field model for GA229-35

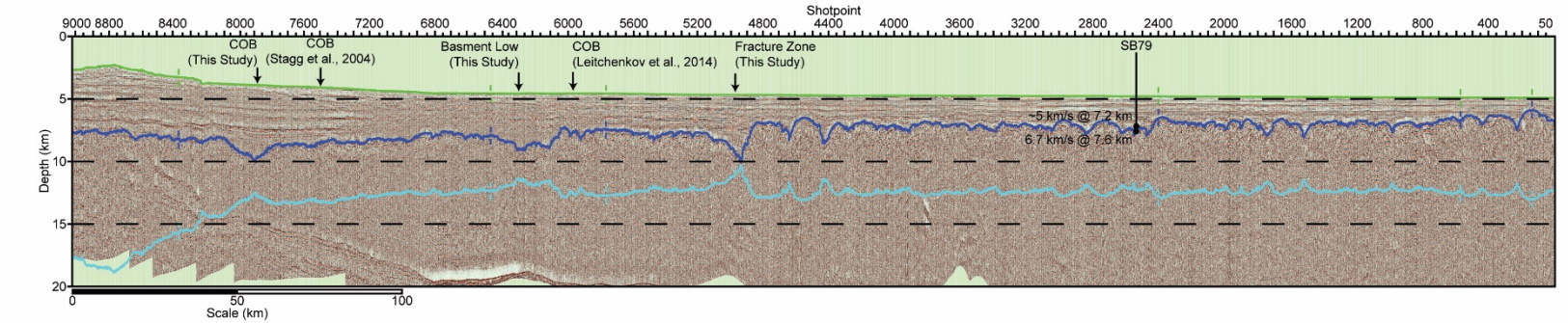

Figure 3.26 Reflection seismic profile RAE45-04

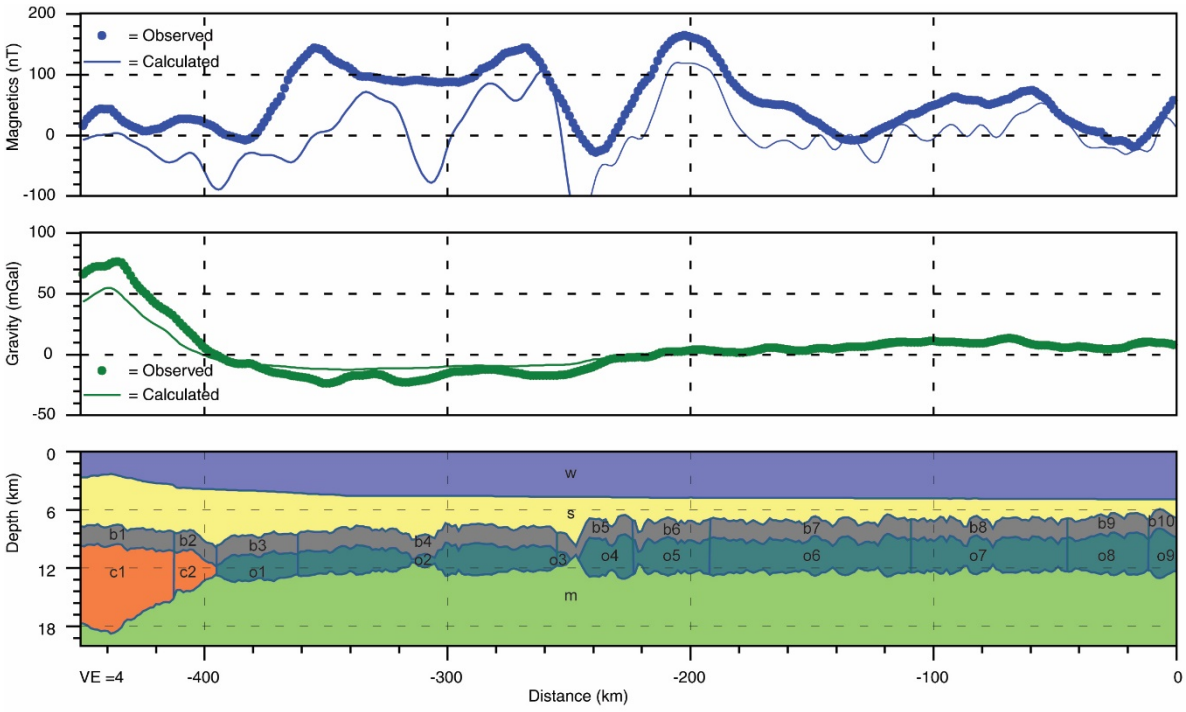

Block	Density	Suceptibility (SI)	Remnance(A/m)	Inclination(°)
w	1.03	0	0	
s	2.4	0	0	
m	3.3	0	0	
b1	2.875	0.1	2	-72.82
b2	2.825	0.13	2	-72.82
b3	2.725	0.15	2	-72.82
b4	2.725	0.18	2	-72.82
b5	2.725	0.1	2	-72.82
b6	2.8	0.18	2	-72.82
b7	2.8	0.18	2	-72.82
b8	2.825	0.08	2	-72.82
b9	2.775	0.14	2	-72.82
b10	2.825	0.1	2	-72.82
c1	2.875	0.02	0	
c2	2.825	0.02	0	
o1	2.725	0.06	0	
o2	2.725	0.09	0	
o3	2.775	0.09	0	
o4	2.775	0.09	0	
o5	2.8	0.09	0	
o6	2.8	0.01	0	
o7	2.85	0.09	0	
o8	2.8	0.01	0	
o9	2.825	0.05	0	

Figure 3.27 Potential field model for RAE45-04

have underwent at least one change in spreading ridge geometry. This spreading ridge change have arisen in response to the initial obliquity of continental rifting, or may be related to either spreading ridge propagation from the Riiser-Larsen Sea (Leinweber & Jokat, 2012) or motion of Sri Lanka (Jokat et al., 2010). Complexities in crustal structure arising from fracture zones and basement lows make determining the exact location of the COB difficult. However, our interpreted COB generally resembles that from previous efforts (e.g., Stagg et al., 2004; Leitchenkov et al., 2014) and postulates a domain of thinned continental crust domain that is approximately 150-225 km in width.

3.5 CONCLUSIONS

Using public domain geophysical data including we have examined and described the crustal structure of the Enderby Basin. Based on our observations, we propose that the Enderby Basin can be divided into three generalized morphological domains (Fig. 3.8). The Eastern Domain, is the oldest and formed at the fastest extension rates during separation of India and East Antarctica (Davis et al., 2016). The Eastern Domain is characterized by abundant volcanic features and thick ocean crust, which likely reflects an influence by the Kerguelen Hotspot. The Central Domain is characterized by two regions of varying ocean crust morphology that are divided by the EBA. The inboard region consists of thin, rugged, proto-oceanic crust, while the outboard region consists of normal thickness, well-structured, oceanic crust. Based on observations of seismic velocity, crustal structure, and the observed seaward limit of crustal thinning, we propose that the COB in the Central Domain, is significantly further inboard than that proposed by previous works (e.g., Stagg et al., 2004; Leitchenkov et al., 2014). Our preferred tectonic model, for the formation of the inboard region of proto-oceanic crust, suggests that it was formed shortly

after continental breakup, when melt production rates were low. Only after reorganization of the magmatic system, potentially by a change in spreading rate, ridge geometry, and/or gradual increase in melt production, was seafloor spreading able to produce normal thickness, well-structured, oceanic crust. The Western Domain is the youngest portion of the Enderby Basin. Ocean crust in this domain is of variable thickness (4.5-8 km) with abundant basement lows and fracture zones. The variable structure crustal of the Western Domain reflects formation at ultraslow extension rates, and may preserve structure related to a spreading ridge reorganization event. The formation of this domain was potentially complicated by initially oblique continental rifting, ridge propagation from the Riiser-Larsen Sea, or independent motion of Sri Lanka. Compiling these observations of sediment thickness (Fig. 3.6), crustal thickness (Fig. 3.7), and crustal structure (Fig. 3.8) for the Enderby Basin, helps to provide insight into the manner in which East Gondwana fragmented and demonstrates that much of the early seafloor spreading in the Indian Ocean was complex and highly variable.

Chapter 4: Influences on the development of volcanic and magma poor morphologies during passive continental rifting[2]

ABSTRACT

Numerical experiments of passive continental extension with decompressive mantle melting have been conducted to investigate controls on the development of end-member, volcanic and magma-poor, rifted margins. A prediction of end-member margin morphology is made by comparing the relative timing of continental breakup and start of magmatic emplacement. Volcanic margins are interpreted to form when magmatic emplacement begins prior to the full thinning of the continental crust, while magma-poor margins are predicted to form when continental breakup precedes any magmatic emplacement. Systematic investigations of potential influencing variables demonstrate that a variety of factors may influence this relative timing with model results producing a spectrum of magmatic character. Of the investigated factors, the initial lithosphere geotherm and crustal thickness appear to be the most significant influences on margin morphology. Independent variation of either variable is capable of altering the predicted end-member morphology between volcanic and magma-poor. Variations in mantle potential temperature, extension rate, and crustal rheology demonstrate an ability to influence passive margin magmatic character, but are unable to independently induce development of a magma-poor margin. In aggregate, model results suggest mantle exhumation and formation of a magma-poor margin is encouraged by: a depressed lithosphere geotherm, thin continental crust, rapid extension rates, low mantle potential temperature, and a strong crustal rheology. Relatively early magmatic emplacement and formation of a volcanic margin is predicted for the majority of modeled conditions, and

[2] Davis, J.K., Lavier, L.L., (In Review). Influences on the development of volcanic and magma poor morphologies during passive continental rifting. Geosphere. Lavier assisted in experiment design and interpretation.

appears bolstered by: an elevated geotherm, thick continental crust, slow extension, high potential temperature, and a weak crustal rheology.

4.1 INTRODUCTION

The end product of continental extension, rifted passive margins, exhibit extreme variations in the distribution of continental crust, patterns of subsidence/sedimentation, and magnitude and timing of volcanism accompanying continental breakup. The most widely used passive margin morphology classification scheme defines two end-members morphologies, volcanic and magma-poor (e.g., Franke, 2013). Assignment of these definitions is related to the relative timing of magmatic emplacement and continental breakup. Volcanic margins are characterized by voluminous magmatic emplacement prior to the full thinning of continental crust (Mutter et al., 1982; White & McKenzie, 1989; Coffin & Eldholm, 1993; Holbrook & Kelemen, 1993; Mjelde et al., 1997; Mjelde et al., 1998; Eldholm et al., 2000; Mjelde et al., 2002; Hopper et al., 2003); while magma-poor passive margins express negligible volcanism prior to final continental breakup (Dean et al., 2000; Boillot & Froitzheim, 2001; Whitmarsh et al., 2001).

It is important to note, that the interpretation of either end-member morphology does not necessarily diagnose the driver of continental rifting (i.e., active vs. passive; Sengör & Burke, 1978) . While active, plume induced, continental rifting likely precludes the development of a magma-poor margin; externally driven, passive continental extension appears capable of generating margins of either morphologic character (Hopper et al., 1992; Holbrook et al., 1994; Van Wijk et al., 2001). Because the extensive partial melting of hot, upwelling asthenospheric mantle is necessary to generate magma during passive continental extension, the distribution of strain throughout the lithosphere may exert a

dominant control on the timing and extent of rift-related magmatism. Accordingly, understanding the relationship between tectonic and magmatic processes is essential for unraveling the factors that control the development of passive continental rift systems and understanding the varying observed morphologies of passive margins (Pérez-Gussinyé et al., 2001; Pérez-Gussinyé & Reston, 2001). To provide insight into these influencing factors, we have performed 2D thermomechanical numerical modeling experiments. These experiments systematically explore potential controlling factors and offer constrained estimates concerning the timing and magnitude of melt produced during passive continental rifting.

4.2 PASSIVE MARGIN MORPHOLOGIC VARIATIONS

Volcanic passive margins are characterized by significant magmatic emplacement preceding and/or synchronous with the start of continental rifting (Mutter et al., 1982; Holbrook & Kelemen, 1993; Geoffroy, 2005). This pre-breakup volcanism indicates the relatively early development of mature magmatic systems that are capable of generating and emplacing significant volumes of melt. These magmatic systems may manifest as onshore igneous emplacements, subaerial seaward dipping reflector sequences, and/or magmatic underplating of the continental crust (Mutter et al., 1982; Mutter et al., 1985; White et al., 1992; Coffin & Eldholm, 1994; Eldholm & Grue, 1994; Planke et al., 2000; Talwani & Abreu, 2000). Globally, the majority of passive margins exhibit some form of volcanic morphology (Skogseid, 2001; Menzies, 2002), including large portions of the northern, central, and southern Atlantic Ocean, the southern Red Sea, and nearly the entirety of the Indian Ocean (Mutter et al., 1985; Coffin & Eldholm, 1992; Mahoney & Coffin, 1997; Planke et al., 2000). This distribution suggests that the processes responsible

for the formation of volcanic passive margins are relatively common and contribute significant volumes to the global igneous activity budget (Coffin and Eldholm, 1994).

Magma-poor margins are less common and are characterized by an apparent absence of significant volcanism prior to the full thinning of the continental crust (Boillot and Froitzheim, 2001; Dean et al., 2000; Whitmarsh et al., 2001). Because melt generation is delayed relative to continental breakup, post-breakup extension is accommodated through the exhumation of the continental lithospheric mantle, rather than through the emplacement and formation of oceanic crust (e.g., Manatschal, 2004; Lavier & Manatschal, 2006). Domains of exhumed lithospheric mantle and magma-poor morphologies have been observed or interpreted along the margins of Iberia-Newfoundland (Boillot et al., 1995; Manatschal & Bernoulli, 1999; Whitmarsh et al., 2001; Hopper et al., 2007; Reston, 2007; Tucholke & Sibuet, 2007; Péron-Pinvidic & Manatschal, 2009; Van Avendonk et al., 2009), Brazil-Angola (Mohriak et al., 1990; Contrucci et al., 2004; Mohriak et al., 2008; Aslanian et al., 2009; Contreras et al., 2010), Southern Australia-East Antarctica (Direen et al., 2007; Direen et al., 2011; Espurt et al., 2012; Gillard et al., 2015; Gillard et al., 2016), the bight of East India (Bastia et al., 2010; Nemcok et al., 2012; Radhakrishna et al., 2012), and the South China Sea (Zhou et al., 1995; Hayes & Nissen, 2005; Yan et al., 2006; Zhou & Yao, 2009; Savva et al., 2013; Lester et al., 2014; McIntosh et al., 2014). This global distribution suggests that development of a magma-poor margin is not a local phenomenon, but a relatively common result of passive continental extension.

4.3 POTENTIAL INFLUENCING FACTORS

A number of possible controls have been suggested to explain observed differences in continental rift style and the varying morphologies of passive margins. The manner and relative significance of how these suggested controls actually impact tectonic processes and passive margin formation is still a subject of ongoing debate (Karner et al., 2007; Armitage et al., 2010; Huismans & Beaumont, 2014; Svartman Dias et al., 2015; Brune, 2016). Utilizing simplified kinematic models of uniform, instantaneous extension, McKenzie & Bickle (1988) and White & McKenzie (1989) suggested that mantle potential temperature acts as the first-order control on the magnitude of syn-rift volcanism during continental breakup. Following the addition of finite extension rates to these kinematic models, Bown & White (1995) suggested that extension rates may instead act as the controlling factor and that diffusive heat loss may temper the influence of mantle potential temperature. Armitage et al. (2010) used dynamic numerical models of viscous, decompressive, mantle melting to suggest that in the presence of a thermal anomaly, the extensional history of a basin, particularly the existing lithosphere structure, significantly influences the resulting margin morphology. Additional factors, including lithosphere thermal structure, initial crustal thickness, and lithosphere rheology have been suggested by a variety of authors, as significant influences on the style of continental rift development and passive margin morphology (England, 1983; Kusznir & Park, 1987; Buck, 1991; Huismans et al., 2005; Svartman Dias et al., 2015; Brune, 2016). These potential controls are summarized in Table 4.1 and are investigated within our numerical modeling experiments to assess their relative importance and manner of influence.

Variable	Values to test		
Mantle Potential Temperature (°C)	1300	**1350**	1400
Extension Rate (full; cm/yr.)	0.5	**1.0**	2.0
Lithosphere Geotherm (Surface Heat Flow, mW/m^2)	40	**47.5**	55
Crustal Thickness (km)	30	**35**	
Crustal Rheology	Dry Qtz.	**Dry Plag.**	

Table 4.1 Potential controlling factors and parameter space.

4.4 METHODOLOGY

4.4.1 Numerical Model Overview

We utilize an adapted version of the explicit, Lagrangian FLAC algorithm (Poliakov et al., 1993; Lavier & Manatschal, 2006; Tan et al., 2012; Svartman Dias et al., 2015) to test the manner in which proposed controls (Table 4.1) influence the relative timing of the first emplacement of melt and the full thinning of the continental crust. FLAC has proven reliable for a number of investigations into continental rifting processes (e.g., Lavier & Manatschal, 2006; Svartman Dias et al., 2015) and was found to be suitable for the adaptations and new melting parameterizations required for this work. FLAC implements brittle, elastoplastic deformation following a Mohr-Coulomb yield criterion (Lavier & Buck, 2002) and simulates localized faulting using a strain-weakening rule (Lavier et al., 2000; Huismans & Beaumont, 2002). To simulate ductile deformation, FLAC employs a nonlinear, Maxwell, viscoelastic, constitutive update with viscosity determined via experimental flow laws (Bürgmann & Dresen, 2008). FLAC's ability to implement a range of brittle-ductile deformation processes makes it particularly suitable

for simulating the varying styles of deformation that occur as the brittle continental crust is thinned and the warm mantle asthenosphere upwells.

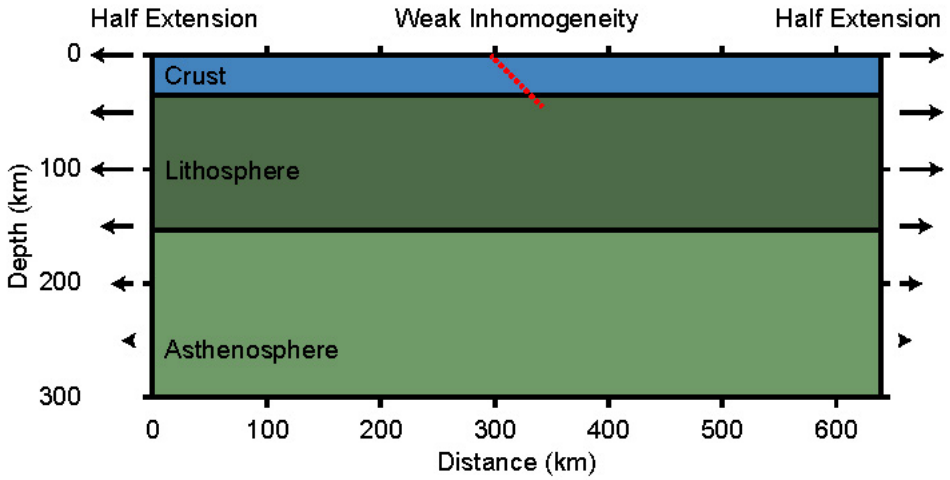

Figure 4.1 Numerical model initial setup.

The model domain is 640 km by 300 km. The continental crust is shown in blue, the mantle lithosphere in dark green, and the mantle asthenosphere in light green. A weak homogeneity, shown in red, helps localize deformation is the center of the model. Half rates of extension are applied to the upper 100 km of each side of the model. Below 100 km depth, the extension rate is linearly reduced and reaches zero at the base of the model.

4.4.2 Model Domain

To capture important lithosphere/asthenosphere deformational processes, our numerical model covers a domain that is 640 km in width and 300 km in depth (Fig. 4.1). Our model mesh utilizes variable element spacing in both the vertical and horizontal directions. In the upper 150 km depth, element spacing is 1 km, while in the lower 150 km, the resolution is reduced to every 2 km. Horizontal element spacing is symmetric about the center of the model, with finer resolution at the center and lower resolution at the edges. The outermost 120 km of the model has an element spacing every 3 km, the middle 100

km domain every 2 km, and the inner 100 km every 1 km. The initial model setup is laterally homogenous in both physical and thermal properties and applies symmetric boundary conditions. The model is vertically stratified into four layers: upper continental crust, lower continental crust, lithospheric mantle, and asthenospheric mantle. To investigate the influence of crustal thickness of final passive margin morphology the thickness of the lower crust is varied between 18-23 km., while the upper crust is held at a constant value of 12 km. The thicknesses of the lithosphere and asthenosphere vary as a function of our thermal structure as discussed below. To investigate the influence of crustal rheology on margin morphology, we vary the rheological properties of the continental crust. The rheological properties of the crust and mantle phases are summarized in Table 4.2. The differential stress profiles of each varying model is shown in Figure 4.2. To localize deformation an initial weak inhomogeneity with minimal cohesion and friction angle is positioned in the center of the model. The inhomogeneity has the same mineral phase and temperature properties as the surrounding material. This inhomogeneity simulates a preexisting weakness, such as a fault, and has a dip of 45° from the surface to a depth of 45 km.

Phase	**ρ (kg/m^3)**	**Θ (°)**	**Θ' (°)**	**C (MPa)**	**A (MPa^{-n}/s)**	**E_a (kJ/mol)**	**n**
Dry Plagioclase (crust)	2800	30	15	40	1.25e-1	3e5	3.05
Dry Quartz (crust)	2800	30	15	40	5e2	2e5	3.3
Dry Olivine (mantle)	3300	30	15	40	7e4	5.2e5	3

Table 4.2 Physical and rheological properties of crust and mantle phases

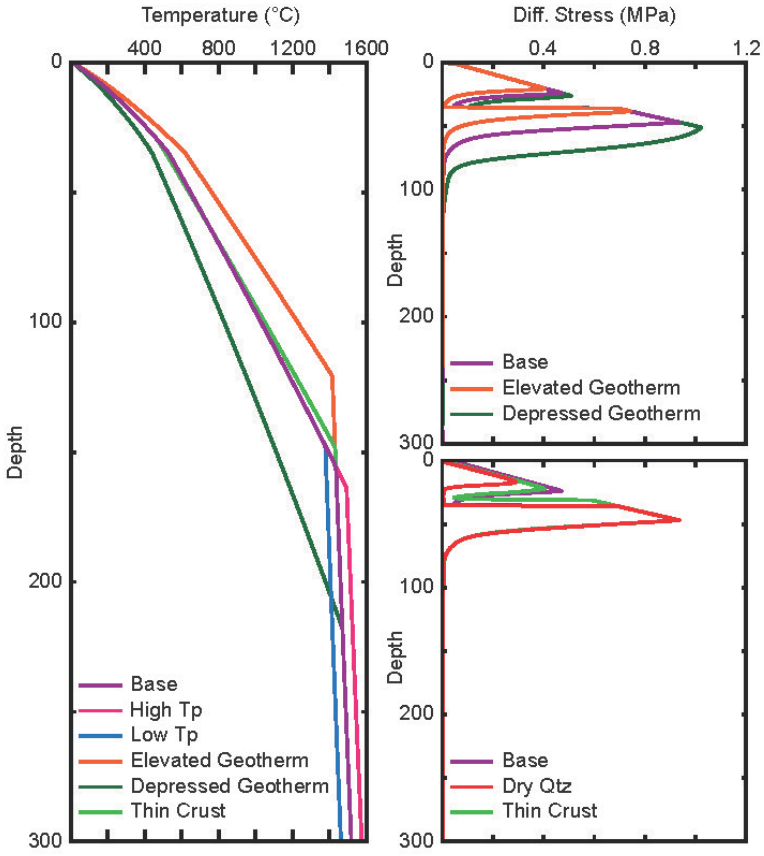

Figure 4.2. Temperature and differential stress profiles

4.4.3 Boundary Conditions

FLAC utilizes a Winkler Formulation for the bottom boundary condition to simulate regional isostasy. Upwelling mantle is replaced with asthenosphere of equivalent potential temperature (McKenzie & Bickle, 1988). The surface topography is free. Temperatures at the surface of the model are fixed to 11℃ while the basal temperatures are determined by input model values of mantle potential temperature. To simulate full spreading rates, we symmetrically extend the upper 100 km (the viscous lithosphere domain) on both sides of the model at constant half-rates as prescribed by our input

parameter extension rate (0.5 cm/yr.; 1.0 cm/yr.; 2.0 cm/yr.). The lower, less viscous, 200 km of our model is extended at lower, linearly decreasing extension rates, with zero extension applied at the base of the model. Adiabatic heating and cooling is included within our model to appropriately capture thermal changes related to compression/decompression. No heat flow is allowed through the sides of our model.

4.4.4 Initial Thermal Structure

The thermal structure of our numerical model is composed of two parts: a steady-state lithosphere geotherm (Hasterok & Chapman, 2011) and an asthenosphere adiabat of equivalent potential temperature (Fig. 4.2). Several of the variables investigated in this work affect the formulation of this thermal structure, including chosen input values of mantle potential temperature, surface heat flow, and crustal thickness. An input value of mantle potential temperature (1300℃; 1350℃; 1400℃) is utilized to calculate an asthenosphere adiabat from the surface to 300 km depth (McKenzie & Bickle, 1988). The lithosphere geotherm is steady-state and is calculated from the formulation of Hasterok & Chapman (2011). For all models we use constant values for the thickness of upper continental crust (12 km), surface temperature (11°C), radiogenic heat production in the lower crust and mantle (0.4 μW/m3 and 0.02 μW/m3 respectively), and thermal conductivity in the crust and mantle (2.3 W/m/K and 3.3 W/m/K respectively). We vary input values for surface heat flow (40.0 mW/m2; 47.5 mW/m2; 55.0 mW/m2) and determine upper crust radiogenic heat production using the empirical relationship outlined within Hasterok & Chapman (2011). To calculate temperature with depth, we perform a 1-D bootstrapping method starting with our surface temperature, surface heat flow, and using the layered definitions of thermal conductivity and heat production (Hasterok & Chapman,

2011). Once we calculate a temperature greater than or equal to our asthenosphere adiabat, we end our geotherm formulation and set the corresponding depth as the lithosphere-asthenosphere boundary (LAB). Regions deeper than the LAB, have temperatures equivalent to the asthenosphere's adiabat, while regions shallower than the LAB have temperatures prescribed via the lithospheric geotherm. Within the lithospheric geotherm formulation, the chosen value of surface heat flow largely controls the overall lithosphere thermal structure (Hasterok & Chapman, 2011). Low values of surface heat flow correspond to a depressed lithospheric geotherm and a deep LAB, while higher values of surface heat flow correspond to an elevated geotherm and a shallow LAB. Chosen values of mantle potential temperature have a minor effect on the depth of the LAB as they shift the adiabat toward lower or higher temperatures. The thermal structure of all models listed in Table 4.3 are shown in Figure 4.2.

4.4.5 Mantle Melting

In order to offer constrained estimates of decompressive melt production, we utilize the peridotite melting parameterization of Katz et al. (2003). This parameterization assumes batch (equilibrium) melting and offers an estimate of the weight fraction of melt as a function of the temperature and pressure conditions, as well as water and clinopyroxene content. We implement this parameterization using markers that track the advection of material phase, weight fraction melt, and pressure/temperature history. Temperature and pressure conditions are updated in FLAC at each time step. For all of the experiments presented in this paper mantle phases are anhydrous and contain 15% weight clinopyroxene. Pressure-dependent functions for the mantle solidus and liquidus follow from Katz et al. (2003). Potential melting conditions are checked within the lithospheric

and asthenospheric mantle at each time step. For thermal conditions above the solidus, melt production is solved using a fourth-order Runge-Kutta scheme, and assumes melting at constant entropy with a thermal correction for latent heat (Katz et al., 2003). For simplicity, melt and matrix phases advect together and do not separate.

4.4.6 Predicting Margin Morphology

To assess the end-member margin morphology produced by each model, we compare the relative timing of first magmatic emplacement to continental breakup. Since we do not allow melt and matrix phases to segregate, we require an estimate for the first age of magmatic emplacement. To estimate this age, we compare model conditions against melt extraction criteria outlined in (Schmeling, 2006). Schmeling (2006) contends that if melt fractions are above 0.02 and vertically distributed over a critical thickness of 3-5 km, then melt extraction and magmatic emplacement will occur. We follow these criteria and for each model output (every 0.05 Myrs) search for regions of >2% melt that are vertically connected over thicknesses greater than 3 km. The youngest model age that meets these criteria is assigned as the start of magmatic emplacement. It is important to emphasize that although we use these criteria to estimate when extraction and emplacement begins, we do not actually simulate melt extraction or emplacement within any of the models presented in this paper. We estimate the timing of continental breakup more directly. Continental breakup is assumed to occur when the continental crust is first thinned to <1 km, the minimum resolution of our model. If our criteria for magmatic emplacement are met prior to continental breakup, we assume magmatic emplacement will occur within the overlying continental crust, and result in a passive margin reflecting volcanic end-member morphology. Conversely, if continental breakup occurs first, we assume post-breakup

extension is accommodated by lithospheric mantle exhumation, and the resulting passive margin will reflect a magma-poor morphology. This volcanic or magma-poor classification scheme, while simple and binary, highlights the most obvious manner in which the simulated margins may vary. Additionally, this classification is tied to our model's ability to resolve the relative timing of major events, which we believe is well constrained.

To help tie model results to observations from real-world passive margin, we provide rough estimates for the thickness of igneous crust and the width of various morphologic domains produced in each model. The thickness of igneous crust estimated at each model output by the calculation of melt thickness. Melt thickness is computed through the integration of new melt produced across the model domain (km^2) and division by the applied extension (km) over the time between outputs. Values of melt thickness are a rough estimate and should be viewed with a degree of skepticism, particularly at higher values. In real world systems and in preliminary tests of more complex numerical simulations, the generation of volcanic or oceanic crust via the segregation of melt and mantle matrix phases, limits asthenosphere upwelling and tends to equilibrate at melt production conditions of around 6 km (Bown & White, 1994). We estimate the onset of seafloor spreading as when melt thickness first reaches the 6 km threshold. If following continental breakup, melt thickness is only between 0-6 km, then we assume a domain of proto-oceanic crust (<6km in thickness) is formed. To provide a rough estimate of the domain widths preserved on the conjugate sides of each modeled set of passive margins, the temporal difference between continental breakup, start of magmatic emplacement, and establishment of seafloor spreading can be multiplied by half of the applied extension rate. While useful as a tool to assess the spectrum of margins produced, because melt migration is neglected, the width of this domain width should be viewed only as an approximation.

4.4.7 Parameter Space & Model Runs

We test a range of potential factors that might influence continental rifting dynamics, the relative timings of magmatic emplacement and continental breakup, and the final margin morphology. These variables include: (1) Mantle potential temperature, (2) extension rate, (3) lithosphere thermal structure, (4) crustal thickness, and (5) crustal rheology. Given that a full exploration of this parameter space would require 108 individual model runs, we instead choose a base model (bold, Table 4.1) and perform 8 experimental runs where we systematically alter only one variable per run. This workflow provides us with 9 model runs, from which we can analyze and compare each variable's relative influence. We recognize that the numerical experiments presented in this paper are unable to cover all potential permutations of continental rifting. However, the systematic exploration of our parameter space can help provide critical insight into the manner in which each variable potentially affects margin morphology, and can help guide future, more detailed, numerical modeling efforts.

4.5 RESULTS

4.5.1 Overview

We present animations and graphics of all model run results. Model animations display deforming lithosphere and asthenosphere phases, the second invariant of strain, and weight fraction melt. The second invariant of strain highlights deformation and provides insight into the faulting style. For display simplicity, the second invariant of strain is masked immediately prior to the onset of melting. In addition to the animations, we present graphics (Fig. 4.3-4.11) displaying melt thickness and minimum crustal thickness from each model run. These graphics compare the relative timing of first magmatic emplacement

and continental breakup, and allow for the prediction of either a volcanic or magma-poor morphology. The formulation of melt thickness, and criteria for the age of first magmatic emplacement and continental breakup are discussed above in the Methodology.

4.5.2 Base Model

The Base model is run with using an asthenosphere with a potential temperature of 1350℃, an extension rate of 1 cm/yr., a lithosphere geotherm with a surface heat flow of 47.5 mW/m2, a crustal thickness of 35 km, and a dry plagioclase crustal rheology (bold, Table 4.1). In the animation (Anim. 4.1) we observe crustal deformation progress through several phases and styles. Initial extension exploits our deep, weak inhomogeneity, and the through formation of a conjugate fault, establishes an H-block (Lavier & Manatschal, 2006; Van Avendonk et al., 2009). By 2.50 Myrs, the development of a shallow antithetic fault localizes brittle deformation in the upper portions of the continental crust. Ductile deformation in the lower crust begins to reduce the angle of our initial, deep-seated faults. At 6.20 Myrs, some portions of the crust have thinned to beta factors greater than 2. Starting at 7.00 Myrs, multiple synthetic and antithetic faults begin to develop. These faults help to connect the deeper low-angle faults to the upper crust. The first melt is generated 10.30 Myrs after the start of extension. This first melting occurs in upwelling asthenosphere at 2.6 GPa. The pressure and temperature conditions of this initial melt agree with the expected conditions predicted for anhydrous melting of mantle with a potential temperature of 1350℃ (Katz et al., 2003). Utilizing the Schmeling (2006) criteria, magmatic emplacement is estimated to begin at 11.00 Myrs (Fig. 4.3). Continental breakup occurs later, following the final thinning of superficially-exposed lower crust at 15.05 Myrs (Fig. 4.3). Since initial magmatic emplacement is estimated to occur 4.05 Myrs prior to

continental breakup, these experiments suggest Base model conditions will favor volcanic intrusion of the continental crust and formation a passive margin demonstrating a volcanic morphology. We estimate that for the Base model, the width of the intruded domain on each conjugate margin will be at least 20.25 km and have emplaced intrusive phases of up to 11.9 km in thickness at the time of continental breakup.

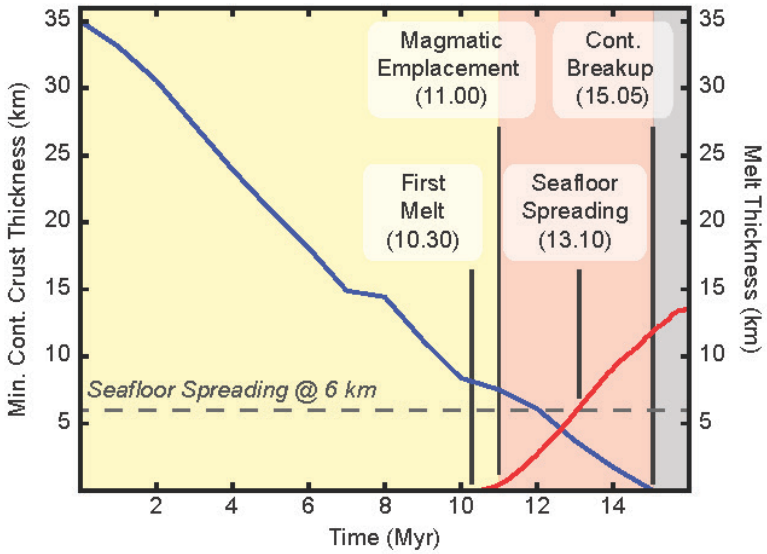

Figure 4.3 Base model results

Minimum continental crust thickness, blue, and melt thickness, red, since time since start of rifting for the Base model. Magmatic emplacement begins prior to continental breakup. Volcanic intrusion of the continental crust and formation of a volcanic margin is estimated to occur during the time period outlined in red.

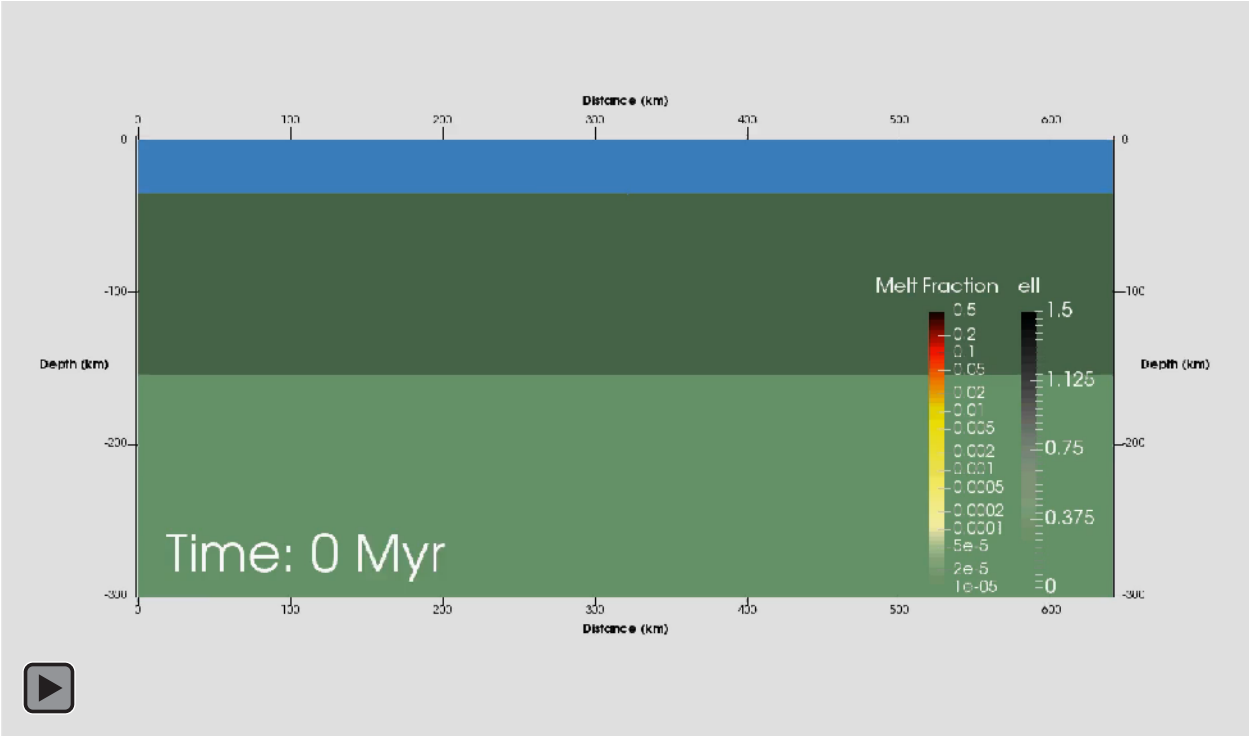

Animation 4.1 Base model rifting simulation.

The crust is shown in blue, lithosphere in dark green, and the asthenosphere in light green. The second invariant of strain (eII) is shown to highlight deformation and is masked prior to the start of melting. Melt is displayed corresponding to pooled weight fraction melt. In the Base model, the first melt is generated at 10.30 Myrs, magmatic emplacement is estimated to begin at 11.00 Myrs, seafloor spreading melt thicknesses are reached at 13.10 Myrs, and continental breakup occurs at 15.05 Myrs. Because magmatic emplacement begins prior to continental breakup, the Base model is predicted to generate a passive margin with a volcanic morphology.

4.5.3 Mantle Potential Temperature

We present two model runs that help demonstrate the influence of mantle potential temperature on margin morphology during passive continental extension. These include a Low Tp model corresponding to a potential temperature of 1300℃ (lower than the base model by 50℃) and a High Tp model corresponding to a potential temperature of 1400℃ (higher than the base model by 50℃). The Low Tp model undergoes crustal deformation that is initially similar to the base model (Anim. 4.2). However, by 11 Ma, after the development of more complex fault systems, the rates of crustal thinning between the Base and Low Tp models begin to diverge. The first melt, in the Low Tp model, is generated at 10.85 Myrs and at pressures of 2.1 GPa (lower pressure due to lower potential temperature). Magmatic emplacement is estimated to begin at 11.55 Myrs., with continental breakup following at 13.05 Myrs (Fig. 4.4). Since initial magmatic emplacement occurs 1.5 Myrs prior to continental breakup, the Low Tp model demonstrates a volcanic morphology. Interestingly, even after continental breakup and formation of a volcanic passive margin, the Low Tp model has not reached melt production rates capable of sustaining seafloor spreading (Fig. 4.4). We suggest that during the 1.6 Myrs between continental breakup and establishment of seafloor spreading melt production rates, a domain of proto-oceanic crust will form outboard of the seaward limit of continental crust. We estimate the intruded continental domain to be 7.5 km and the proto-oceanic domain to be 8 km in width for each conjugate margin of the Low Tp model. Maximum thicknesses of intrusive crust is estimated to reach 3.2 km.

The High Tp model undergoes crustal deformation in a manner that appears to diverge from the Base model by as early as 3 Myrs (Anim. 4.3). Similar to the Base model, The High Tp model develops shallow antithetic faults that localize brittle deformation in the upper crust, however the location of these faults differs from those in the Base model.

The first melt, in the High Tp model, is generated at 8.45 Myrs at pressures of 3.25 GPa (higher pressures due to higher potential temperature). Magmatic emplacement is estimated to begin at 9.35 Myrs, with continental breakup following at 12.20 Myrs (Fig. 4.5). Since initial magmatic emplacement occurs 2.85 Myrs prior to continental breakup, these experiments suggest the High Tp model will form a passive margin demonstrating a volcanic morphology. The width of the intruded continental domain is estimated to be 15.5 km for each conjugate margin and up to 14.5 km in thickness. Based on our binary classification scheme, both the Low Tp and High Tp models appear to favor formation of volcanic margins and therefore do not appear to be a significant and independent control on determining end-member passive margin variability. However, model results demonstrate clear differences in the width and thickness of the volcanic domain and suggest that mantle potential temperature provides an important influence in the magmatic characteristics of passive margins.

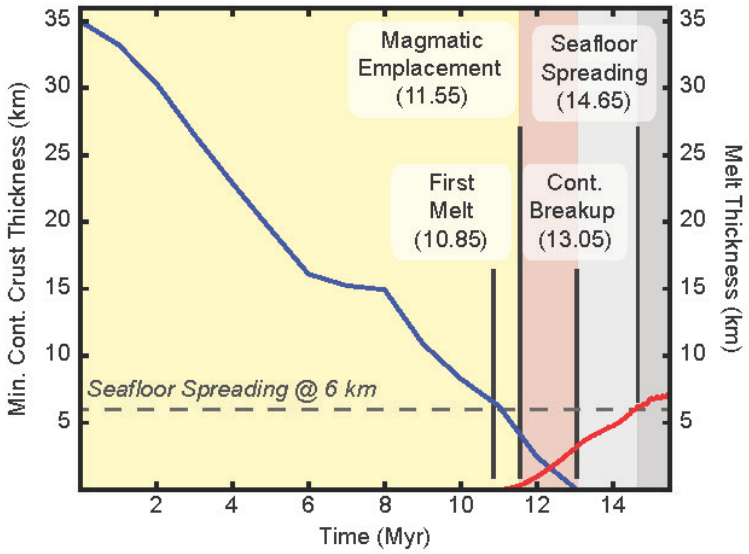

Figure 4.4 Low Tp model results

Minimum continental crust thickness, blue, and melt thickness, red, since time since start of rifting for the Low mantle potential temperature model. Magmatic emplacement begins prior to continental breakup. Volcanic intrusions within the continental crust and formation of a volcanic margin are estimated to occur during the time period outlined in red.

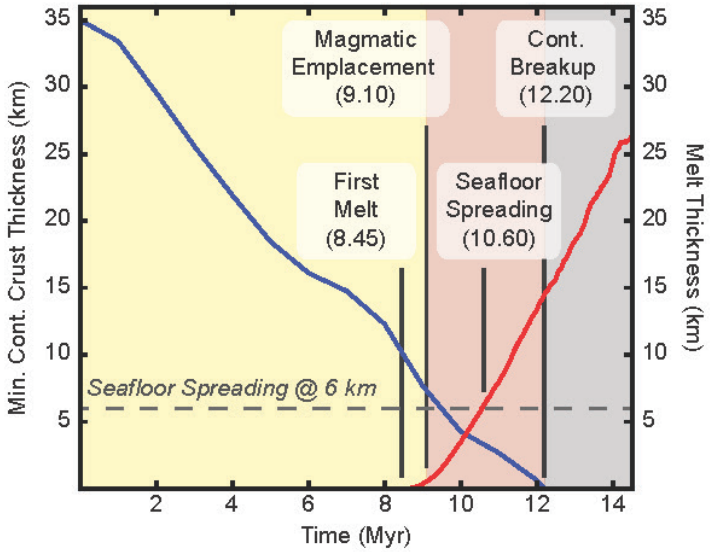

Figure 4.5 High Tp model results

Figure 5. Minimum continental crust thickness, blue, and melt thickness, red, since time since start of rifting for the High mantle potential temperature model. Magmatic emplacement begins prior to continental breakup. Volcanic intrusion of the continental crust and formation of a volcanic margin is estimated to occur during the time period outlined in red.

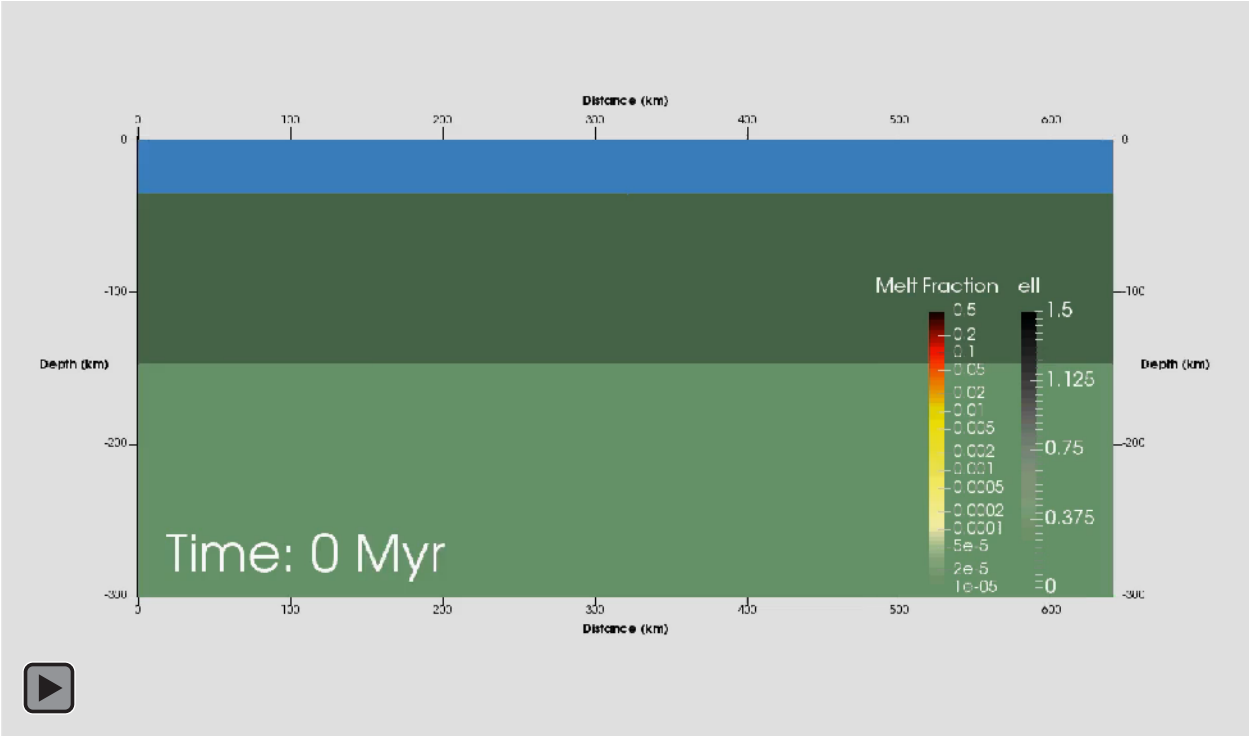

Animation 4.2 Low Tp model rifting simulation

Displayed variables are identical to those shown in Animation 4.1. In the Low Tp model, the first melt is generated at 10.85 Myrs, magmatic emplacement is estimated to begin at 11.55 Myrs, continental breakup occurs at 13.05 Myrs, and seafloor spreading melt thicknesses are reached at 14.65 Myrs. Because magmatic emplacement begins prior to continental breakup, the Low Tp model is predicted to generate a passive margin with a volcanic morphology.

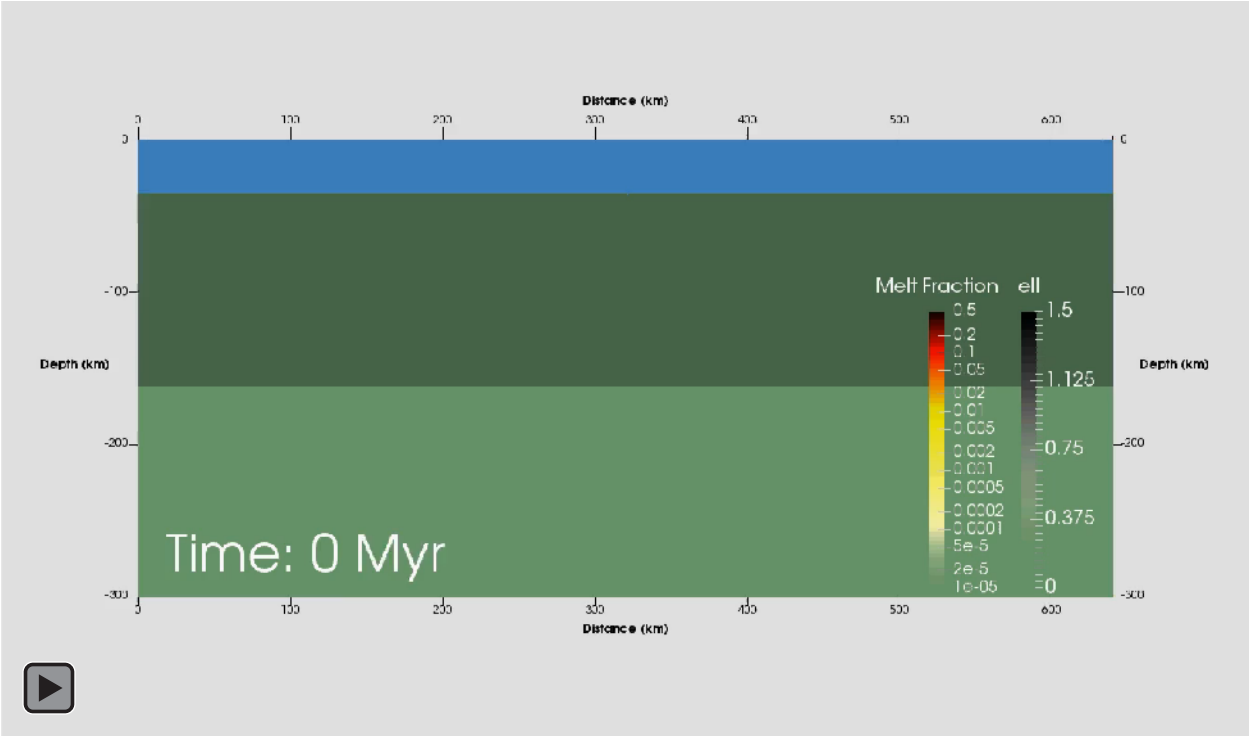

Animation 4.3 High Tp model rifting simulation

Numerical simulation of continental rifting for the High Tp model. Displayed variables are identical to those shown in Animation 4.1. In the High Tp model, the first melt is generated at 8.45 Myrs, magmatic emplacement is estimated to begin at 9.10 Myrs, seafloor spreading melt thicknesses are reached at 10.60 Myrs, and continental breakup occurs at 12.20 Myrs. Because magmatic emplacement begins prior to continental breakup, the High Tp model is predicted to generate a passive margin with a volcanic morphology.

4.5.4 Extension Rate

Two experimental runs were conducted to investigate the influence of Fast (2.0 cm/yr.) and Slow (0.5 cm/yr.) extension rates on passive continental rifting. Please note when comparing the crustal thickness graphics for the extension rate experiments (Fig. 4.6 & 4.7), the scales of the x-axis have been altered compared to other model graphics. In the Fast model (Anim. 4.4), we observe crustal faulting that resembles a more rapid form of the deformation seen in the Base model. By as early as 3 Myrs, the crust has thinned to beta factors in excess of 2. The first melt is generated at 5.15 Myrs, at pressures (2.6 GPa) identical to the Base model. Magmatic emplacement is estimated to begin at 5.55 Myrs, with continental breakup closely following at 5.65 Myrs (Fig. 4.6). Melt production does not reach seafloor spreading thicknesses until 7.0 Myrs. As suggested by Bown and White (1995), rapid extension reduces time-dependent diffusive heat loss. In only the Fast model, we observe a significant portion of continental lithosphere being induced to melt (Anim. 4.4), suggesting that very little lithosphere heat content was lost due to lateral heat diffusion during upwelling. Magmatic emplacement occurs slightly earlier than continental breakup in the Fast model, suggesting that these conditions might favor a very limited volcanic end-member margin morphology. The intruded crustal zone for each conjugate margin is estimated at 1.0 km for the Fast model with intrusive phase thicknesses of only 0.3 km. The 1.85 Myrs between first melt generation and establishment of seafloor spreading is the fastest increase in melt production observed in all models. However, despite this rapid increase in melt productivity, this experiment predicts the formation a zone of proto-oceanic crust outboard of the seaward limit of continental crust. We estimate the conjugate widths of the proto-ocean domain to be 13.5 km.

In the Slow model (Anim. 4.5) we observe crustal deformation processes that resemble a sluggish version of the Base model. The first melt is generated at 19.35 Myrs

and at pressures identical to Base model (2.6 GPa). As expected for asthenosphere with higher diffusive heat lost, this initial melt is produced within asthenosphere that is furthest from the laterally adjacent cooler lithosphere. Asthenosphere proximal to the lithosphere is not induced to melt until lower pressures. Magmatic emplacement is estimated to begin at 20.70 Myrs. Continental breakup occurs much later, at 28.0 Myrs (Fig. 4.7). The 7.3 Myrs between first magmatic emplacement and continental breakup, is the longest time delay of all model runs. Results from this Slow model indicate that lower rates of continental extension will tend to favor formation of volcanic margins. We estimate the conjugate width of this volcanic domain to be 18.25 km with intruded thicknesses of up to 10.0 km. Both the Fast and Slow models highlight the strain-rate dependence of the lower crust and its influence on the timing of continental breakup. Both models predict a formation of a volcanic passive margin, suggesting extension rate alone does independently or fully control margin morphology. However, similar to mantle potential temperature, extension rates clearly demonstrate an important influence on the overall margin magmatic character, with higher rates of extension favoring a narrower intruded volcanic domain and lower values of intrusive thicknesses.

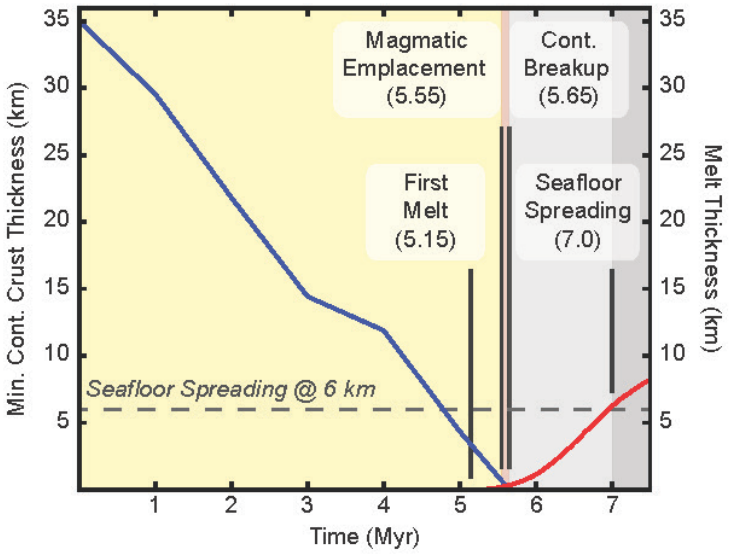

Figure 4.6 Fast model results.

Minimum continental crust thickness, blue, and melt thickness, red, since time since start of rifting for the Fast extension rate model. Magmatic emplacement begins prior to continental breakup. Volcanic intrusion of the continental crust and formation of a volcanic margin is estimated to occur during the time period outlined in red.

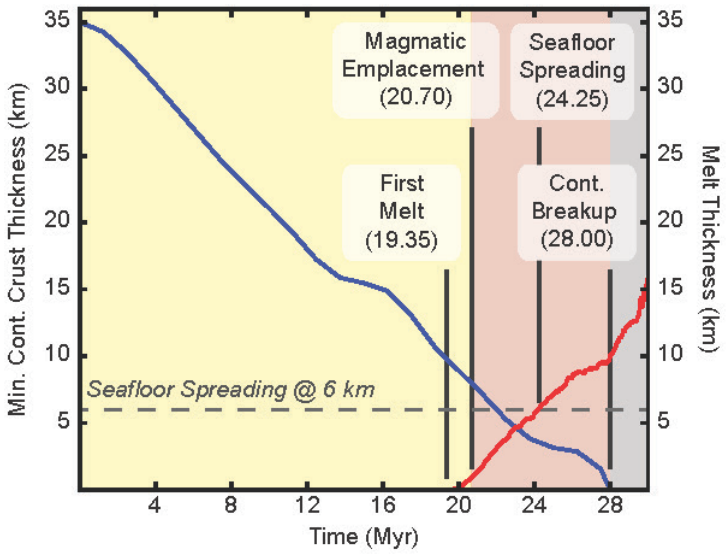

Figure 4.7 Slow model results

Minimum continental crust thickness, blue, and melt thickness, red, since time since start of rifting for the Slow extension rate model. Magmatic emplacement begins prior to continental breakup. Volcanic intrusion of the continental crust and formation of a volcanic margin is estimated to occur during the time period outlined in red.

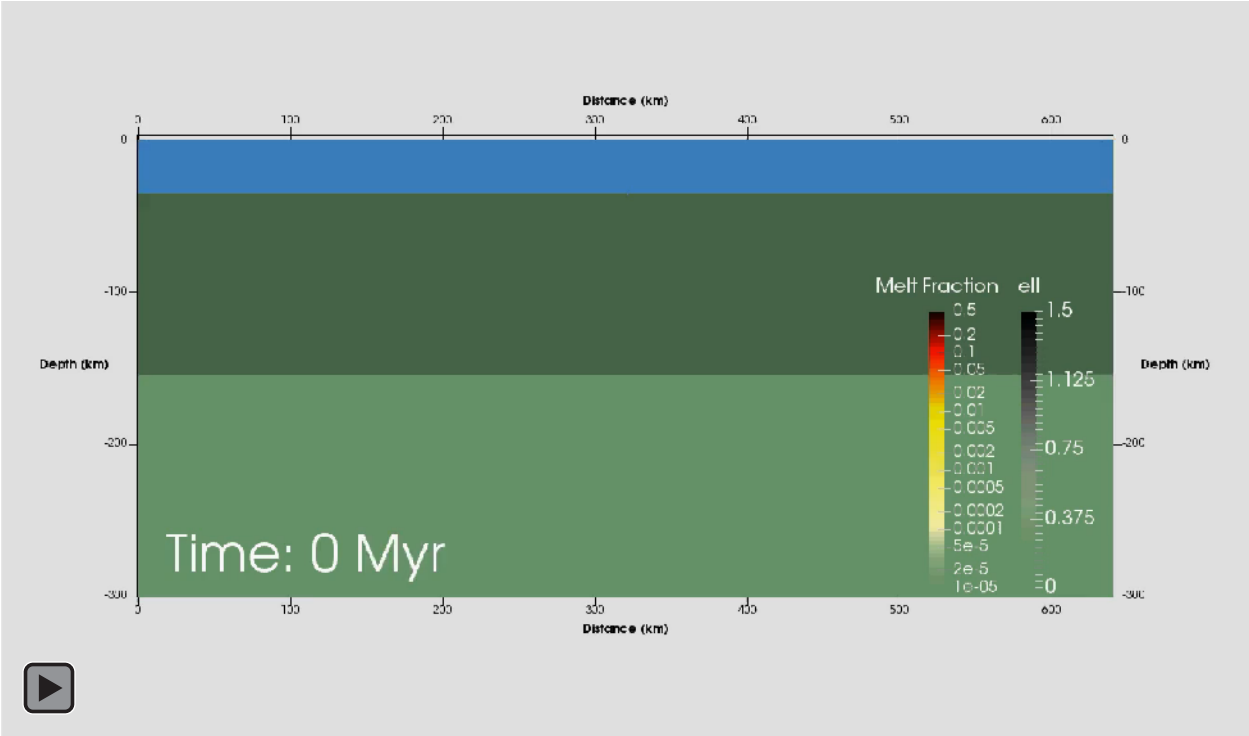

Animation 4.4 Fast model rifting simulation

Numerical simulation of continental rifting for the Fast extension rate model. Displayed variables are identical to those shown in Animation 4.1. In the Fast extension rate model, the first melt is generated at 5.15 Myrs, magmatic emplacement is estimated to begin at 5.55 Myrs, continental breakup occurs at 5.65 Myrs, and seafloor spreading melt thicknesses are reached at 7.00 Myrs. Because magmatic emplacement begins prior to continental breakup, the Fast extension rate model is predicted to generate a passive margin with a volcanic morphology.

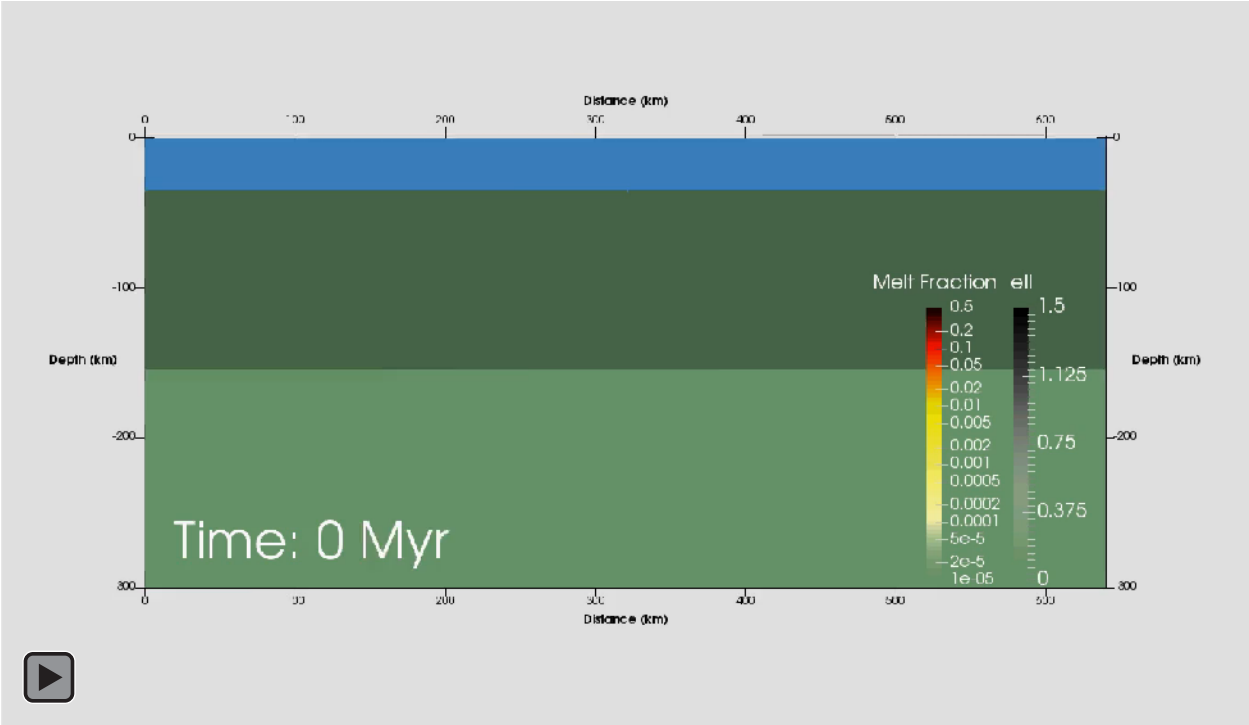

Animation 4.4 Slow model rifting simulation

Numerical simulation of continental rifting for the Slow extension rate model. Displayed variables are identical to those shown in Animation 4.1. In the Slow extension rate model, the first melt is generated at 19.35 Myrs, magmatic emplacement is estimated to begin at 20.70 Myrs, seafloor spreading melt thicknesses are reached at 24.25 Myrs, and continental breakup occurs at 28.00 Myrs. Because magmatic emplacement begins prior to continental breakup the Slow extension rate model is predicted to generate a passive margin with a volcanic morphology.

4.5.5 Lithosphere Geotherm

To evaluate manner in which lithosphere thermal structure influences margin morphology, we conduct and compare two experimental runs using a warmer Elevated (surface heat flow of 55 mW/m2) and a colder Depressed (surface heat flow 40 mW/m2) geotherm. In the Elevated model (Anim. 4.6), initial crustal deformation proceeds in a manner that strongly mimics the Base model. Melt production in the Elevated model begins at 10.10 Myrs (Fig. 4.8), slightly earlier than in the Base model, but at identical pressures (2.6 GPa). Magmatic emplacement is estimated to first occur at 11.20 Myrs. Continental breakup occurs later at 16.20 Myrs (Fig. 4.8). The 5.00 Myrs between first magmatic emplacement and continental breakup, is the third longest of all models, and suggests that an Elevated lithosphere geotherm demonstrate a clear volcanic margin. The protracted time between first magmatic emplacement and continental breakup is likely a result of warmer, ductile, lower crust accommodating the final stages of crustal thinning over a lengthier period. For the Elevated geotherm model, we estimate a volcanic domain of 25.0 km in width, with intrusive thicknesses up 10.9 km, for each conjugate margin.

The colder, Depressed geotherm model (Anim. 4.7) demonstrates a style of crustal faulting unique from the Base and Elevated models. Extension is accommodated on deeply penetrating faults that bound the H-Block and couple the crust and mantle. At 5.00 Myrs, following significant H-Block subsidence, a pair of initially shallow faults begin to form and localize deformation within the block. By 8.00 Myrs, these faults appear to have coupled to the upper mantle, and a new, antithetic, upper-crust fault is formed. Crustal thinning then progresses rapidly and reaches continental breakup by 10.70 Myrs (Fig. 4.9), the third fastest breakup of all model runs. Melt does not start being produced until 12.95 Myrs with magmatic emplacement estimated to first occur at 13.50 Myrs (Fig. 4.9). Seafloor spreading levels of melt production are delayed until 15.25 Myrs. The timing of

the all magmatic processes, including the first melting, magmatic emplacement, and establishment of seafloor spreading, are delayed in the Depressed model relative to the Base model. This delay in melt production likely result from the deeper LAB of the cold model, which forces the asthenosphere to upwell over a larger distance to intersect the solidus. Numerical model results indicate that during the 2.8 Myrs between continental breakup and first magmatic emplacement, extension is accommodated through exhumation of lithospheric mantle. Therefore, Depressed lithosphere geotherm conditions appear to favor the formation of passive margins with magma-poor morphology. We estimate that the exhumed mantle domain will be 14.0 km in width for each of the conjugate margins produced by the Depressed geotherm model. Melt thickness estimates (Fig. 4.9) suggest the development of a 22.75 km proto-oceanic domain outboard of each of these exhumed mantle domains. Given that Elevated and Depressed geotherms demonstrate a clear ability to influence and generate end-member morphologies, we interpret the lithospheric geotherm to be a significant control on passive continental extension.

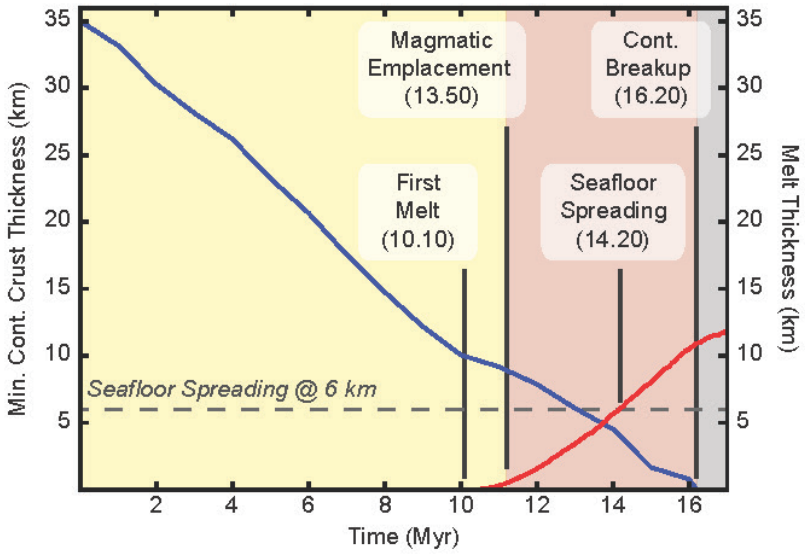

Figure 4.8 Results from Elevated geotherm model

Minimum continental crust thickness, blue, and melt thickness, red, since time since start of rifting for the Elevated lithosphere geotherm model. Magmatic emplacement begins prior to continental breakup. Volcanic intrusion of the continental crust and formation of a volcanic margin is estimated to occur during the time period outlined in red.

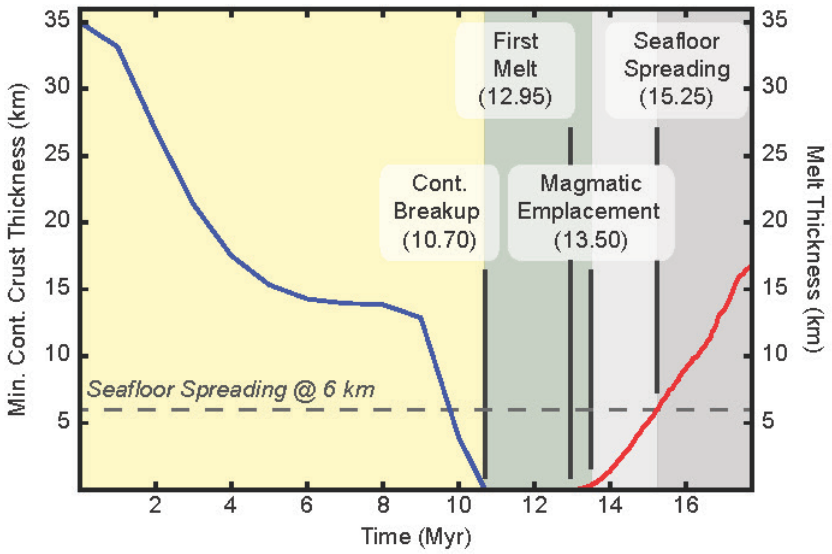

Figure 4.9 Results from Depressed geotherm model.

Minimum continental crust thickness, blue, and melt thickness, red, since time since start of rifting for the Depressed lithosphere geotherm model. Magmatic emplacement occurs after continental breakup. Lithospheric mantle exhumation and formation of a magma-poor margin is estimated to occur during the time period outlined in green.

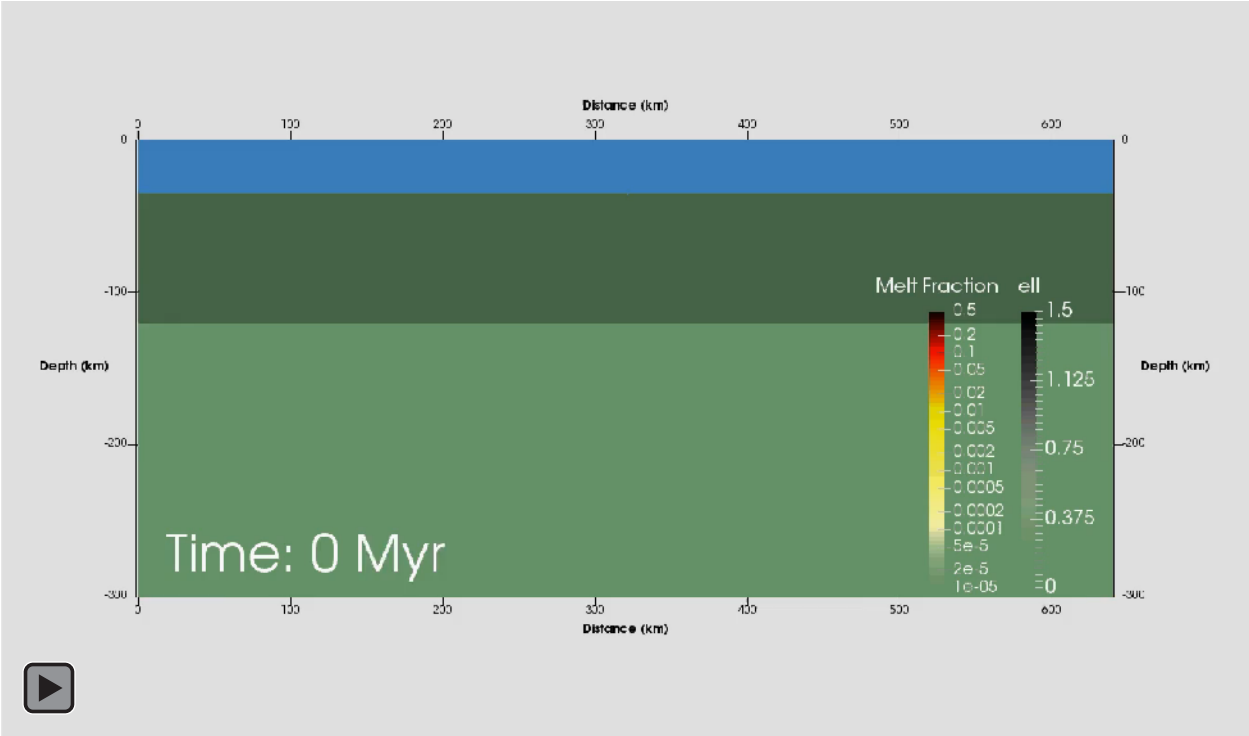

Animation 4.6 Elevated geotherm rifting simulation

Displayed variables are identical to those shown in Animation 4.1. In the Elevated geotherm model, the first melt is generated at 10.30 Myrs, magmatic emplacement is estimated to begin at 11.00 Myrs, seafloor spreading melt thicknesses are reached at 13.10 Myrs, and continental breakup occurs at 15.05 Myrs. Because magmatic emplacement begins prior to continental breakup, the Elevated geotherm model is predicted to generate a passive margin with a volcanic morphology.

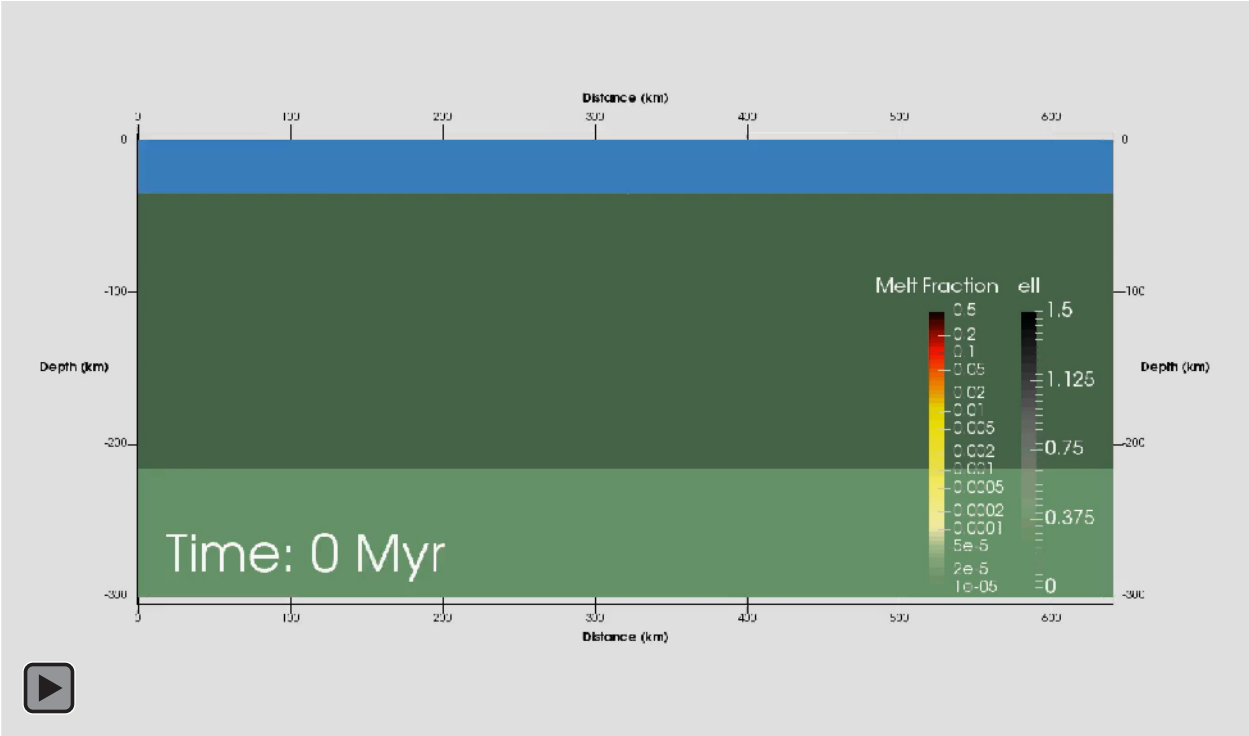

Animation 4.7 Depressed geotherm rifting simulation.

Displayed variables are identical to those shown in Animation 4.1. In the Depressed geotherm model, continental breakup occurs at 10.70 Myrs, the first melt is generated at 12.95 Myrs, magmatic emplacement is estimated to begin at 13.50 Myrs, and seafloor spreading melt thicknesses are reached at 15.25 Myrs. Because continental breakup occurs prior to any magmatic emplacement, the Depressed geotherm model is predicted to generate a passive margin with a magma-poor morphology.

4.5.6 Crustal Thickness

To investigate the influence of initial crustal thickness on margin morphology, we compare results from our Base model against an experiment with a Thin Crust of only 30 km (12 km upper; 18 km lower). In the Thin Crust model (Anim. 4.8), crustal deformation is dissimilar to the Base model and instead closely resembles the Depressed geotherm model. With a thinner lower crust, brittle faults penetrate deeply. Similar to the Depressed geotherm model, this acts to couple the crust and mantle and rapidly thin the crust. Continental breakup occurs rapidly (8.85 Myrs; Fig. 4.10), the second fastest time to breakup. Although first melting (8.70 Myrs; 2.6 GPa) precedes continental breakup, first magmatic emplacement (9.35 Myrs) postdates breakup (Fig. 4.10). The timing of continental breakup, first melt, magmatic emplacement, and establishment of seafloor spreading are all earlier in the Thin Crust model than in the Base model. This is likely related to the thinner domain of both crust and lithosphere in the model. Model results indicate that during the 0.5 Myrs between continental breakup and first magmatic emplacement, extension is accommodated via lithospheric mantle exhumation, and therefore the Thin Crust passive margin will demonstrate a magma-poor morphology. We estimate that this exhumed mantle will occupy a domain 2.5 km in width outboard of the limit of continental crust for each conjugate margin. Similar to the Depressed geotherm model, the Thin Crust model predicts a zone of proto-oceanic crust outboard of the exhumed lithospheric mantle. This proto-oceanic domain is estimated to be 13.75 km in width for each conjugate margin. Comparison of the varying morphologies of the Thin Crust and Base models indicate that crustal thickness acts as a significant control on the development of end-member passive margin morphologies.

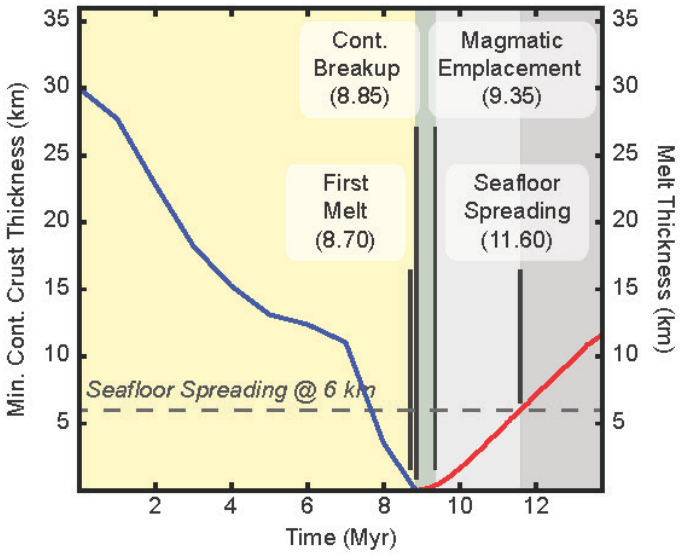

Figure 4.10 Results from the Thin crust model

Minimum continental crust thickness, blue, and melt thickness, red, since time since start of rifting for the Thin Crust model. Magmatic emplacement occurs after continental breakup. Lithospheric mantle exhumation and formation of a magma-poor margin is estimated to occur during the time period outlined in green.

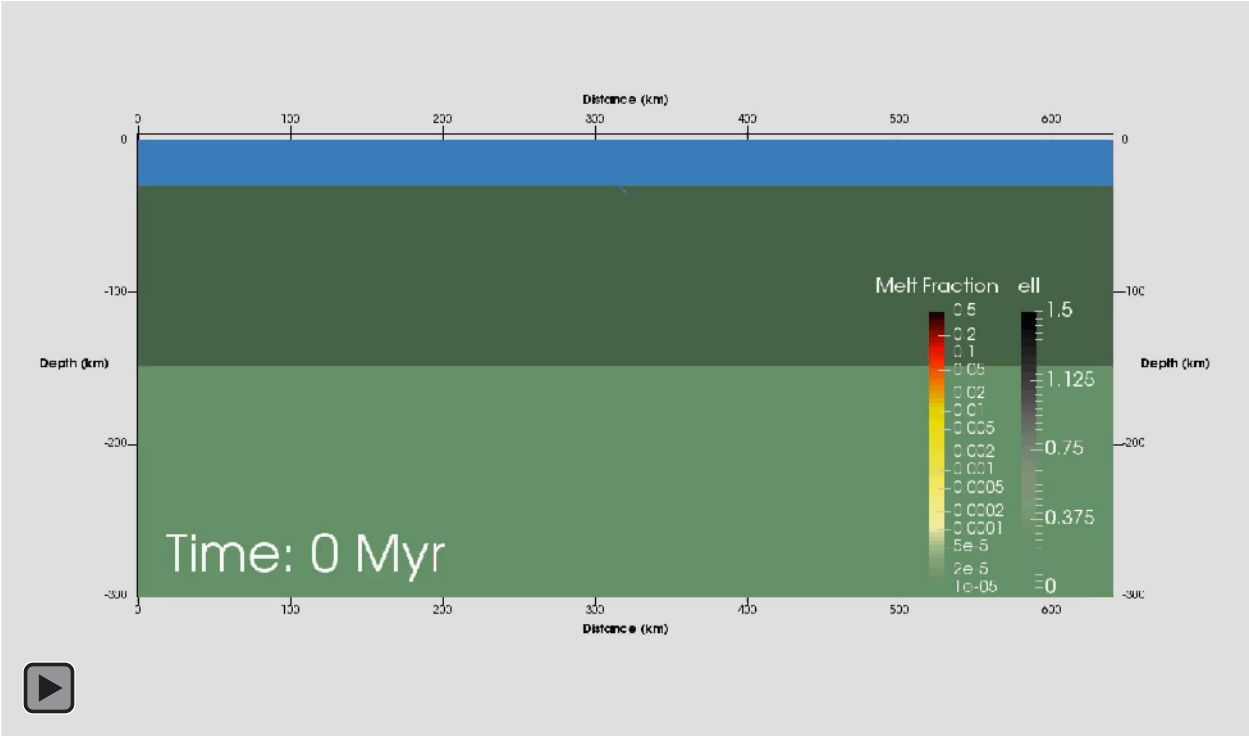

Animation 4.8 Thin Crust model rifting simulation

Displayed variables are identical to those shown in Animation 4.1. In the Thin Crust model, the first melt is generated at 8.70 Myrs, continental breakup occurs at 8.85 Myrs, magmatic emplacement is estimated to begin at 9.35 Myrs, and seafloor spreading melt thicknesses are reached at 11.60 Myrs. Because continental breakup occurs prior to any magmatic emplacement, the Thin Crust model is predicted to generate a passive margin with a magma-poor morphology.

4.5.7 Crustal Rheology

In order to investigate the potential influence of crustal rheology, we compare results from our Base model against an experiment in which a weaker Dry Quartz rheology was used for the continental crust. Crustal deformation observed in the Dry Quartz model (Anim. 4.9) differs from that observed in the Base model. Following initial H-Block formation, two sets of antithetic faults develop in the upper crust at 2.5 Myrs. While these faults confine brittle deformation in the upper crust, ductile deformation in the lower crust begins to reduce the angle of the H-Block bounding faults. Around 5.5 Myrs, a new fault forms in the upper crust outside of the H-Block and begins to accommodate delocalized deformation. At 8.5 Myrs, a new fault forms directly over the upwelling asthenosphere, couples the crust and upper mantle, and helps re-localize crustal deformation. The first melting occurs at 9.15 Myrs and magmatic emplacement follows closely at 9.85 Myrs (Fig. 4.11). Seafloor spreading rates of melt production are reached at 12.05 Myrs. Continental breakup occurs at 15.25 Myrs (Fig. 4.11) and likely assisted by the shallow, rapidly upwelling, asthenosphere. Results from the Dry Quartz run demonstrate the second longest period (5.4 Myrs) of magmatic emplacement prior to continental breakup. The intruded volcanic domain is estimated to be 27.0 km in width with intrusive thicknesses up to 15.8 km for each conjugate margin. As both the strong Base model and weak Dry Quartz models demonstrate volcanic morphologies, it does not appear that crustal rheology is a significant influence on formation of end-member passive margin morphologies. However, a stronger rheology does appear to favor a more limited volcanic domain width and thinner thickness of intrusive crust.

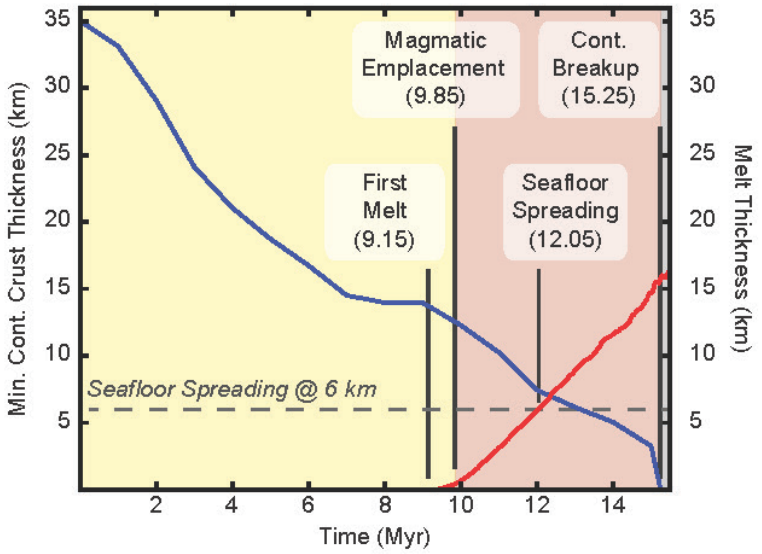

Figure 4.11 Results from the Dry Quartz model.

Minimum continental crust thickness, blue, and melt thickness, red, since time since start of rifting for the Dry Quartz crustal rheology model. Volcanic intrusion of the continental crust and formation of a volcanic margin is estimated to occur during the time period outlined in red.

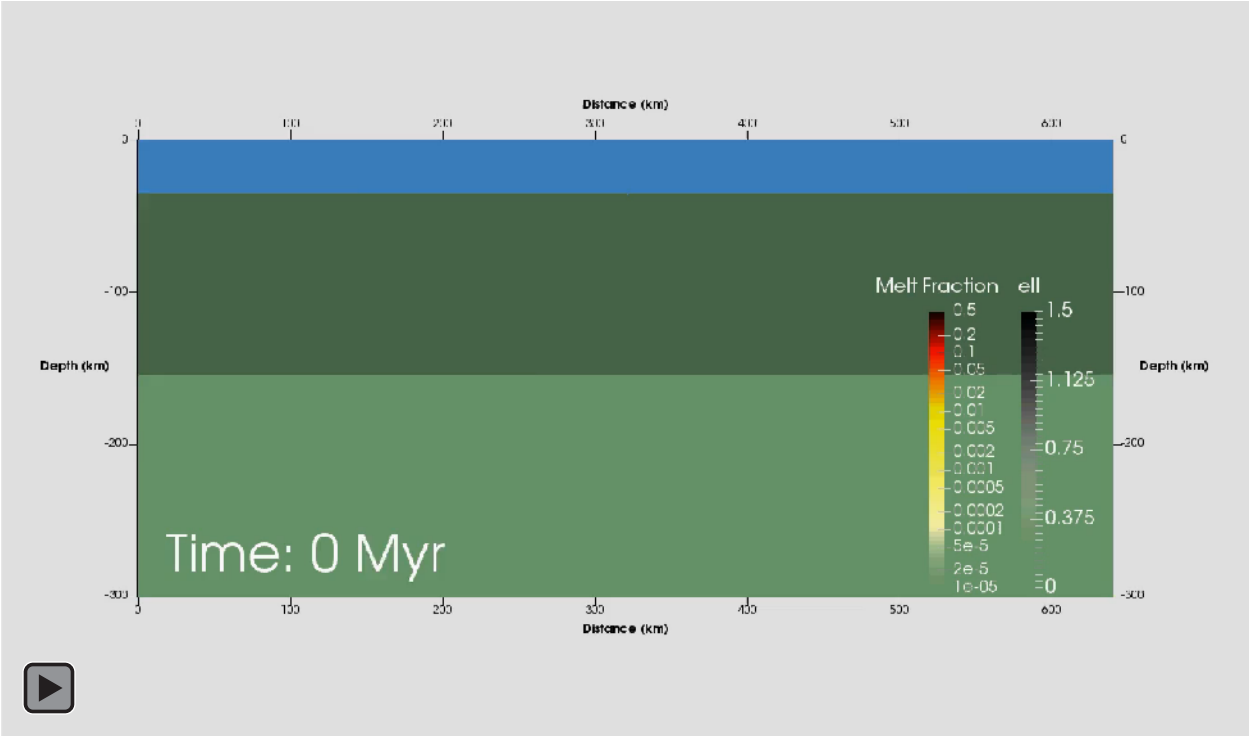

Animation 4.9 Dry Quartz rifting simulation

Numerical simulation of continental rifting for the Dry Quartz model. Displayed variables are identical to those shown in Animation 1. In the Dry Quartz model, the first melt is generated at 9.15 Myrs, magmatic emplacement is estimated to begin at 9.85 Myrs, seafloor spreading melt thicknesses are reached at 12.05 Myrs, and continental breakup occurs at 15.25 Myrs. Because magmatic emplacement begins prior to continental breakup, the Dry Quartz model is predicted to generate a passive margin with a volcanic morphology.

4.6. DISCUSSION

4.6.1 Overview

We estimate passive margin morphology (volcanic vs. magma-poor) by comparing the relative timing of continental breakup and first magmatic emplacement. Volcanic passive margins are interpreted to form in numerical simulations where magmatic emplacement begins before continental breakup. Magma-poor margins are interpreted to form in models where magmatic emplacement does not begin until after continental breakup. The timing of continental breakup, initial magmatic emplacement, and establishment of seafloor spreading, as well as estimates for the width of the various domains, and estimates of intrusive thickness are summarized for all models in Table 4.3. In Figure 4.12, melt thickness and first magmatic emplacement are graphically displayed relative to continental breakup for all model runs. Each investigated variable demonstrated some ability to influence the relative timing of magmatic emplacement to continental breakup and the magmatic character of the preserved passive margins. A spectrum of margin morphologies were produced with varying degrees of magmatism. Cooler lithosphere geotherms, thinner crust, faster extension, lower mantle potential temperature, and stronger crustal rheologies appear to favor formation of passive margins with more magma-poor affinities. Warmer lithosphere geotherms, thicker crust, slower extension, higher mantle potential temperatures, and weaker crust will tend to favor formation of more magmatic, volcanic passive margins. Similar to real world observations (Menzies, 2002; Skogseid, 2001), the majority (7/9) of our numerical experiments predict the formation of passive margins demonstrating some volcanic characteristics. Two of these volcanic models, the Fast extension and Low Tp cases, failed to reach melt production rates capable of sustaining seafloor spreading prior to continental breakup, suggesting formation of proto-oceanic crust seaward of the limit of continental crust. Only in two of our model

runs, the Depressed geotherm and Thin crust experiments, did the tectonic and magmatic processes develop in a manner conducive to the formation of a magma-poor morphology. Both of these magma-poor models have volcanic counterparts (i.e., Elevated geotherm; Base model/Thick Crust). Since multiple variables appear capable of reproducing both morphologies, we can conclude that no single variable is alone responsible for determining passive margin end-member morphology. However, even though multiple variables may influence passive margin morphology, our experiments indicate that some factors are relatively more influential than others. It is important to emphasize that our experiments only reflect the relative influence of each variable at the conditions modeled. At different conditions for the Base model, the relative effectiveness of each investigated variable will likely be modified.

Variable	**Model**	**Cont. Breakup (Myrs)**	**Magma Emplac. (Myrs)**	**Seafloor Spread. (Myrs)**	**Morphology**	**Intrusive Domain (km)**	**Exhumed Mantle Width (km)**	**Proto-ocean Width (km)**
Base	Base	15.05	11.00	13.10	Volcanic	20.25 (11.9)	0	0
Mantle Potential Temperature	Low Tp	13.05	11.55	14.65	Volcanic	7.5 (3.2)	0	8.0
	High Tp	12.20	9.10	10.60	Volcanic	15.5 (14.5)	0	0
Extension Rate	Fast	5.65	5.55	7.00	Volcanic	1.0 (0.3)	0	13.5
	Slow	28.00	20.70	24.25	Volcanic	18.25 (10)	0	0
Lithosphere Geotherm	Elevated	16.20	11.20	14.20	Volcanic	25 (10.9)	0	0
	Depressed	10.70	13.50	15.25	Magma-poor	0 (0)	14	22.75
Crustal Thickness	Thin	8.85	9.35	11.60	Magma-poor	0 (0)	2.5	13.75
Crustal Rheology	Dry Quartz	15.25	9.85	12.05	Volcanic	27 (15.8)	0	0

Table 4.3 Timing and summary of major rifting events in each experiment

4.6.2 Significant Influences: Lithosphere Geotherm & Crustal Thickness

In our experiments, the lithosphere geotherm appears to be the most significant variable in determining passive margin morphology. A warmer, elevated, lithosphere geotherm induces earlier magmatic emplacement relative to continental breakup, and tends to favor a volcanic morphology. Conversely, a cooler, depressed, lithosphere geotherm delays magmatic emplacement until after breakup and demonstrates a well-defined magma-poor morphology (Fig. 4.12). The lithosphere geotherm largely control passive margin morphology through two complementary influences on: (1) the strength of the continental crust and (2) the depth of the LAB. Cooler geotherms will tend to have both a brittle lower crust that favors rapid continent breakup, and an initially deep LAB that delays the onset of melting by distancing the asthenosphere from the solidus. Conversely, warmer geotherms will have ductile lower crust that can stymie rapid crustal thinning, as well as a shallow LAB that favors relatively earlier melting.

Crustal thickness appears to be a significant influence as well, with thinner crust favoring a magma-poor morphology and thicker crust favoring a volcanic morphology. Crustal thickness influences margin morphology by significantly altering both the style and rates of crustal thinning. When the crust is thin, brittle faulting is able to penetrate more deeply, and induce early continental breakup and mantle exhumation. The variation in margin morphology resulting crustal thickness experiments is not as extensive as the variability observed for the lithosphere geotherm experiments (Fig. 4.12). This leads us to suggest, that although a significant influence, crustal thickness is likely not as important as the lithosphere geotherm on determining margin morphology during continental extension.

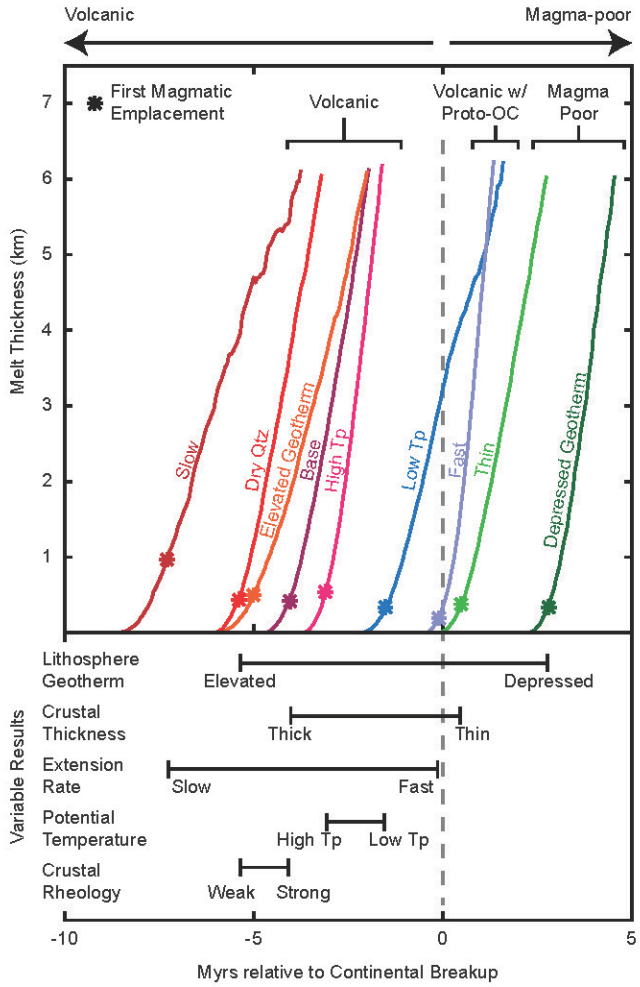

Figure 4.12. Modeling results summary

Melt thickness and onset of magmatic emplacement relative to the timing of continental breakup for all models. Volcanic margins, where some intrusion of continental crust likely occurred are indicated by magmatic emplacement asterisks to the left of the grey, dashed, continental breakup line. Magma-poor margins where post-breakup extension was accommodated by a period of lithospheric mantle exhumation are indicated by magmatic emplacement asterisks to the right of the continental breakup line. Models that have post-breakup melting rates below that necessary to form full thickness (6 km) oceanic crust, and therefore contain a proto-oceanic domain are indicated by melt thickness lines that cross the continental breakup line. Shown below the main graph, is the relative influence of each tested variable tested on model results. Variations in lithosphere geotherm and crustal thickness demonstrate a significant influence and are able to directly affect the resulting passive margin morphology. Extension rate and mantle potential temperature demonstrate a clear influence and may be potential important influencing factors. Crustal rheology does not appear to be a major influence on determining margin morphology.

4.6.3 Important Influences: Extension Rate & Mantle Potential Temperature

Despite not being able to produce both end-member morphologies, extension rates and mantle potential temperature exert an influence on the relative timing of magmatic emplacement and continental breakup, an important quality in determining the character of passive margins. Rapid extension appears to favor less pre-breakup volcanism, while slower extension appears to enhance the magnitude of pre-breakup volcanism. This result stems from the strain rate dependence of the ductile lower crust. In our rapidly extended model, the lower crust thins rapidly, leading to continental breakup while the asthenosphere is just beginning to upwell, and still at considerable depth. This deep asthenosphere is less productive and is ultimately responsible forming the proto-oceanic domain following breakup. Conversely, in the slowly extended model, the asthenosphere upwells quicker than the crust can thin, and ultimately forms one of the most well-defined volcanic margin of all experiments. It seems likely that under slightly altered initial conditions, variation of the extension rates would be able to demonstrate both types of end-member margin morphology.

Mantle Potential Temperatures offer a somewhat confounding picture of their influence on margin morphology. As expected, the potential temperatures demonstrates shallower melting, delayed magmatic emplacement, and lower rates of melt production. Higher potential temperature conditions demonstrates deeper, earlier melting and elevated melt production rates. Given the shallow depths the asthenosphere needs to reach to melt in the lower potential temperature model, we expect it capable of developing a magma-poor morphology under marginally different model conditions. Although the high potential temperature model demonstrates a more volcanic morphology than the low potential temperature model, the high temperature model does not appear to produce a volcanic domain as wide as the Base model. This is due to earlier continental breakup in the high

potential model (2.85 Myrs earlier). The highly sensitive nature of strain localization is responsible for differences in the location of faulting and timing of continental breakup in these models. Differences in the thermal and density properties of the asthenosphere affect isostatic forces and strain localization within the crust. It is worth noting that the high potential temperature model produces a thicker intrusive package than the Base model due to enhanced melt productivity. Variations in mantle potential temperatures demonstrate a clear influence on the depth, timing, and production rates of decompressive mantle melting and are therefore considered an important factor in determining passive margin morphology.

4.6.4 Likely Influence: Crustal Rheology

Differences in crustal rheology were able to produce observable changes in the relative timing of magmatic emplacement and continental breakup. Both the stronger dry-plagioclase and weaker dry-quartz experiments demonstrated timings of magmatic emplacement and continental breakup that indicated a volcanic morphology. Utilization of a dry quartz rheology slightly extended the timing of continental breakup, causing larger thicknesses of volcanic intrusives relative to the Base model. This result suggests weaker rheologies might favor development of more volcanic passive margins. Conversely, strong rheologies, such as dry-plagioclase, might assist in the development of magma-poor morphologies. It is likely that under altered model conditions, crustal rheology might be a more significant factor in determining passive margin morphology. However, for the experiments investigated in this work, crustal rheology did not demonstrate a clear ability to promote a diverse range of potential outcomes, and is therefore judged to be the relatively least important variable in these experiments.

4.7 CONCLUSIONS

We have conducted nine numerical experiments that investigate the influence of (1) lithosphere geotherm, (2) crustal thickness, (3) extension rate, (4) mantle potential temperature, and (5) crustal rheology on passive continental rifting and development of end-member margin morphologies. Experiment results indicate that all of these variables are capable of influencing continental rift development, and a spectrum of magmatic morphologies are produced. However, only two variables were found to independently and significantly alter the predicted end-member passive margin morphology. Out of all of the investigated variables, changes in the lithosphere geotherm demonstrated the most profound influence on passive margin morphology. Warmer geotherms encouraged development of volcanic margins and cooler geotherms clearly formed as magma-poor margins. Crustal thickness was identified as the second most influential variable. Changes in lower crustal thickness, as small as 5 km, were able to alter the final passive margin morphology. Thin crust appears to promote development of magma-poor margins, while thick crust encourages formation of volcanic margins. Although changes to extension rate and mantle potential temperature did not alter the development of margin morphology in these experiments, both variables demonstrated tendencies to influence margin morphology. Fast extension and low mantle potential temperatures appear to favor development of magma-poor characteristics. While slow extension rates and high mantle potential temperatures might favor formation of volcanic morphologies. Crustal rheology was found to be a more minor influence on margin morphology at the conditions investigated in these experiments, but might be more important at other initial and boundary conditions. Our results lead us to conclude that lithospheric thermal structure and crustal thickness are the most likely first order controls on passive margin morphological development. Extension rate and mantle potential temperatures likely influence this margin

development, but alone cannot account for the observed morphologic variations at passive continental margins.

Appendix

Supplementary available for download, along with a brief description, is listed below.

1. MagPicks.kmz - .kmz file of the magnetic identifications utilized in Chapter 2
2. dxypa.zip - zip file containing .dxypa shiptrack files used for ModMag modeling in Chapter 2
3. dat.zip - zip files containing .dat files for identifying magnetic anomalies in ModMag
4. IO_fz.kmz - .kmz files of seafloor fabric interpreted within the Indian Ocean
5. SomaliRidge.kmz - .kmz files of the abandoned spreading ridge interpreted in the Somali Basin
6. PlateModelAnimation.mp4 - .mp4 animation of the plate model developed in Chapter 2
7. SuppTable1_SeismicLine.csv - Table of the reflection seismic lines utilized in Chap. 3

References

Alibert, C., 1991. Mineralogy and geochemistry of a basalt from Site 738: Implications for the tectonic history of the southernmost part of the Kerguelen Plateau, Proc. Ocean Drill. Program Sci. Results, pp. 293-298.

Armitage, J.J., Collier, J.S., Minshull, T.A., 2010. The importance of rift history for volcanic margin formation. Nature 465, 913-917.

Aslanian, D., Moulin, M., Olivet, J.-L., Unternehr, P., Matias, L., Bache, F., Rabineau, M., Nouzé, H., Klingelheofer, F., Contrucci, I., 2009. Brazilian and African passive margins of the Central Segment of the South Atlantic Ocean: Kinematic constraints. Tectonophysics 468, 98-112.

Bastia, R., Radhakrishna, M., Srinivas, T., Nayak, S., Nathaniel, D., Biswal, T., 2010. Structural and tectonic interpretation of geophysical data along the Eastern Continental Margin of India with special reference to the deep water petroliferous basins. Journal of Asian Earth Sciences 39, 608-619.

Board, W., Frimmel, H., Armstrong, R., 2005. Pan-African tectonism in the western Maud Belt: P–T–t path for high-grade gneisses in the HU Sverdrupfjella, East Antarctica. Journal of Petrology 46, 671-699.

Boccaletti, M., Getaneh, A., Bonavia, F., 1991. THE MARDA FAULT: A REMNANT OF AN INCIPIENT ABORTED RIFT IN THE PALEO-AFRICAN ARABIAN PLATE. Journal of Petroleum Geology 14, 79-91.

Boillot, G., Beslier, M., Krawczyk, C., Rappin, D., Reston, T.J., 1995. The formation of passive margins: constraints from the crustal structure and segmentation of the deep Galicia margin, Spain. Geological Society, London, Special Publications 90, 71-91.

Boillot, G., Froitzheim, N., 2001. Non-volcanic rifted margins, continental break-up and the onset of sea-floor spreading: some outstanding questions. Geological Society, London, Special Publications 187, 9-30.

Borissova, I., Coffin, M.F., Charvis, P., Operto, S., 2003. Structure and development of a microcontinent: Elan Bank in the southern Indian Ocean. Geochemistry, Geophysics, Geosystems 4.

Bown, J.W., White, R.S., 1994. Variation with spreading rate of oceanic crustal thickness and geochemistry. Earth and Planetary Science Letters 121, 435-449.

Bown, J.W., White, R.S., 1995. Effect of finite extension rate on melt generation at rifted continental margins. Journal of Geophysical Research: Solid Earth 100, 18011-18029.

Boyden, J.A., Müller, R.D., Gurnis, M., Torsvik, T.H., Clark, J.A., Turner, M., Ivey-Law, H., Watson, R.J., Cannon, J.S., 2011. Next-generation plate-tectonic reconstructions using GPlates.

Brune, S., 2016. Rifts and rifted margins: A review of geodynamic processes and natural hazards. Plate Boundaries and Natural Hazards 219, 13.

Buck, W.R., 1991. Modes of continental lithospheric extension. Journal of Geophysical Research 96, 20161-20178.

Bürgmann, R., Dresen, G., 2008. Rheology of the lower crust and upper mantle: Evidence from rock mechanics, geodesy, and field observations. Annual Review of Earth and Planetary Sciences 36, 531.

Cande, S.C., Larson, R.L., LaBrecque, J.L., 1978. Magnetic lineations in the Pacific Jurassic quiet zone. Earth and Planetary Science Letters 41, 434-440.

Carbotte, S.M., Scheirer, D.S., 2004. Variability of Ocean Crustal Structure Created Along the Global Midocean Ridge, In: Davis, E.E., Elderfield, H. (Eds.), Hydrogeology of the Oceanic Lithosphere. Cambridge University Press, p. 59.

Chiappini, M., von Frese, R.R., 1999. Advances in Antarctic geomagnetism. Annali di Geofizica 42.

Christensen, N.I., Mooney, W.D., 1995. Seismic velocity structure and composition of the continental crust: A global view. Journal of Geophysical Research: Solid Earth 100, 9761-9788.

Cochran, J.R., 1988. Somali Basin, Chain Ridge, and origin of the Northern Somali Basin gravity and geoid low. Journal of Geophysical Research: Solid Earth 93, 11985-12008.

Coffin, M.F., Eldholm, O., 1992. Volcanism and continental break-up: a global compilation of large igneous provinces. Geological Society, London, Special Publications 68, 17-30.

Coffin, M.F., Eldholm, O., 1993. Scratching the surface: Estimating dimensions of large igneous provinces. Geology 21, 515-518.

Coffin, M.F., Eldholm, O., 1994. Large igneous provinces: crustal structure, dimensions, and external consequences. Reviews of Geophysics 32, 1-36.

Coffin, M.F., Pringle, M., Duncan, R., Gladczenko, T., Storey, M., Müller, R., Gahagan, L., 2002. Kerguelen hotspot magma output since 130 Ma. Journal of Petrology 43, 1121-1137.

Collins, A.S., Clark, C., Plavsa, D., 2014. Peninsular India in Gondwana: the tectonothermal evolution of the Southern Granulite Terrain and its Gondwanan counterparts. Gondwana Research 25, 190-203.

Collins, A.S., Pisarevsky, S.A., 2005. Amalgamating eastern Gondwana: the evolution of the Circum-Indian Orogens. Earth-Science Reviews 71, 229-270.

Contreras, J., Zühlke, R., Bowman, S., Bechstädt, T., 2010. Seismic stratigraphy and subsidence analysis of the southern Brazilian margin (Campos, Santos and Pelotas basins). Marine and Petroleum Geology 27, 1952-1980.

Contrucci, I., Matias, L., Moulin, M., Géli, L., Klingelhofer, F., Nouzé, H., Aslanian, D., Olivet, J.-L., Réhault, J.-P., Sibuet, J.-C., 2004. Deep structure of the West African continental margin (Congo, Zaïre, Angola), between 5 S and 8 S, from reflection/refraction seismics and gravity data. Geophysical Journal International 158, 529-553.

Cooray, P., 1994. The Precambrian of Sri Lanka: a historical review. Precambrian Research 66, 3-18.

Davis, J.K., Lawver, L.A., Norton, I.O., Gahagan, L.M., 2016. New Somali Basin magnetic anomalies and a plate model for the early Indian Ocean. Gondwana Research 34, 16-28.

Dean, S., Minshull, T., Whitmarsh, R., Louden, K., 2000. Deep structure of the ocean-continent transition in the southern Iberia Abyssal Plain from seismic refraction profiles: The IAM-9 transect at 40 20′ N. Journal of Geophysical Research: Solid Earth 105, 5859-5885.

Dick, H.J., Lin, J., Schouten, H., 2003. An ultraslow-spreading class of ocean ridge. Nature 426, 405-412.

Direen, N., Borissova, I., Stagg, H., Colwell, J., Symonds, P., 2007. Nature of the continent–ocean transition zone along the southern Australian continental margin: a comparison of the Naturaliste Plateau, SW Australia, and the central Great

Australian Bight sectors. Geological Society, London, Special Publications 282, 239-263.

Direen, N.G., Stagg, H.M., Symonds, P.A., Colwell, J.B., 2011. Dominant symmetry of a conjugate southern Australian and East Antarctic magma-poor rifted margin segment. Geochemistry, Geophysics, Geosystems 12.

Duncan, R.A., 2002. A time frame for construction of the Kerguelen Plateau and Broken Ridge. Journal of Petrology 43, 1109-1119.

Eagles, G., König, M., 2008. A model of plate kinematics in Gondwana breakup. Geophysical Journal International 173, 703-717.

Eldholm, O., Gladczenko, T., Skogseid, J., Planke, S., 2000. Atlantic volcanic margins: a comparative study. Geological Society, London, Special Publications 167, 411-428.

Eldholm, O., Grue, K., 1994. North Atlantic volcanic margins: dimensions and production rates. Journal of Geophysical Research: Solid Earth 99, 2955-2968.

England, P., 1983. Constraints on extension of continental lithosphere. Journal of Geophysical Research: Solid Earth 88, 1145-1152.

Espurt, N., Callot, J.P., Roure, F., Totterdell, J.M., Struckmeyer, H.I., Vially, R., 2012. Transition from symmetry to asymmetry during continental rifting: an example from the Bight Basin–Terre Adélie (Australian and Antarctic conjugate margins). Terra Nova 24, 167-180.

Franke, D., 2013. Rifting, lithosphere breakup and volcanism: Comparison of magma-poor and volcanic rifted margins. Marine and Petroleum Geology 43, 63-87.

Frey, F.A., Coffin, M., Wallace, P., Weis, D., Zhao, X., Wise, S., Wähnert, V., Teagle, D., Saccocia, P., Reusch, D., 2000. Origin and evolution of a submarine large igneous province: the Kerguelen Plateau and Broken Ridge, southern Indian Ocean. Earth and Planetary Science Letters 176, 73-89.

Frey, F.A., McNaughton, N.J., Nelson, D.R., Duncan, R.A., 1996. Petrogenesis of the Bunbury Basalt, Western Australia: interaction between the Kerguelen plume and Gondwana lithosphere? Earth and Planetary Science Letters 144, 163-183.

Fritz, H., Abdelsalam, M., Ali, K., Bingen, B., Collins, A., Fowler, A., Ghebreab, W., Hauzenberger, C., Johnson, P., Kusky, T., 2013. Orogen styles in the East African

Orogen: a review of the Neoproterozoic to Cambrian tectonic evolution. Journal of African Earth Sciences 86, 65-106.

Gaina, C., Müller, R., Brown, B., Ishihara, T., 2003. Microcontinent formation around Australia. Geological Society of America Special Papers 372, 405-416.

Gaina, C., Müller, R.D., Brown, B., Ishihara, T., Ivanov, S., 2007. Breakup and early seafloor spreading between India and Antarctica. Geophysical Journal International 170, 151-169.

Gee, J.S., Kent, D.V., 2007. Source of oceanic magnetic anomalies and the geomagnetic polarity time scale.

Geoffroy, L., 2005. Volcanic passive margins. Comptes Rendus Geoscience 337, 1395-1408.

Gibbons, A.D., Barckhausen, U., den Bogaard, P., Hoernle, K., Werner, R., Whittaker, J.M., Müller, R.D., 2012. Constraining the Jurassic extent of Greater India: Tectonic evolution of the West Australian margin. Geochemistry, Geophysics, Geosystems 13.

Gibbons, A.D., Whittaker, J.M., Müller, R.D., 2013. The breakup of East Gondwana: assimilating constraints from Cretaceous ocean basins around India into a best-fit tectonic model. Journal of Geophysical Research: Solid Earth 118, 808-822.

Gillard, M., Autin, J., Manatschal, G., Sauter, D., Munschy, M., Schaming, M., 2015. Tectonomagmatic evolution of the final stages of rifting along the deep conjugate Australian-Antarctic magma-poor rifted margins: Constraints from seismic observations. Tectonics 34, 753-783.

Gillard, M., Manatschal, G., Autin, J., 2016. How can asymmetric detachment faults generate symmetric Ocean Continent Transitions? Terra Nova 28, 27-34.

Gohl, K., Leitchenkov, G., Parsiegla, N., Ehlers, B.-M., Kopsch, C., Damaske, D., Guseva, Y., Gandyukhin, V., 2007. Crustal types and continent-ocean boundaries between the Kerguelen Plateau and Prydz Bay, East Antarctica. Antarctica: A Keystone in a Changing World. Proc. 10th ISAES, USGS Open-File Report 1047.

Golynsky, A., 2007. Magnetic anomalies in East Antarctica and surrounding regions: a window on major tectonic provinces and their boundaries. Proceedings of the 10th ISAES: USGS Open-File Report 1047.

Golynsky, A., Alyavdin, S., Masolov, V., Tscherinov, A., Volnukhin, V., 2002. The composite magnetic anomaly map of the East Antarctic. Tectonophysics 347, 109-120.

Golynsky, A., Ivanov, S., Kazankov, A.J., Jokat, W., Masolov, V., von Frese, R., Group, A.W., 2013. New continental margin magnetic anomalies of East Antarctica. Tectonophysics 585, 172-184.

Hanson, R.E., Crowley, J.L., Bowring, S.A., Ramezani, J., Gose, W.A., Dalziel, I.W., Pancake, J.A., Seidel, E.K., Blenkinsop, T.G., Mukwakwami, J., 2004. Coeval large-scale magmatism in the Kalahari and Laurentian cratons during Rodinia assembly. Science 304, 1126-1129.

Hasterok, D., Chapman, D., 2011. Heat production and geotherms for the continental lithosphere. Earth and Planetary Science Letters 307, 59-70.

Hayes, D.E., Nissen, S.S., 2005. The South China sea margins: Implications for rifting contrasts. Earth and Planetary Science Letters 237, 601-616.

Heirtzler, J.R., Burroughs, R.H., 1971. Madagascar's paleoposition: new data from the Mozambique Channel. Science 174, 488-490.

Holbrook, W., Kelemen, P., 1993. Large igneous province on the US Atlantic margin and implications for magmatism. Nature 364, 433-436.

Holbrook, W.S., Reiter, E., Purdy, G., Sawyer, D., Stoffa, P., Austin, J., Oh, J., Makris, J., 1994. Deep structure of the US Atlantic continental margin, offshore South Carolina, from coincident ocean bottom and multichannel seismic data. Journal of Geophysical Research: Solid Earth 99, 9155-9178.

Hopper, J., Funck, T., Tucholke, B., 2007. Structure of the Flemish Cap margin, Newfoundland: insights into mantle and crustal processes during continental breakup. Geological Society, London, Special Publications 282, 47-61.

Hopper, J.R., Dahl-Jensen, T., Holbrook, W.S., Larsen, H.C., Lizarralde, D., Korenaga, J., Kent, G.M., Kelemen, P.B., 2003. Structure of the SE Greenland margin from seismic reflection and refraction data: Implications for nascent spreading center subsidence and asymmetric crustal accretion during North Atlantic opening. Journal of Geophysical Research: Solid Earth 108.

Hopper, J.R., Mutter, J.C., Larson, R.L., Mutter, C.Z., 1992. Magmatism and rift margin evolution: Evidence from northwest Australia. Geology 20, 853-857.

Huismans, R.S., Beaumont, C., 2002. Asymmetric lithospheric extension: The role of frictional plastic strain softening inferred from numerical experiments. Geology 30, 211-214.

Huismans, R.S., Beaumont, C., 2014. Rifted continental margins: the case for depth-dependent extension. Earth and Planetary Science Letters 407, 148-162.

Huismans, R.S., Buiter, S.J., Beaumont, C., 2005. Effect of plastic-viscous layering and strain softening on mode selection during lithospheric extension. Journal of Geophysical Research: Solid Earth 110.

Ingle, S., Weis, D., Frey, F., 2002. Indian continental crust recovered from Elan Bank, Kerguelen plateau (ODP Leg 183, site 1137). Journal of Petrology 43, 1241-1257.

Ishwar-Kumar, C., Windley, B., Horie, K., Kato, T., Hokada, T., Itaya, T., Yagi, K., Gouzu, C., Sajeev, K., 2013. A Rodinian suture in western India: New insights on India-Madagascar correlations. Precambrian Research 236, 227-251.

Jokat, W., Nogi, Y., Leinweber, V., 2010. New aeromagnetic data from the western Enderby Basin and consequences for Antarctic-India break-up. Geophysical Research Letters 37.

Jourdan, F., Féraud, G., Bertrand, H., Watkeys, M., 2007. From flood basalts to the inception of oceanization: Example from the 40Ar/39Ar high-resolution picture of the Karoo large igneous province. Geochemistry, Geophysics, Geosystems 8.

Jourdan, F., Féraud, G., Bertrand, H., Watkeys, M., Renne, P., 2008. The 40Ar/39Ar ages of the sill complex of the Karoo large igneous province: Implications for the Pliensbachian-Toarcian climate change. Geochemistry, Geophysics, Geosystems 9.

Karner, G.D., Manatschal, G., Pinheiro, L., 2007. Imaging, mapping and modelling continental lithosphere extension and breakup: an introduction. Geological Society, London, Special Publications 282, 1-8.

Katz, R.F., Spiegelman, M., Langmuir, C.H., 2003. A new parameterization of hydrous mantle melting. Geochemistry, Geophysics, Geosystems 4.

König, M., Jokat, W., 2010. Advanced insights into magmatism and volcanism of the Mozambique Ridge and Mozambique Basin in the view of new potential field data. Geophysical Journal International 180, 158-180.

Kusznir, N., Park, R., 1987. The extensional strength of the continental lithosphere: its dependence on geothermal gradient, and crustal composition and thickness. Geological Society, London, Special Publications 28, 35-52.

Larson, R.L., Mutter, J.C., Diebold, J.B., Carpenter, G.B., Symonds, P., 1979. Cuvier Basin: a product of ocean crust formation by Early Cretaceous rifting off Western Australia. Earth and Planetary Science Letters 45, 105-114.

Lavier, L.L., Buck, W.R., 2002. Half graben versus large-offset low-angle normal fault: Importance of keeping cool during normal faulting. Journal of Geophysical Research: Solid Earth 107.

Lavier, L.L., Buck, W.R., Poliakov, A.N., 2000. Factors controlling normal fault offset in an ideal brittle layer. Journal of Geophysical Research: Solid Earth 105, 431-423.

Lavier, L.L., Manatschal, G., 2006. A mechanism to thin the continental lithosphere at magma-poor margins. Nature 440, 324-328.

Lawver, L.A., Gahagan, L.M., Dalziel, I.W., 1998. A tight fit-early Mesozoic Gondwana, a plate reconstruction perspective. Memoirs of National Institute of Polar Research. Special issue 53, 214-229.

Le Pichon, X., Heirtzler, J.R., 1968. Magnetic anomalies in the Indian Ocean and sea-floor spreading. Journal of Geophysical Research 73, 2101-2117.

Leinweber, V.T., Jokat, W., 2012. The Jurassic history of the Africa–Antarctica corridor—new constraints from magnetic data on the conjugate continental margins. Tectonophysics 530, 87-101.

Leitchenkov, G., Guseva, J., Gandyukhin, V., Grikurov, G., Kristoffersen, Y., Sand, M., Golynsky, A., Aleshkova, N., 2008. Crustal structure and tectonic provinces of the Riiser-Larsen Sea area (East Antarctica): results of geophysical studies. Marine Geophysical Researches 29, 135-158.

Leitchenkov, G., Guseva, Y.B., Gandyukhin, V., Ivanov, S., Safonova, L., 2014. Structure of the Earth's crust and tectonic evolution history of the Southern Indian Ocean (Antarctica). Geotectonics 48, 5.

Lester, R., Van Avendonk, H.J., McIntosh, K., Lavier, L., Liu, C.S., Wang, T., Wu, F., 2014. Rifting and magmatism in the northeastern South China Sea from wide-angle tomography and seismic reflection imaging. Journal of Geophysical Research: Solid Earth 119, 2305-2323.

Mahoney, J.J., Coffin, M.F., 1997. Large igneous provinces: continental, oceanic, and planetary flood volcanism. American Geophysical Union.

Manatschal, G., 2004. New models for evolution of magma-poor rifted margins based on a review of data and concepts from West Iberia and the Alps. International Journal of Earth Sciences 93, 432-466.

Manatschal, G., Bernoulli, D., 1999. Architecture and tectonic evolution of nonvolcanic margins: Present-day Galicia and ancient Adria. Tectonics 18, 1099-1119.

Markl, R.G., 1974. Evidence for the breakup of eastern Gondwanaland by the Early Cretaceous. Nature 251, 196-200.

Marks, K., Tikku, A., 2001. Cretaceous reconstructions of East Antarctica, Africa and Madagascar. Earth and Planetary Science Letters 186, 479-495.

McElhinny, M., 1970. Formation of the Indian Ocean. Nature 228, 977-979.

McIntosh, K., Lavier, L., van Avendonk, H., Lester, R., Eakin, D., Liu, C.-S., 2014. Crustal structure and inferred rifting processes in the northeast South China Sea. Marine and Petroleum Geology 58, 612-626.

McKenzie, D., Bickle, M., 1988. The volume and composition of melt generated by extension of the lithosphere. Journal of Petrology 29, 625-679.

McKenzie, D., Sclater, J.G., 1971. The evolution of the Indian Ocean since the Late Cretaceous. Geophysical Journal International 24, 437-528.

Mendel, V., Munschy, M., Sauter, D., 2005. MODMAG, a MATLAB program to model marine magnetic anomalies. Computers & geosciences 31, 589-597.

Menzies, M.A., 2002. Volcanic rifted margins. Geological Society of America.

Mjelde, R., Digranes, P., Shimamura, H., Shiobara, H., Kodaira, S., Brekke, H., Egebjerg, T., Sørenes, N., Thorbjørnsen, S., 1998. Crustal structure of the northern part of the Vøring Basin, mid-Norway margin, from wide-angle seismic and gravity data. Tectonophysics 293, 175-205.

Mjelde, R., Kasahara, J., Shimamura, H., Kamimura, A., Kanazawa, T., Kodaira, S., Raum, T., Shiobara, H., 2002. Lower crustal seismic velocity-anomalies; magmatic underplating or serpentinized peridotite? Evidence from the Vøring Margin, NE Atlantic. Marine Geophysical Researches 23, 169-183.

Mjelde, R., Kodaira, S., Shimamura, H., Kanazawa, T., Shiobara, H., Berg, E., Riise, O., 1997. Crustal structure of the central part of the Vøring Basin, mid-Norway margin, from ocean bottom seismographs. Tectonophysics 277, 235-257.

Mohriak, W., Mello, M., Dewey, J., Maxwell, J., 1990. Petroleum geology of the Campos Basin, offshore Brazil. Geological Society, London, Special Publications 50, 119-141.

Mohriak, W., Nemčok, M., Enciso, G., 2008. South Atlantic divergent margin evolution: rift-border uplift and salt tectonics in the basins of SE Brazil. Geological Society, London, Special Publications 294, 365-398.

Mutter, J.C., Hegarty, K.A., Cande, S.C., Weissel, J.K., 1985. Breakup between Australia and Antarctica: a brief review in the light of new data. Tectonophysics 114, 255-279.

Mutter, J.C., Talwani, M., Stoffa, P.L., 1982. Origin of seaward-dipping reflectors in oceanic crust off the Norwegian margin by "subaerial sea-floor spreading". Geology 10, 353-357.

Nemcok, M., Henk, A., Allen, R., Sikora, P., Stuart, C., 2012. Continental break-up along strike-slip fault zones; observations from the Equatorial Atlantic: Geological Society. London, Special Publications Online, First published March 27, 2012.

Niu, X., Ruan, A., Li, J., Minshull, T., Sauter, D., Wu, Z., Qiu, X., Zhao, M., Chen, Y.J., Singh, S., 2015. Along-axis variation in crustal thickness at the ultraslow spreading Southwest Indian Ridge (50° E) from a wide-angle seismic experiment. Geochemistry, Geophysics, Geosystems 16, 468-485.

Nogi, Y., Nishi, K., Seama, N., Fukuda, Y., 2004. An interpretation of the seafloor spreading history of the West Enderby Basin between initial breakup of Gondwana and anomaly C34. Marine Geophysical Research 25, 221-231.

Norton, I., Sclater, J., 1979. A model for the evolution of the Indian Ocean and the breakup of Gondwanaland. Journal of Geophysical Research: Solid Earth 84, 6803-6830.

O'brien, P., Stagg, H., 2007. Tectonic elements of the continental margin of East Antarctica, 38–164ºE: in. US Geological Survey.

Operto, S., Charvis, P., 1996. Deep structure of the southern Kerguelen Plateau (southern Indian Ocean) from ocean bottom seismometer wide-angle seismic data. Journal of Geophysical Research: Solid Earth 101, 25077-25103.

Pérez-Gussinyé, M., Reston, T., Morgan, J.P., 2001. Serpentinization and magmatism during extension at non-volcanic margins: the effect of initial lithospheric structure. Geological Society, London, Special Publications 187, 551-576.

Pérez-Gussinyé, M., Reston, T.J., 2001. Rheological evolution during extension at nonvolcanic rifted margins: onset of serpentinization and development of detachments leading to continental breakup. Journal of Geophysical Research: Solid Earth 106, 3961-3975.

Péron-Pinvidic, G., Manatschal, G., 2009. The final rifting evolution at deep magma-poor passive margins from Iberia-Newfoundland: a new point of view. International Journal of Earth Sciences 98, 1581-1597.

Phipps Morgan, J., Parmentier, E., Lin, J., 1987. Mechanisms for the origin of mid-ocean ridge axial topography: Implications for the thermal and mechanical structure of accreting plate boundaries. Journal of Geophysical Research: Solid Earth 92, 12823-12836.

Planke, S., Symonds, P.A., Alvestad, E., Skogseid, J., 2000. Seismic volcanostratigraphy of large-volume basaltic extrusive complexes on rifted margins. Journal of Geophysical Research: Solid Earth 105, 19335-19351.

Poliakov, A., Podladchikov, Y., Talbot, C., 1993. Initiation of salt diapirs with frictional overburdens: numerical experiments. Tectonophysics 228, 199-210.

Powell, C.M., Roots, S., Veevers, J., 1988. Pre-breakup continental extension in East Gondwanaland and the early opening of the eastern Indian Ocean. Tectonophysics 155, 261-283.

Rabinowitz, P.D., Coffin, M.F., Falvey, D., 1983. The separation of Madagascar and Africa. Science 220, 67-69.

Radhakrishna, M., Twinkle, D., Nayak, S., Bastia, R., Rao, G.S., 2012. Crustal structure and rift architecture across the Krishna–Godavari basin in the central Eastern Continental Margin of India based on analysis of gravity and seismic data. Marine and Petroleum Geology 37, 129-146.

Reeves, C., 2014. The position of Madagascar within Gondwana and its movements during Gondwana dispersal. Journal of African Earth Sciences 94, 45-57.

Reeves, C., De Wit, M., 2000. Making ends meet in Gondwana: retracing the transforms of the Indian Ocean and reconnecting continental shear zones. Terra Nova 12, 272-280.

Reeves, C., Sahu, B., De Wit, M., 2002. A re-examination of the paleo-position of Africa's eastern neighbours in Gondwana. Journal of African Earth Sciences 34, 101-108.

Reston, T., 2007. Extension discrepancy at North Atlantic nonvolcanic rifted margins: Depth-dependent stretching or unrecognized faulting? Geology 35, 367-370.

Royer, J.-Y., Coffin, M.F., 1988. 50. JURASSIC TO EOCENE PLATE TECTONIC RECONSTRUCTIONS IN THE KERGUELEN PLATEAU REGION1, Proceedings of the Ocean Drilling Program: Scientific results. The Program, p. 917.

Sandwell, D.T., Müller, R.D., Smith, W.H., Garcia, E., Francis, R., 2014. New global marine gravity model from CryoSat-2 and Jason-1 reveals buried tectonic structure. Science 346, 65-67.

Savva, D., Meresse, F., Pubellier, M., Chamot-Rooke, N., Lavier, L., Po, K.W., Franke, D., Steuer, S., Sapin, F., Auxietre, J., 2013. Seismic evidence of hyper-stretched crust and mantle exhumation offshore Vietnam. Tectonophysics 608, 72-83.

Schmeling, H., 2006. A model of episodic melt extraction for plumes. Journal of Geophysical Research: Solid Earth 111.

Sclater, J.G., Fisher, R.L., 1974. Evolution of the east: Central Indian Ocean, with emphasis on the tectonic setting of the Ninetyeast Ridge. Geological Society of America Bulletin 85, 683-702.

Segoufin, J., 1978. Anomalies magnetiques mesozoiques dans le bassin de Mozambique. CR Acad. Sci. Paris 287, 109-112.

Segoufin, J., Patriat, P., 1980. Existence d'anomalies mésozoïques dans le bassin de Somalie. Implications pour les relations Afrique-Antarctique-Madagascar. CR Acad. Sci. Paris 291, 85-88.

Sengör, A., Burke, K., 1978. Relative timing of rifting and volcanism on Earth and its tectonic implications. Geophysical Research Letters 5, 419-421.

Skogseid, J., 2001. Volcanic margins: geodynamic and exploration aspects. Marine and Petroleum Geology 18, 457-461.

Smith, A.G., Hallam, A., 1970. The fit of the southern continents.

Solli, K., Kuvaas, B., Kristoffersen, Y., Leitchenkov, G., Guseva, J., Gandjukhin, V., 2008. The Cosmonaut Sea Wedge. Marine Geophysical Researches 29, 51-69.

Sotin, C., Parmentier, E., 1989. Dynamical consequences of compositional and thermal density stratification beneath spreading centers. Geophysical Research Letters 16, 835-838.

Stagg, H., 1985. The structure and origin of Prydz Bay and MacRobertson shelf, East Antarctica. Tectonophysics 114, 315-340.

Stagg, H., Colwel, J., Direen, N., O'brien, P., Bernardel, G., Borissova, I., Brown, B., Ishirara, T., 2004. Geology of the continental margin of Enderby and Mac. Robertson Lands, East Antarctica: insights from a regional data set. Marine Geophysical Researches 25, 183-219.

Stagg, H., Colwell, J., Borissova, I., Ishihara, T., Bernardel, G., 2006. The Bruce Rise area, East Antarctica: Formation of a continental margin near the greater India-Australia-Antarctica triple junction. Terra Antartica 13, 3.

Stagg, H.M.J., Colwell, J., Direen, N., O'Brien, P., Browning, B., Bernardel, G., Borissova, I., Carson, L., Close, D., 2005. Geological framework of the continental margin in the region of the Australian Antarctic Territory. Geoscience Australia Record 2004, 1-373.

Suess, E., 1885. Das antlitz der erde. Prag and Leipzig, 2778.

Svartman Dias, A.E., Lavier, L.L., Hayman, N.W., 2015. Conjugate rifted margins width and asymmetry: The interplay between lithospheric strength and thermomechanical processes. Journal of Geophysical Research: Solid Earth 120, 8672-8700.

Talwani, M., Abreu, V., 2000. Inferences regarding initiation of oceanic crust formation from the US East Coast margin and conjugate South Atlantic margins. Wiley Online Library.

Tan, E., Lavier, L.L., Van Avendonk, H.J., Heuret, A., 2012. The role of frictional strength on plate coupling at the subduction interface. Geochemistry, Geophysics, Geosystems 13.

Tominaga, M., Tivey, M.A., Sager, W.W., 2015. Nature of the Jurassic magnetic Quiet Zone. Geophysical Research Letters 42, 8367-8372.

Torsvik, T.H., Van der Voo, R., Preeden, U., Mac Niocaill, C., Steinberger, B., Doubrovine, P.V., van Hinsbergen, D.J., Domeier, M., Gaina, C., Tohver, E., 2012. Phanerozoic polar wander, palaeogeography and dynamics. Earth-Science Reviews 114, 325-368.

Tucholke, B.E., Sibuet, J.-C., 2007. Leg 210 synthesis: Tectonic, magmatic, and sedimentary evolution of the Newfoundland-Iberia rift, Proceedings of the Ocean Drilling Program, scientific results. Ocean Drilling Program College Station, TX, pp. 1-56.

Tucker, R.D., Roig, J.-Y., Moine, B., Delor, C., Peters, S., 2014. A geological synthesis of the Precambrian shield in Madagascar. Journal of African Earth Sciences 94, 9-30.

Van Avendonk, H.J., Lavier, L.L., Shillington, D.J., Manatschal, G., 2009. Extension of continental crust at the margin of the eastern Grand Banks, Newfoundland. Tectonophysics 468, 131-148.

Van Wijk, J., Huismans, R., Ter Voorde, M., Cloetingh, S., 2001. Melt generation at volcanic continental margins: no need for a mantle plume. Geophysical Research Letters 28, 3995-3998.

Veevers, J., 2009. Palinspastic (pre-rift and-drift) fit of India and conjugate Antarctica and geological connections across the suture. Gondwana Research 16, 90-108.

Veevers, J., 2012. Reconstructions before rifting and drifting reveal the geological connections between Antarctica and its conjugates in Gondwanaland. Earth-Science Reviews 111, 249-318.

White, R., McKenzie, D., 1989. Magmatism at rift zones: the generation of volcanic continental margins and flood basalts. Journal of Geophysical Research: Solid Earth 94, 7685-7729.

White, R.S., McKenzie, D., O'Nions, R.K., 1992. Oceanic crustal thickness from seismic measurements and rare earth element inversions. Journal of Geophysical Research: Solid Earth 97, 19683-19715.

Whitmarsh, R., Manatschal, G., Minshull, T., 2001. Evolution of magma-poor continental margins from rifting to seafloor spreading. Nature 413, 150-154.

Whittaker, J.M., Goncharov, A., Williams, S.E., Müller, R.D., Leitchenkov, G., 2013. Global sediment thickness data set updated for the Australian-Antarctic Southern Ocean. Geochemistry, Geophysics, Geosystems 14, 3297-3305.

Williams, S.E., Whittaker, J.M., Granot, R., Müller, D.R., 2013. Early India-Australia spreading history revealed by newly detected Mesozoic magnetic anomalies in the Perth Abyssal Plain. Journal of Geophysical Research: Solid Earth 118, 3275-3284.

Yan, P., Deng, H., Liu, H., Zhang, Z., Jiang, Y., 2006. The temporal and spatial distribution of volcanism in the South China Sea region. Journal of Asian Earth Sciences 27, 647-659.

Zhou, D., Ru, K., Chen, H.-z., 1995. Kinematics of Cenozoic extension on the South China Sea continental margin and its implications for the tectonic evolution of the region. Tectonophysics 251, 161-177.

Zhou, D., Yao, B., 2009. Tectonics and sedimentary basins of the South China Sea: challenges and progresses. Journal of Earth Science 20, 1-12.

Zhu, D.-C., Chung, S.-L., Mo, X.-X., Zhao, Z.-D., Niu, Y., Song, B., Yang, Y.-H., 2009. The 132 Ma Comei-Bunbury large igneous province: Remnants identified in present-day southeastern Tibet and southwestern Australia. Geology 37, 583-586.